MAGNETIC CLAMPING STRUCTURES FOR THE CONSOLIDATION OF COMPOSITE LAMINATES

A Thesis
Presented to
The Academic Faculty

by

Jordan Ziegenbein

In Partial Fulfillment
of the Requirements for the Degree
Master of Science in Mechanical Engineering
Woodruff School of Mechanical Engineering

Georgia Institute of Technology
May, 2011

MAGNETIC CLAMPING STRUCTURES FOR THE CONSOLIDATION OF COMPOSITE LAMINATES

Approved by:

Dr. Jonathan Colton, Advisor
School of Mechanical Engineering
Georgia Institute of Technology

Dr. Steven Danyluk
School of Mechanical Engineering
Georgia Institute of Technology

Dr. John Schultz
Georgia Tech Research Institute
Georgia Institute of Technology

Date Approved:

“That’s what education means – to be able to do what you’ve never done before.”

- George Herbert Palmer

Life of Alice Freeman Palmer, 1908.

ACKNOWLEDGMENTS

I would like to thank all of the people at Georgia Tech who made this thesis a reality. My classmates have been great sources of encouragement and fun and have helped me get perspective on problems within research. A special thanks is due to Jennifer Flachs who helped me develop the first version of the FEA model as a class project. I also am grateful to the mechanical engineering staff who provided me with so much support throughout the conceptual and experimental phases of this project. Louis Boulanger and John Graham of the machine shop and Kyle French and the folks in the electronics shop were tremendously helpful and patient. I would also like to thank JD Huggins for teaching me to use a tube bender. Dr. Rick Cowan also deserves a special thanks for helping me think through conceptual problems early on in the project. Furthermore, I would like to thank my thesis committee members, Dr. Steven Danluk and Dr. John Schultz, for their thoughtful comments, support, and investment of time. I am very grateful to Dr. Colton for inviting me to do research with him, for his advisement and motivation, and for being an excellent brainstormer. I have grown as an engineer and problem solver under his instruction. I'd also like to extend thanks to the students of UNIST, South Korea, particularly Gu-Hyeok Kang and Dae-Han Sung, who helped me with data collection. I also wish to thank my friends and family for their encouragement and for bearing with me; especially my wife, Elise, who is my best friend and personal counselor and has provided me with abundant encouragement. Lastly, I would like to Herbert Roters for his book, *Electromagnetic Devices*, which helped me develop an understanding and intuition about magnetic fields.

TABLE OF CONTENTS

LIST OF TABLES

LIST OF FIGURES

SUMMARY

Fiber reinforced polymer composite materials have generated great interest in the last few decades due to their low density, high strength and stiffness, and ability to be molded into parts of a variety of shapes and sizes. Composite materials require pressure to be applied in a direction normal to face of the part during the manufacturing process. This pressure, called the consolidation pressure, compacts the fibers and squeezes out excess polymer in order to create parts with superior volume fractions of reinforcing fibers, and therefore superior mechanical properties. Current methods for producing high-performance composite materials involve the use of autoclaves for the application of heat and consolidation pressure. Autoclaves are able to produce excellent parts but have significant disadvantages such as high cost and slow processing times, which are exacerbated at large scales. Current research is taking place to develop processes that can compete with and potentially replace the use of autoclaves. This research is often focused on enhancing traditional techniques, such as vacuum-assisted resin transfer molding (VARTM), that are already scalable and low-cost.

The objective of this thesis is to develop a novel device, which applies consolidation pressure to a composite part through the use of magnetic field interactions between electromagnets and an iron-filled rubber material. This magnetic clamping structure involves an array of electromagnets placed within or used as a one-sided rigid mold for a composite part. A magnetic silicone rubber sheet filled with iron particles, which may be cast into a variety of shapes, is placed over the part. When the

electromagnets are energized with DC current, magnetic flux is produced between them and the rubber, which causes attractive forces and therefore compression in the part.

Experiments were performed to characterize the force developed by the clamping device with regard to the independent parameters of the system: driving current, part thickness, rubber thickness, and magnetic filler loading percentage of the rubber. An apparatus was built to measure the attractive forces, power the electromagnets, and provide thermal management of the electromagnets. The magnetization curves of the rubber at various loading percentages were measured experimentally. A FEA model was developed in ANSYS to simulate the magnetic field inside the device and calculate the total attractive force. The model was validated using the experimental data. A discussion of the steps necessary to implement structural analysis into the FEA model is included as well.

The magnetic flux within the magnetic clamping structure was analyzed with a flux circuit approximation technique and with the FEA model. Magnetic phenomena such as flux leakage and saturation and their detrimental effects on the performance of the device were discussed. The performance of the clamping device was generalized based upon two characteristic proportions, which were optimized with the model. A method was developed by which the device may be designed based upon the thickness of the part to be consolidated and the required clamping pressure. The design method specifies the necessary electromagnet geometry, driving current and number of coils, and the parameters of the rubber component. The discussion is concluded with an example device design using characteristic ratios that provide an upper level bound on the power requirements of the device. The example demonstrated that the clamping structure is able

to generate 100 kPa of clamping pressure with a power requirement of less than 4 kW per square meter of part area. As such, the device could be used with a part the size of a commercial jet wing at a cost of only a few dollars per hour of operation. In addition, initial modeling demonstrates that the clamping pressure of the device may be increased by 3 to 4 times by utilizing armatures of either solid low-carbon steel or magnetic rubber made with advanced magnetic materials or processing techniques.

CHAPTER 1

INTRODUCTION

Autoclaves are used commercially for a number of fiber reinforced polymer composite materials, including thermoplastic and thermoset prepreg. Prepreg is laid onto a one-sided rigid mold, vacuum bagged, and autoclaved at pressures on the order of 1 MPa to compact the fibers and drive resin flow for part consolidation. Industrial autoclaves are significant capital investments and may cost a few million dollars. Recent engineering efforts, such as the Boeing 787 Dreamliner, have involved very large-scale composite parts, which require autoclaves big enough to contain them. As autoclaves grow, so do their capital expense, operating expenses, and processing times. As such, efforts have been made to adapt traditional composite manufacturing technology, specifically vacuum-assisted resin transfer molding (VARTM), to the requirements of high-performance composite applications. VARTM is a process by which dry reinforcement fibers are vacuum bagged and are infused with thermoset resin and consolidated by atmospheric pressure. The process is widely used on large-scale composite parts such as boat hulls and windmill blades. VARTM faces some challenges when it is applied as a process for high-performance composites. Dimensional tolerances of manufactured parts are often poor and consolidation pressures are limited to 100 kPa. Novel processes such as controlled atmospheric pressure resin infusion (CAPRI), patented by Boeing, are being developed to combat these challenges (Niggeman, 2008). It is proposed that a magnetic clamping structure involving electromagnets and a flexible, magnetic rubber may be used to create consolidation pressures great enough to compete with autoclaves or at least be used as an enhancement to VARTM.

The magnetic clamping device is composed of an array of electromagnets placed below the composite part and a flexible magnetic rubber sheet laid on top of the part. When the electromagnets are energized, the rubber is attracted to the electromagnets and creates compressive stress on the face of the part. The objective of this thesis is to discuss the capabilities of such a device and determine to what extent it may be used for the consolidation of composite laminates.

Chapter 2 includes a more thorough treatment of the topic of composite laminate consolidation and the mechanisms involved in fiber bed compaction. A review of the literature provides discussion of the necessary consolidation pressures for various composite materials and manufacturing processes. Out-of-autoclave techniques, such as CAPRI, are also discussed. Chapter 3 provides a theoretical background of the magnetic phenomena relevant to the development of the magnetic clamping device. The physical mechanisms responsible for magnetic forces, magnetization of materials, and the development of magnetic fields in tractive electromagnet systems are discussed. In addition, a background of magnetorheological materials is given to motivate discussion of the properties of the magnetic rubber used in the device. Chapter 4 contains the details of the apparatus built to characterize forces developed between electromagnets and the magnetic rubber, including a DC power supply, cold plate, and a non-magnetic load frame. The electromagnets purchased for the experiments were also studied to determine critical details of their construction. The development, fabrication, and magnetization curve testing of the magnetic rubber is also explained. The development of an axisymmetric FEA model of the system in ANSYS is also discussed, including mesh

convergence methods. The experiments performed with the apparatus and rubber are outlined in Chapter 4 as well.

Chapter 5 displays the results of the experiments and discussion of the effects of the experimental parameters on the force developed by the magnetic clamping device. The model was solved at similar parameter values and compared with the experimental results to validate the model. The device is also analyzed from a theoretical perspective as a magnetic flux circuit to determine the critical system proportions necessary to develop useful magnetic flux. Two device ratios are proposed as indicators of the performance of the device and optimum values for the ratios are determined using the FEA model. The clamping pressure of the device is also shown to scale independently of its geometric dimensions. A method is developed to design the magnetic clamping device such that it generates the desired consolidation pressure at a given scale. The chapter concludes with an example of this design process and a discussion of the power requirements of the device. In addition, the pressure profile developed by the device is discussed using both experimental data and the FEA model. The possibility of using arrays of electromagnets for the device is also discussed. Chapter 6 contains concluding remarks about the real-world practicality of the magnetic clamping device and recommendations regarding its implementation and further study required to complete the understanding of the capabilities of the device.

CHAPTER 2

BACKGROUND

Fiber-reinforced composite materials consist of high-strength, high-stiffness reinforcing fibers encapsulated in a polymer matrix. The matrix may be a thermoplastic (TP) or a cross-linking thermoset (TS) polymer. The matrix couples the mechanical properties of the reinforcement by surrounding each individual fiber. A large percentage of commerical composites utilize glass or carbon reinforcing fibers. The mechanical properties of a manufactured part increase with the volume fraction of fibers it contains. As such, reinforcing fiber volume fractions tend to be higher in high-performance applications, as well as constituent materials with superior properties. Low-performance applications such as boat hulls are often made of short E-glass fibers in a polyester matrix with volume fractions of approximately 0.25. On the other hand, aerospace applications frequently use carbon fiber reinforcements with volume fractions over 0.6 in a PEEK thermoplastic matrix. The fiber volume fraction of a finished composite part is highly dependent upon the consolidation pressure applied to compact the part during the manufacturing process.

Aerospace-level composite parts are often manufactured with the use of an autoclave, which applies the heat and pressure necessary to consolidate composites to high volume fractions. Gutowski (1997) gives 0.62 as a benchmark fiber volume fraction value for high-performance composite laminates. Industrial autoclaves are significant capital investments, in the range of many millions of dollars, and have many disadvantages. They build up pressure and heat slowly due to their enormous volumetric and thermal capacitance. Nitrogen gas is often used instead of air in order to discourage

the combustion of the resin or manufacturing materials in the presence of compressed oxygen, thereby increasing operating costs. In addition, autoclaves may be so large and heavy that disassembly or relocation is impossible; as such, related manufacturing processes are constrained to operate in the vicinity of the autoclave. Significant safety issues surround the use of autoclaves as well, as would be expected in situations involving large-scale pressure vessels. Autoclaving is, however, a mature technology and the process is able to make excellent quality composite parts out of a wide range of materials.

As the size of fiber reinforced composite parts has increased, and thus manufacturing costs, efforts have been made to develop out-of-autoclave processing techniques. Engineering feats such as the Boeing 787 Dreamliner, which utilizes a record percentage of composite materials in an aircraft, demonstrate the need to develop composite manufacturing techniques that may be utilized on a large scale and in a flexible manner. The capabilities of a magnetic clamping structure for the consolidation of composite laminates is explored in this thesis as a manufacturing method to potentially compete with traditional autoclaving processes. The purpose of this section is to discuss the mechanisms of composite consolidation and the required processing pressures and temperatures for a variety of composite materials. The consolidation pressures utilized in traditional manufacturing methods are used as benchmark values for comparison with the clamping pressure the magnetic device generates. In addition, current efforts to develop out-of-autoclave processing techniques are presented and discussed, with a focus on the enhancement of non-autoclave methods.

2.1 Composite Manufacturing Methods Overview

In this section the manufacturing requirements of various reinforcement-matrix systems, both TP and TS, are discussed. The nature of fiber bed compaction and associated modeling techniques are discussed briefly as well.

2.1.1 Consolidation of Fiber-Reinforced Composites

In the case of both TP and TS composites, the manufacturing process involves flow of the matrix material and compaction of the reinforcing fibers. Composite materials are often processed in the form of prepreg, in which the reinforcement is previously wet out either by a TP or TS resin. Alternatively, dry reinforcement may be used with a liquid thermoset resin. Thermoset resin in a liquid form is driven with a pressure differential into the reinforcing fibers to achieve fiber wet-out. Thermoplastic resin must be melted, often at temperatures up to 400°C for high-performance materials such as PEEK, and allowed to cool and solidify after the part has been molded. TS prepreg begins in a semi-solid, B-staged state of cure and is heated in order to initiate resin flow. The application of heat initiates the curing process and thus solidification of the thermoset resin. Polymer flow after fiber wet-out is important for a number of reasons. First, it allows the part to take the shape of whatever mold is utilized and capture necessary surface finishes. Second, polymer flow across layers of reinforcement cloth develops interlaminar shear strength as the layers of cloth are bound together. Finally, excess resin is driven out of the part resulting in improved fiber volume fractions. Polymer flow as described is achieved through the application of consolidation pressure normal to the face of the composite part.

Consolidation pressure also increases the fiber volume fraction of a composite part by compacting the individual fibers together. Gutowski developed a model for the static elastic deformation of fiber bundles, treating a bundle as a collection of curved beams. The Gutowski fiber compression model is frequently used in process modeling of fiber reinforced composites. The model is given by Equation 2.1,

$$\sigma = k \frac{\left(\sqrt{\frac{v_f}{v_0}} - 1 \right)}{\left(\sqrt{\frac{v_a}{v_f}} - 1 \right)^4} \tag{2.1}$$

where σ is the compressive stress in the fiber bed, k is an empirical constant based upon the nature of the fibers, v_f is the volume fraction of the fiber bed, v_0 is the unloaded volume fraction, and v_a is the maximum possible volume fraction (Gutowski, 1997). The model demonstrates that fiber bed compaction is nonlinear; increases in volume fraction must be accompanied by an exponential increase is consolidation pressure due to the stiffening effect of the fiber bed. Actual process modeling of composite part deformation includes the transient viscous effects of the resin flow. Viscous forces are much higher in the case of TP resins than TS resins. Uncured epoxies generally have viscosities less than 100 Pa-s, and may be as low as 1 Pa-s, while thermoplastics are between 100-5000 Pa-s at their melt points (Åström, 1997). As such, TP prepreg laminates require higher consolidation pressures to drive the appropriate resin flow in a timely manner while achieving the necessary fiber compaction.

2.1.2 Thermoplastic Prepreg Consolidation

Thermoplastic polymer material is solid when cool and TP prepreg plies are stiff and often difficult to position at room temperature. A number of processing techniques are available for use with TP prepreg. In-situ tape-laying overcomes prepreg stiffness through localized heating of a small width of prepreg tape as it is continuously laid down onto a part and allowed to cool. Prepreg stacks may also be formed into a final part by compression molding with matched, heated dies using consolidation pressure of at least 1 MPa (Åström, 1997). Long (2001) reported that consolidation pressures of 3 MPa and temperatures of 200°C were necessary to reduce void contents to below 1% in a glass fiber and polypropylene material. Ramasamy, Wang, and Muzzy also performed extensive consolidation experimentation with carbon fiber and nylon in compression molding, utilizing pressures up to 700 kPa (Ramasamy, 1996). Vacuum bagging with autoclave consolidation is a very common processing method as well. Stacks of prepreg are laid onto a one-sided rigid die, frequently topped with a caul plate to help maintain the shape of the other side of the composite, and covered with breather and/or bleeder material and a vacuum bag. The bag is sealed and the system is evacuated of air. The setup is placed in an autoclave to be heated and the ambient pressure is brought to approximately 1 MPa. The vacuum drawn in the bag increases the consolidation pressure experienced by the part by 1 atm or 100 kPa. Åström suggests a typical autoclave consolidation cycle for a carbon and PEEK composite includes a temperature of 390°C and pressures up to 1 MPa. These examples demonstrate that composite laminates made with thermoplastic prepreg generally require at least 1 MPa of consolidation pressure. This value will be used as a benchmark for the necessary required clamping pressure of

the magnetic clamping device in order for it to be practical for use with thermoplastic laminates. Additionally, in order for the device to be used with high-performance composites it must be able to withstand temperatures of 400°C conservatively.

2.1.3 Thermoset Prepreg Consolidation

While compression molding techniques similar to those used with thermoplastic prepreg may be used with thermoset prepreg, autoclaving offers significant advantages in process flexibility over compression molding. Only a one-sided mold need be used and temperatures and pressures are easily adjustable except with some lag time. Prepreg is placed on the mold with bleeder material to absorb excess resin, breather material to maintain even vacuum, and vacuum bagged. A porous barrier is also used to prevent saturation of the breather. The bagged setup is then processed in an autoclave. Figure 2.1 shows the components involved in the process.

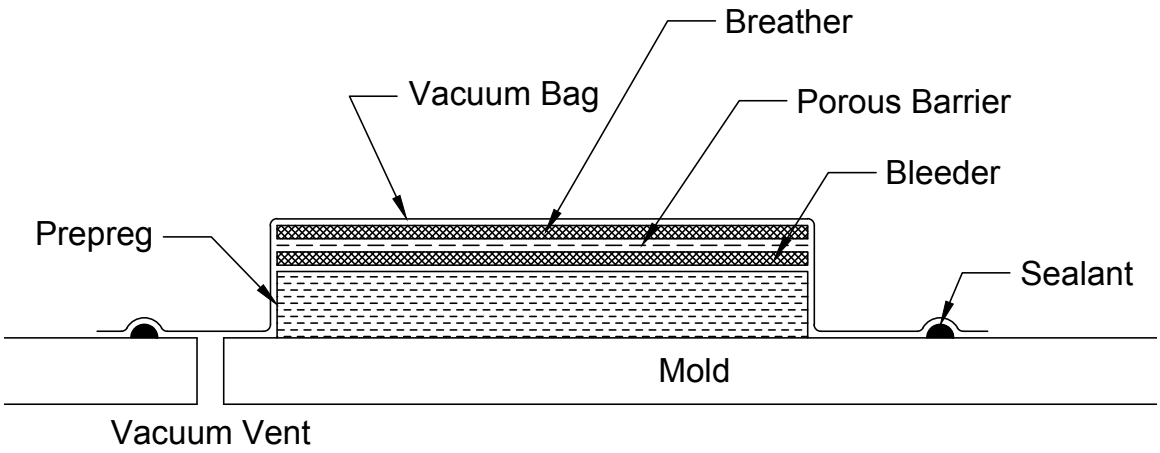

Figure 2.1 Typical thermoset prepreg processing

Figure 2.1 shows the composite prepreg covered with the supporting media and vacuum bagged on a mold. The vacuum vent is shown on the left hand side of the mold.

Early work by Young (1995) demonstrated that the degree of consolidation, and therefore the quality, of TS prepreg laminates is most strongly influenced by the autoclave consolidation pressure. Cure cycle temperature history, while important to the overall process, is not critical to the final volume fraction of the part. Dillon, et al., state that common high-performance epoxy-based composites require autoclave temperatures of 175°C and pressures of 600 kPa (Gutowski, 1997). These values are therefore used as the necessary operating temperature the magnetic clamping structure must withstand and clamping pressure the clamping structure must exert in order for it to be of value in TS prepreg consolidation.

One interesting, recently developed molding process intended to compete with autoclaving is the Quickstep process. The technique is mentioned here because it is used with TS prepreg lay-ups. The prepreg is laid up on a one-sided rigid mold and is placed in a device that encapsulates it with two rubber bladders inside a rigid frame. Figure 2.2 shows the details of the process.

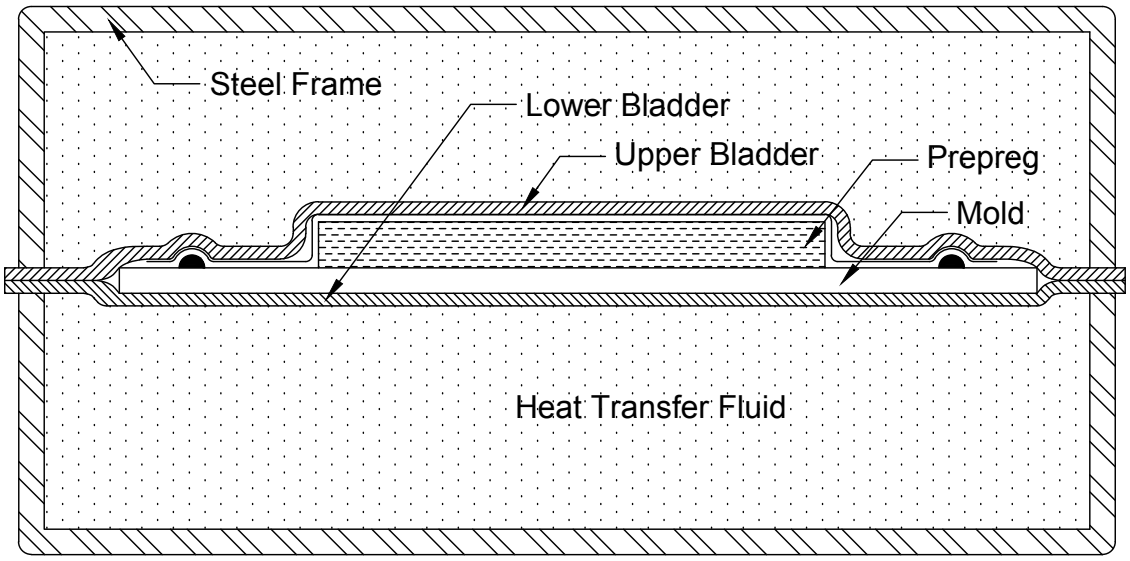

Figure 2.2 Quickstep process for thermoset prepreg

The bladders are filled with a heat transfer fluid, which is heated and circulated to control the temperature of the laminate. The process is able to heat and cool the part much more quickly than an autoclave process. In addition, the fluid may be pressurized to aid in the consolidation of the part. A recent study was performed comparing the properties of Hexcel 6376 carbon fiber prepreg laminates using the Quickstep process with 100 kPa consolidation pressure and an autoclave process with an applied pressure of 800 kPa. The Quickstep and autoclave processes yielded parts with fiber volume fractions of 60.2% and 64.1%, respectively (Davies, 2007). The primary advantage with the Quickstep device is the thermal flexibility of the process due to high convection coefficients possible with a heat transfer liquid. However, because the entire part is contained within a rigid, fluid-filled device, such as an autoclave, Quickstep offers no potential benefit in terms of consolidation pressure. Were the heat transfer fluid pressurized to, say, 1 MPa, the device would still have to be built to withstand the same forces as a pressure vessel filled with air at 1 MPa. The device faces the same challenges as the autoclave in terms of scaling.

2.1.4 Vacuum-Assisted Resin Transfer Molding

Vacuum-assisted resin transfer molding (VARTM) is a process commonly used to manufacture good quality thermoset composite parts of a variety of sizes. Dry reinforcement is vacuum bagged on a one-sided rigid mold along with flow-enhancing media and ports for resin and vacuum vents. Figure 2.3 displays the process and the related components. Note that flow media are placed over the entire part and under both the resin port and the vacuum vent in order to allow resin flow throughout the entire system.

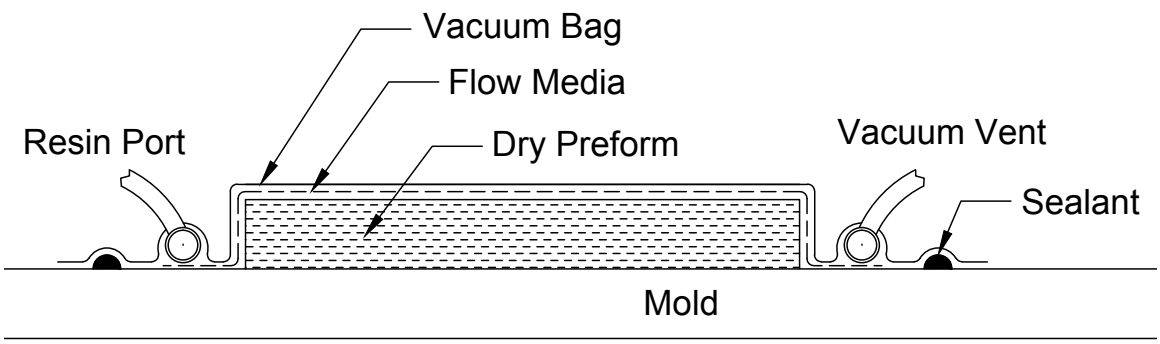

Figure 2.3 Typical VARTM process

Thermoset liquid resin, such as epoxy, is driven into the dry, evacuated preform via the pressure differential created by the vacuum. Atmospheric pressure acts as the consolidation pressure for the part because it is at or near zero absolute pressure. The entire system may be placed in an oven after infusion if the resin requires a high-temperature cure. The process can yield composite parts with volume fractions of 0.5 or greater. One of the significant advantages of the process is that the size of the part is limited only by the size of the mold. While resin flow lengths are limited by the permeability of the compacted fibers and the required processing time, large parts may be broken down into repeated infusion cells each covering a certain amount of area (Potter, 1997). Extremely large structures, such as boat hulls and windmill blades, are routinely manufactured by VARTM. Furthermore, an advantage of the VARTM process is the cost savings and ease of handling of dry reinforcement cloth as opposed to TS prepreg.

2.2 VARTM as an Out-of-Autoclave Process

VARTM cannot generate parts to the degree of quality possible with an autoclave. Abraham (1998) studied the difference between E-glass and epoxy panels manufactured with traditional autoclaving using pressures of 1.3 MPa and with VARTM using only

atmospheric pressure for consolidation. VARTM yielded a part with a volume fraction of 50.4% while autoclaving yielded 63.9%. Tensile strength of the VARTM part was 17.7% less than the autoclaved part, although the void content was slightly lower for the VARTM part. This example is typical of the discrepancy between VARTM and autoclaved parts due to an order of magnitude difference in consolidation pressure. However, VARTM has great advantages over autoclaving in terms of process flexibility, cost, and scalability. Current research efforts have taken place to enhance the utility of VARTM. In this section, some of these efforts are discussed and the magnetic clamping structure device is presented as a possible enhancement to traditional VARTM.

2.2.1 Double Vacuum Bagging

Traditional VARTM techniques employ a single vacuum bag covering a dry preform. The preform is completely evacuated and compacted by the vacuum bag and the resin, which is at atmospheric pressure, is drawn into the space between the fibers due to the pressure differential. Epoxy resins are degassed at full vacuum after mixing to completely remove dissolved and entrained air before infusion. Incomplete degassing results in the evolution of voids throughout the part when the epoxy is drawn in. Other types of high-performance, high-temperature resins such as polyimides and phenolics, however, generate water and volatiles during the curing process, which occurs after infusion. The consolidation pressure of the vacuum bag prevents the escape of these volatiles. Hou, et. al, (2008) developed a novel double vacuum bag process which enhances the ability of the traditional VARTM process to handle volatiles given off by the resin. The double vacuum bag method involves a porous steel frame placed over the original vacuum bag and part. A second vacuum bag is placed over the steel frame and is

sealed with respect to the rest of the system. The pressure within both vacuum bags may be controlled independently. At different stages of the infusing and curing process the two pressures are adjusted. The outer bag may be vented to atmosphere and the inner bag completely evacuated to generate maximum consolidation pressure. Also, the outer bag may be brought to full vacuum with the inner bag at partial vacuum, allowing the volatiles to be drawn out of the part due to the high vacuum situation but eliminating compaction pressure. The steel frame prevents the outer bag from collapsing onto the inner bag and part. Experiments qualitatively demonstrated superior parts and low void content with the double vacuum bag process. The process can also be carried out with a single vacuum bag setup placed within a vacuum oven, provided the pressure inside the vacuum bag and the pressure in the oven can be controlled independently. However, a double vacuum bag and frame setup is more suited to a large-scale VARTM process because a large vacuum oven would be required for large parts.

2.2.2 Controlled Atmospheric Pressure Resin Infusion (CAPRI)

One of the main drawbacks of the traditional VARTM process is the dimensional tolerance realizable in the finished part. As infusion takes place, compaction pressure in the part is lost to some degree because of the introduction of the resin. The compaction stress on the fibers is given by Equation 2.2,

$$P_{\text{atm}} = \sigma + P_{\text{resin}} \tag{2.2}$$

where P_{atm} is atmospheric pressure, σ is the normal stress on the part, and P_{resin} is the pressure carried by the resin fluid (Acheson, 2004). The equation shows that when the resin is allowed to bear some of the load of atmospheric pressure, the consolidation pressure of the fiber bed is reduced accordingly. Acheson, et al., demonstrated

experimentally that parts manufactured with VARTM tend to show final dimensions that are thicker near the resin inlet ports and thinner at the vacuum vents due to resin pressure reducing the load on the preform. Thickness variations as great as 9% over the length of the part were observed. Similar trends in part thickness variation with traditional VARTM were observed by Niggeman, et al. (2008), with variations of up to 4% in a 60cm long, 8mm thick part. Preform stress was measured at the inlet and vent side of the part after full infusion with VARTM. The vent side was at nearly full vacuum of 97 kPa while the inlet side was at 22 kPa, with a linear variation in stress across the length of the part. The experimental results also indicated that the fabricated part did not have a consistent fiber volume fraction across its length.

The controlled atmospheric pressure resin infusion method (CAPRI), patented by Boeing, was developed to combat part thickness variation. CAPRI is essentially VARTM with two additional modifications. First, the fiber bed is subjected to a debulking process before infusion, in which the fibers are bagged and vacuum is drawn on the part and released repeatedly. A 15-layer E-glass cloth preform was shown to compact at full vacuum from a thickness of 8.2mm to 7.8mm after 400 debulking cycles. Additional debulking did not show further improvement. The debulking process causes the fibers to "nest," reducing the overall part height and reducing the springback of the fibers. The CAPRI process also involves infusion of the resin at partial vacuum. The resin container is placed in a vacuum chamber at half-vacuum before infusion is initiated. This effectively reduces the maximum P_{resin} term in Equation 2.2. Half-vacuum infusion increased the preform pressure at the inlet side from 22 kPa to approximately 60 kPa and reduced the thickness variation across the length of the part to less than 1%. Final part

total volume fractions increases of 5% were reported with the debulking and half-vacuum infusion processes combined. The results of the study indicate that the debulking process is primarily responsible for the increase in fiber volume fraction and the half-vacuum infusion process is responsible for the decrease in thickness variation, though the two are not entirely independent. One significant downside to the CAPRI process is that infusion times are increased due to the decreased fiber permeability from debulking and decreased pressure differential in half-vacuum infusion. Experimental application of the CAPRI process resulted in infusion times increased from standard VARTM by a factor of 6.

2.2.3 Magnetic Clamping Structures as VARTM Enhancement

Current research efforts in the literature demonstrate that there is significant interest in enhancement of the traditional VARTM process to manufacture composite laminates with increased fiber volume fractions and dimensional tolerance and with high-performance materials. The results of the CAPRI process demonstrate that debulking cycles significantly improve the fiber volume fraction of parts produced with only atmospheric pressure consolidation in VARTM. The magnetic clamping structure is able to develop clamping pressures rapidly, potentially faster than possible with a vacuum pump, and may have value as a debulking device if it is designed to apply at least 100 kPa of pressure. In addition, the results of the Acheson and Niggeman VARTM studies have shown that part thickness variation from the resin inlet to the vacuum vent is a common problem due to fluid resin pressure in the preform. The CAPRI half-vacuum infusion process demonstrated that part thickness gradients may be significantly reduced by reducing the proportional difference between the preform compaction stress at the inlet and outlet. It is proposed that a magnetic clamping structure, placed on top of the

vacuum bag in a traditional VARTM process, may be able to produce the same decrease in part thickness gradient with or without half-vacuum infusion by adding clamping pressure over the entire part. The increased clamping pressure may also increase the final volume fraction of fibers in the part. Given that the difference in preform consolidation pressure due to resin pressure in VARTM is at most 100 kPa (atmospheric), this pressure will be used as another benchmark value for the magnetic clamping device.

In summary, this chapter discussed the mechanism of composite laminate consolidation for thermoplastic and thermoset prepreg materials as well as dry fiber preforms. The processing conditions, especially consolidation pressure, commonly used to manufacture good quality parts out of these materials in autoclaving, VARTM, and compression molding, were discussed. The necessary consolidation pressures are set as points of comparison for the performance of the magnetic clamping device. Both thermoplastic and thermoset prepreg require compaction pressures of approximately 1 MPa. Additionally, high-performance TP and TS prepregs require processing temperatures near 400°C and 175°C, respectively, so the device must be designed to withstand these temperatures. Traditional VARTM methods also were discussed as well as recently developed techniques, such as CAPRI, to enhance the utility of VARTM. Due to the challenges inherent in maintaining low part thickness gradients in VARTM, it is postulated that the magnetic clamping device might be used as an enhancement to VARTM if it is able to produce clamping pressures of at least 100 kPa. Furthermore, if the device can generate 100 kPa it may also be utilized for rapid compression and decompression of dry fiber preforms for the CAPRI debulking technique.

CHAPTER 3

THEORETICAL BACKGROUND

The purpose of the device is to generate pressure at the surface of a composite laminate using a ferromagnetic rubber structure. It is well understood that ferromagnetic materials experience attractive forces in magnetic fields. However, the physical interactions behind these forces have many complications arising from geometry and nonlinear material behavior. This section lays out the general theory behind magnetic forces by defining important magnetic field terminology, discussing ferromagnetic material behavior, and outlining an analytical solution method for static magnetic systems.

3.1 Magnetic Fields and Forces

This section presents the terminology and fundamental relationships used to analyze static magnetic systems. A discussion of magnetic body forces and surface stresses is included as well as a description of the magnetic circuit analysis method.

3.1.1 Magnetic Field Nomenclature

It is necessary to note the distinction between the notation B and H when dealing with magnetic fields. B refers to the magnetic flux density (Tesla) and H refers to the magnetic field intensity (amp-turns/meter). In non-magnetic materials the two follow a simple linear relationship:

$$B = \mu_0 H \tag{3.1}$$

where μ_0 is the permeability of free space. In ferromagnetic materials such as iron, a magnetization term is added:

$$B = \mu_0 H + \mu_0 M \tag{3.2}$$

where M is the magnetization of the material due to the alignment of magnetic dipole domains present in ferromagnets (Bansal, 2004). The term M is a non-linear function of H. It is helpful to consider a magnetic material as having two overlapping domains: vacuum and ferromagnetic. The $\mu_0 H$ term is the response of vacuum domain and the $\mu_0 M$ term is the response of the ferromagnetic domain. The two terms combined yield the total induced field B of the material to an applied field H. The curve relating these two values is known as the BH curve. The differential permeability (or simply the permeability) of a material is defined as

$$\mu = \frac{dB}{dH} \tag{3.3}$$

The permeability of a material is equal to the slope of the BH curve at the field value the material is experiencing. Permeability is often reported relative to vacuum as $\mu = \mu_r \mu_0$ where μ_r is the relative permeability. Vacuum and other non-magnetic materials such as air, plastic, and aluminum have relative permeability equal to unity. These phenomena are discussed at further length in section 3.2.

3.1.2 Magnetic Forces

A ferromagnetic structure magnetized to $\vec{M}$ by a prevailing field $\vec{B}_0$ experiences a volumetric body force, $\vec{f}$, given by Equation 3.4.

$$\vec{f} = \vec{M} \cdot \nabla \vec{B}_0 \tag{3.4}$$

The net force, $\vec{F}$, experienced by the structure is given by Equation 3.5,

$$\vec{F} = \int \left(\vec{M} \cdot \nabla \vec{B}_0 \right) dv \tag{3.5}$$

where *v* indicates the volume of the magnetized body. Moon (1984) demonstrates that the distributed body force may be rewritten as Equations 3.6 and 3.7,

$$\vec{f} = \nabla \cdot \mathrm{T}^{em} \tag{3.6}$$

$$\mathrm{T}^{em} = \frac{1}{\mu_0}\left(\vec{B}\vec{B} - \frac{1}{2}B^2\delta\right) \tag{3.7}$$

where δ indicates the Kronecker delta function and T^{em} is the electromagnetic stress tensor. Applying the divergence theorem allows the net force to be written as a surface traction problem over an area, *a*, given by Equation 3.8.

$$\vec{F} = \int \left(\mathrm{T}^{em} \cdot \vec{n}\right) da \tag{3.8}$$

Further simplification yields Equation 3.9, an expression for magnetic pressure, p_{mag}, at a surface of a magnetized body,

$$p_{mag} = \frac{B_n^2}{2\mu_0} \tag{3.9}$$

where B_n refers to the component of the flux density normal to the faces of interest (Moon, 1984). This stress is often referred to as pressure but it does in fact act outward from the face of the body. The previous equation provides a convenient method for calculating the distributed stress on ferromagnetic structures as B_n may be calculated or directly measured with a Gaussmeter.

3.1.3 Magnetic Circuit Analysis

Magnetic systems are inherently dipolar; every source of a magnetic field also has a sink. Magnetic fields therefore create closed paths or circuits. The concept of a magnetic circuit is introduced to facilitate understanding of the interactions of magnetic

media and the magnetic fields that exist within them. The magnetic circuit analysis method detailed in this section allows for simplified calculations of magnetic field problems and ultimately for estimations of magnetic forces.

According to Ampere's circuital law for a surface *S* with perimeter *C*,

$$\oint_C B \cdot dl = \mu_0 \iint J \cdot dS \tag{3.10}$$

where *J* is current density (ampere per square meter). The relationship shows that current density normal to a surface necessarily creates a magnetic field, *B*. For the purposes of this thesis it is important to consider *S* as the cross-sectional area of a wound electromagnet coil. Such a coil of *N* turns which is excited by a current *I* generates a magnetomotive force (*mmf*) of *NI* amp-turns. Magnetic flux, Φ, given in webers, results from the following relationship, shown in Equation 3.11,

$$\Phi = \frac{NI}{R} \tag{3.11}$$

where *R* is the reluctance (amp-turn/weber) of the path that the flux follows. This relationship is intuitively related to Ohm's law if flux is thought of as current, *mmf* as voltage, and reluctance as resistance.

Magnetic flux follows the paths of least reluctance as it completes the magnetic circuit mandated by Ampere's law. Flux paths are complicated and may be impossible to calculate exactly by analytical means (Roters, 1941). Simplifications may be made in order to estimate the solutions to magnetic circuit problems. Magnetic problems are divided into reluctance elements with a mean flux path through each element. Each element has a certain reluctance and is connected to other elements in series or parallel. Magnetic flux follows the same rules as electric current. The flux into an element is equal

to that out of the element. Flux is conserved around closed loops. This allows complex magnetic field problems to be dealt with much like classic resistor network problems. The primary difference between magnetic and electric circuits, however, is that the reluctance of a magnetic circuit element is dependent upon the field within in. Each element of the circuit has reluctance given by Equation 3.12,

$$R \equiv \int \frac{dl}{\mu S} \tag{3.12}$$

where S is the cross-sectional area of the element, l is the length of the mean flux path, and μ is the permeability. For simple geometries the reluctance may be expressed as Equation 3.13.

$$R = \frac{l}{\mu S} \tag{3.13}$$

Because μ is nonlinearly dependent upon the applied field for ferromagnetic elements, the problem must be solved in an iterative fashion. The flux, Φ, through an element of cross sectional area S is related to the flux density B by Equation 3.14.

$$B = \frac{\Phi}{S} \tag{3.14}$$

To complete the Ohm's law analogy Equation 3.15 must be considered.

$$H = \frac{mmf}{l} \tag{3.15}$$

Equation 3.15 shows that to maintain a magnetic field intensity H over an element of length l a certain *mmf* is required. Hence, the *mmf* of an element is like a voltage drop across a resistor. The sum of all *mmf* terms around a magnetic circuit is equal to the total driving *mmf*, which is *NI*.

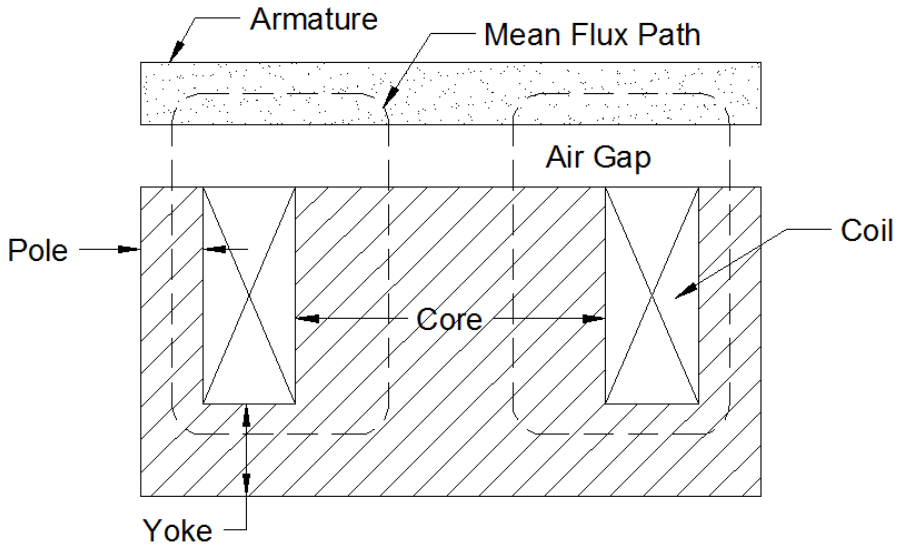

Figure 3.1 Round electromagnet and armature with flux paths

Figure 3.1 shows the cross section of a flat-faced cylindrical lifting electromagnet coupled with an armature through an air gap. Coil windings are encapsulated in steel, shown with the crosshatch. The steel is also referred to as the back iron. The center of the back iron is the core, the underside is the yoke, and the side is the pole. The armature is shown above the face of the magnet with an air gap between them. This air gap is known as the working air gap since the electromagnet does work through the thickness of the gap. The dashed lines indicate the mean flux path around the circuit.

The magnetic circuit method is useful for analyzing the magnetic flux in tractive systems such as the one shown in figure 3.1. The iron sections of the magnet, the air gaps, and the armature are divided into circuit elements. With knowledge of the BH characteristic of the materials involved, the system may be solved at different current excitations. When the total flux through the circuit elements is known the flux density of the working air gaps may be calculated. The effective tensile stress at the face of the armature can then be determined using Equation 3.9.

3.2 Magnetic Material Models

The purpose of this section is to describe the intrinsic behavior of ferromagnetic materials such as steel and iron as well as composite magnetic materials. As mentioned in the previous section, the primary concern is to determine the response of a material in terms of magnetic flux density, B, to a static applied magnetic field intensity, H. The BH curve (or induction curve) of a magnetic material is necessary in order to solve magnetic field problems that involve such materials. Composite magnetic materials, a composition of magnetic particles in a non-magnetic matrix, exhibit interesting physical behaviors. BH curves and permeability models of composite magnetic materials are discussed in this section as they apply to the iron-filled rubber used in the consolidation pressure device. Magnetic composites involving an elastomeric matrix exhibit field dependent elastic moduli and are referred to as magnetorheological (MR) elastomers. The structural properties of MR materials are discussed briefly in this section as well.

3.2.1 Intrinsic Magnetic Behavior of Ferromagnetic Materials

For the purposes of this paper only the properties of soft magnetic materials are discussed. Magnetic materials are generally described as either soft or hard. Hard magnetic materials retain a certain amount of an induced magnetization when the original field is removed and exhibit hysteresis when the applied field is reversed. Permanent magnet materials such as ferrites, rare earth, and samarium cobalt are magnetically hard. Magnetically soft materials have single-valued BH curves and retain little to no magnetization when an applied field is removed. Soft magnetic materials include iron, nickel, cobalt, and their various oxides and alloys.

Soft magnetic materials are composed of magnetic domains. These domains are randomly aligned in the absence of a magnetic field and exhibit no net magnetization. In the presence of an applied field the domains align with the prevailing field and support it. As discussed earlier, the total *B*-field response of a magnetic material may be thought of as the response of vacuum plus the response of the domains. As the applied field grows, the ferromagnetic domains become increasingly aligned with the applied field. Eventually all the domains are aligned and cannot respond to a further increase in applied field. As this point the material is saturated. Saturation flux density is not defined rigorously but refers to the magnitude of flux density, B_{sat}, at which the permeability is near unity. Soft magnetic material is characterized by high permeability at low applied fields and low permeability at high applied fields. To illustrate these phenomena the BH curve of 1018 steel is shown in Figure 3.2.

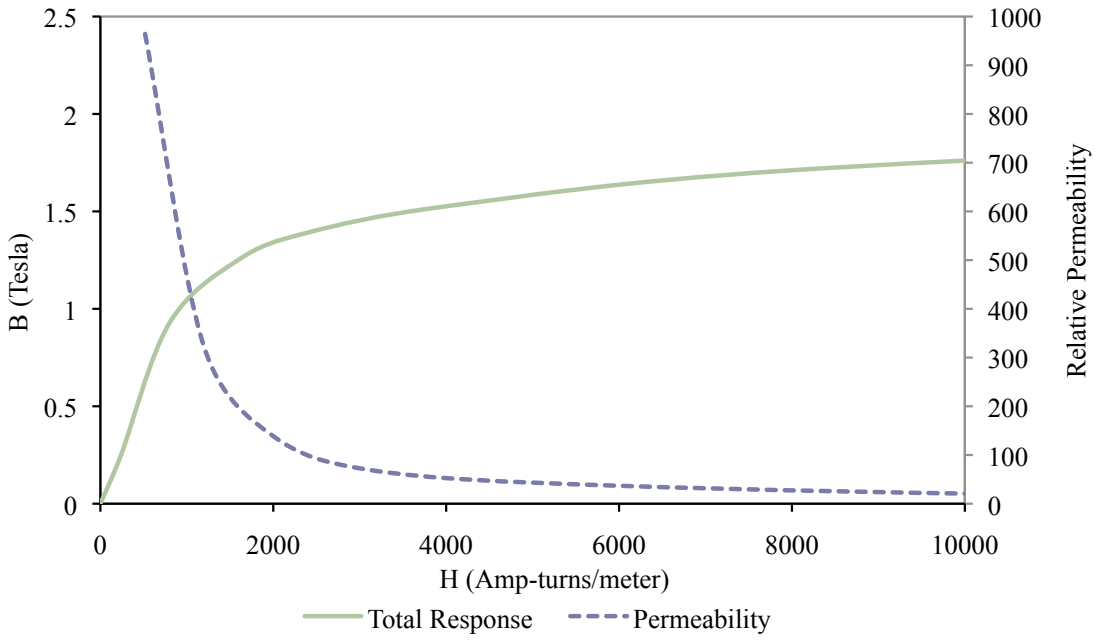

Figure 3.2 BH and Permeability curve of 1018 steel

Figure 3.2 shows the magnetic response of 1018, a common low carbon steel that is often used in electromagnetic devices (ASM, 1978). The solid curve is the BH curve of the material and the segmented curve shows the relative permeability of the material (shown on the right hand scale). The permeability curve demonstrates a sharp rise up to about $H = 600$ followed by an asymptotic fall. The point where the permeability begins to drop, around $H = 1000$ in this case, is called the knee of the curve. Figure 3.3 demonstrates the effect of magnetic saturation in 1018 steel.

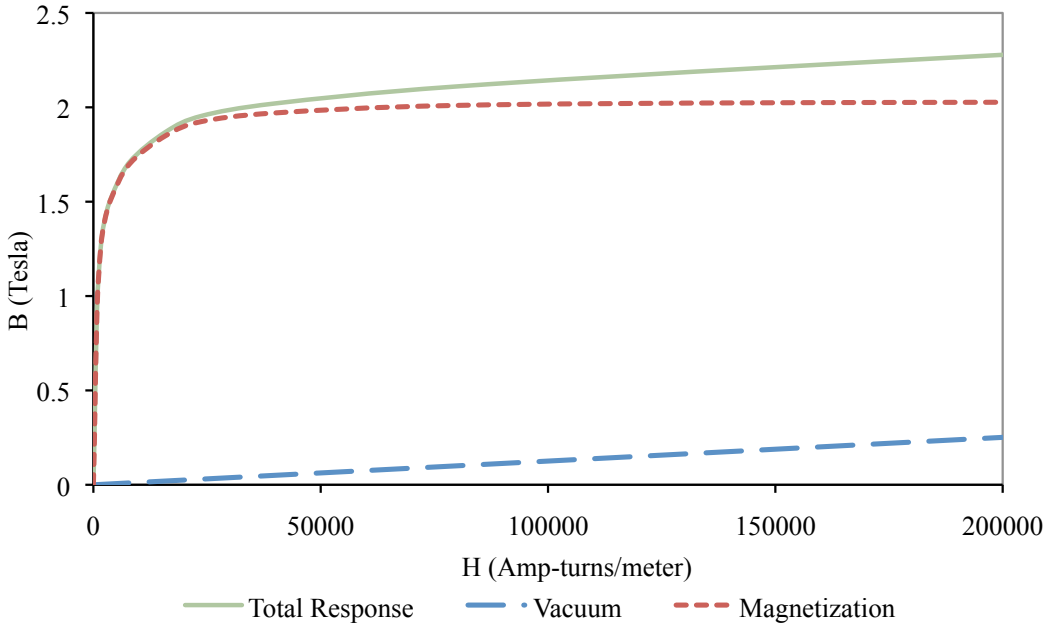

Figure 3.3 BH curve of 1018 steel showing vacuum response and magnetization

Note that the horizontal scale in Figure 3.3 is extended from what is shown in Figure 3.2. The solid curve is the total response of the material (same as Figure 3.2), the dotted line is the magnetization or response of the magnetic domains, and the dashed line is the response of vacuum. The total response is the sum of the magnetization and vacuum response as given in Equation 3.1. The divergence of the total response and the

magnetization curves indicates the degree of saturation of the material. At an applied field of H = 50,000 Amp-turns/meter the magnetization curve is nearly level at B_{sat} = 2 Teslas.

The primary ferromagnetic elements are iron, nickel, and cobalt. A number of alloys and oxides of these elements exist with various properties such as initial permeability, hysteretic losses, or saturation flux density. The latter is the most important property for devices that generate mechanical forces like lifting electromagnets, which are designed to operate at very high applied fields. High purity iron has a saturation flux density of 2.15 Teslas and steels with minimal alloying elements, such as 1018 and 12L14, saturate at about 2 Teslas. Steels with higher percentages of alloying elements generally have lower saturation points, so electromagnet casings are usually constructed of low carbon steel.

3.2.2 Composite Magnetic Materials

The composite laminate consolidation device consists of a sheet of iron-filled rubber that is attracted to an electromagnet placed underneath the part. An understanding of the behavior of this rubber is important with regard to the modeling and design of the device. This section discusses the magnetization and elastic models of magnetic composites, which are defined here as magnetic particles dispersed in a non-magnetic matrix.

Research concerning the physical behavior of magnetic composite materials is focused in the areas of magnetorheological (MR) materials and polymer bonded soft magnetics (PBSM). The matrix materials of MR materials include elastomers, gels, and liquids. They are typically characterized by particle volume fractions of less than 50%.

MR materials exhibit magnetic field-dependent structural phenomena. The structural damping, elastic modulus, or yield stress of a MR material may be changed by application of a magnetic field. These materials are studied for their use in tunable damping systems such as automotive engine mounts or fluid-filled shocks. PBSMs are polymer-coated magnetic particles that are pressed or sintered together. They have good magnetic properties and low electrical conductivity making them suitable for high-frequency induction applications like transformer cores. PBSMs tend to have higher particle volume fractions than MR materials.

A review of the literature shows that research has been done to determine the effect of magnetic particle material, size, and loading fractions on the magnetic response of composite materials. Attempts have also been made to determine magnetization models. Jolly developed a numerical model for the magnetization of chains of magnetic particles in a non-magnetic medium. It was shown that B_{sat} of the composite is related to the saturation point of the magnetic material and the volume loading fraction by Equation 3.16,

$$B_{sat} = \phi B_{sat,0} \tag{3.16}$$

where ϕ is the particle volume fraction and $B_{sat,0}$ is the saturation field of the magnetic material (Jolly, 1996). This equation shows that composites made of high saturation point materials at high loading fractions can be expected to yield superior high-field clamping performance. Anhalt (2008) demonstrated that the initial permeability of magnetic composites is independent of particle size but maximum permeability values slightly increase with increasing particle diameter. It has been shown that initial permeability increases with particle loading fraction. Particle alignment has also been shown to be a

factor in the magnetization behavior of magnetic composites. Vicente, et al., (2002) showed that particles in a liquid or elastomer show a local maximum as the applied field tends to align them. Particles pre-aligned in a rigid medium do not display this phenomenon. Carbonyl iron particles of 1 μm mean diameter dispersed in an elastomer and epoxy had relative permeabilities of about 2.5 and 3, respectively, which tended to decrease with increasing applied field. Other experiments by Anhalt, et al., (2007) used 88 μm carbonyl iron powder in polypropylene and yielded a relative permeability of about 3. Much of the work to characterize MR materials has occurred recently and no complete model exists that accurately represents their BH characteristics. Magnetic properties of the filler material, geometry and distribution of the filler particles, and structural properties of the matrix are all complications and have not been unified. As such, any accurate information about a MR elastomer must be determined by experimental testing.

Magnetorheological effects and their dependencies upon the constituents of magnetic composites are also surveyed in the literature. The shear modulus of a MR elastomer of 27% iron particle loading may be increased by as much as 50% when a 1 Tesla field is applied to it (Davis, 1999). Jolly, et al., (1996) demonstrated that both an increase in particle loading and applied field result in an increase in elastic modulus of a similar MR material. These results are important for magneto-structural coupled modeling of MR elastomers. At high magnetic fields MR materials may be significantly stiffer than a zero field situation. Highly accurate structural modeling of a MR elastomer with applied magnetic fields would therefore require this field-stiffening effect to be

considered. This sort of field-stiffening structural model is not within the scope of this thesis, however, but future modeling efforts should consider including these effects.

3.3 Chapter Summary

This section discussed magnetic field theory and terminology relevant to the scope of the thesis. The basics of applied and induced fields and an overview of ferromagnetic materials was included. Magnetic forces were discussed with specific focus on development of surface traction equations. An analytical method of solving magnetic field problems as reluctance circuits was outlined which may be employed to facilitate understanding of tractive electromagnet problems. Electromagnet construction and terminology was also discussed briefly. This section also contained a treatment of magnetorheological materials, specifically elastomers, with regard to intrinsic magnetic response and field-dependent elasticity.

CHAPTER 4

EXPERIMENTAL METHODS

The purpose of the magnetic clamping structure device is to apply consolidation pressure normal to the face of a composite laminate. Experiments were performed to characterize the forces developed in the magnetic rubber material by magnetic fields. The primary goal was to gain an understanding of the magnitude and distribution of such forces. Samples of magnetic rubber of various iron loading percentages and thicknesses were made. The attractive forces between the samples and electromagnets were measured using an Instron load frame. A FEA model was developed in ANSYS to predict attractive forces with varying parameters and its results were compared with the force measurements for validation. Validation of the model allows extrapolation to predict the pressure generated with high applied currents. This chapter provides the details of the experimental apparatuses and the magnetic rubber that was fabricated. The experiments that were performed are described, as well as the development of the FEA model.

4.1 Apparatus

This section describes the various devices used in the experiments. Electromagnets were used to generate magnetic fields. The type of steel used in the electromagnets was determined by a hardness test procedure. An estimation method is described to determine the number of coils inside the electromagnets and their interior geometry. A power supply and cold plate were built to energize the electromagnets and control their temperature. The load frame and sample hanger used to test the attractive forces generated by the electromagnets and the magnetic rubber is described. Magnetic instrumentation used in the experiments is also described including a handheld

Gaussmeter and Lakeshore vibrating sample magnetometer. Figure 4.1 shows the experimental setup used to measure the attractive forces. With labels on the magnetic rubber sample, the electromagnet, the cold plate, and the nonmagnetic hanger, which is pinned to a load cell (not shown).

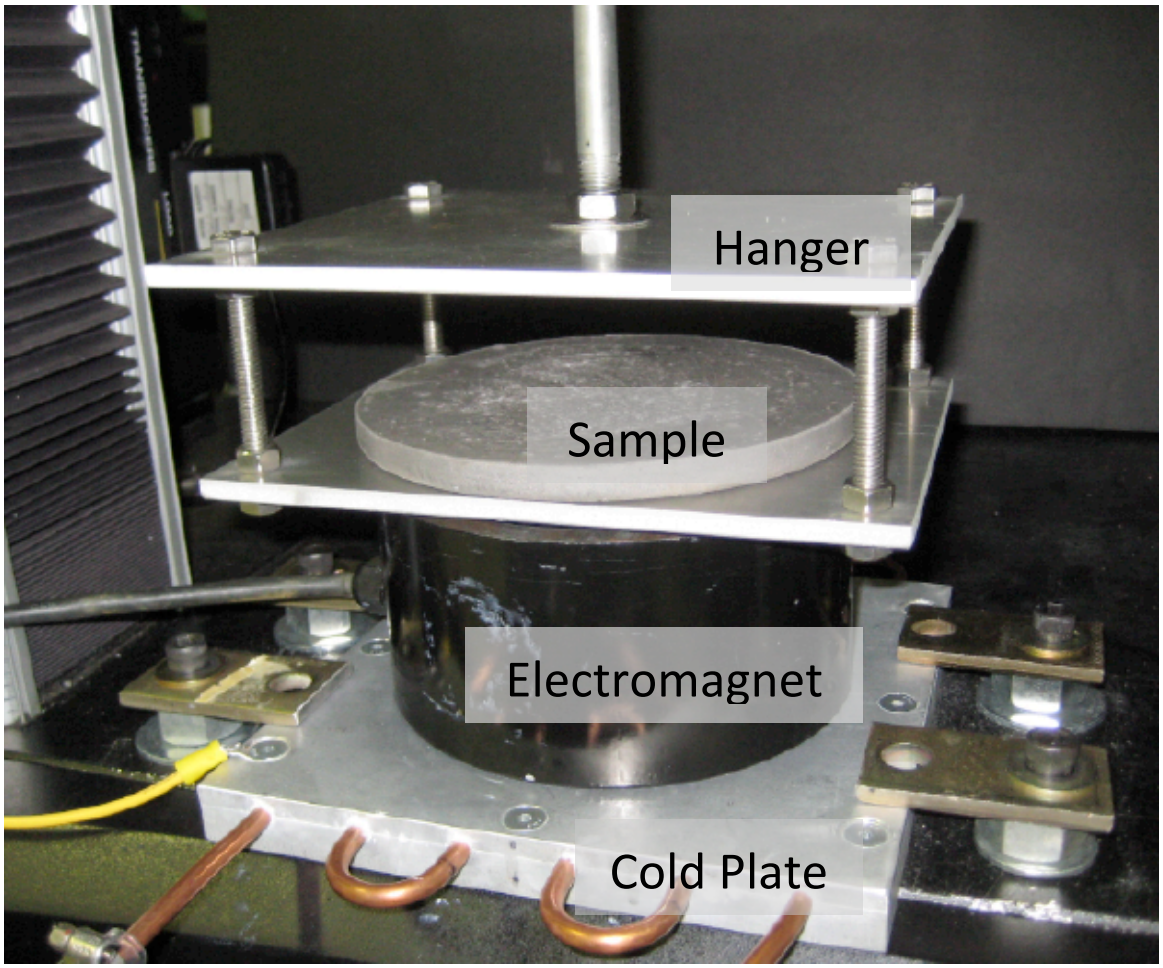

Figure 4.1 Experimental apparatus: sample with hanger, 6" electromagnet, and cold plate

4.1.1 Electromagnets

Electromagnets are used to generate the magnetic fields that developed by forces in the magnetic rubber intended for use in the composite clamping device. Two sizes of round electromagnets supplied by Magnetech are used in the experiments. Both are

round, flat-faced lifting electromagnets designed to operate with a 12 VDC power supply. A 6” diameter electromagnet, model R-6030-12, is used to perform large-scale tests and a set of 1” electromagnets, model R-1007-12, are used to determine model scalability and perform tests in array configurations. Images of the two electromagnets are shown in Figure 4.2.

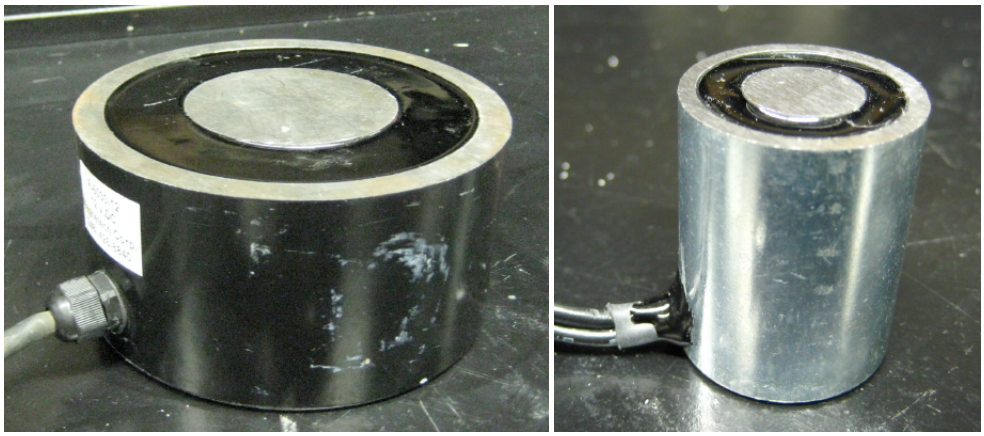

Figure 4.2 6” Electromagnet (Left) and 1” Electromagnet (Right)

The terminology regarding the construction of electromagnets may be found in section 3.1. The following sections provide the details of the electromagnets including construction materials, geometry, power requirements, and cooling. Methods to determine the type of steel and the number of coils in the electromagnets are outlined. Supporting devices including a cooling plate and power supply are also discussed.

As discussed in section 3.3.1, low carbon steels are usually chosen for electromagnet construction due to their high saturation fields, magnetic softness, and ease of manufacture. Mild steels such as 1010, 1018, 1035, and 1040 have very similar BH curves and may be modeled quite accurately with a single BH relationship, shown in

Figure 3.2. A hardness test was performed on the steel encasing of a 1” diameter round electromagnet in order to determine if it is a mild steel. A Buehler microhardness device, model 1600-6406, was used to perform the hardness test. The device operates by indenting a sample with a pyramid-shaped indenter with 2 kgf. An optical scope allows measurement of the lengths between the corners of the indent. The device then calculates the hardness and reports it in a Vickers scale (HV). The results were correlated to the Brinell hardness (HB) scale for ease of comparison with published data. Ten tests were performed at different points of the core of the electromagnet. A 95% confidence interval for the hardness was calculated and is shown in Table 4.1.

Table 4.1 Hardness comparison of 1” magnet core and standard cold drawn low carbon steels (ASM Metals Handbook, 1978)

AISI name	Brinell Hardness (HB)
Experimental Data	**162-171**
1018	101-143
1035	131-179
1040	143-187
1045	149-197
1050	163-212
1141	170-223
1144	179-229

Table 4.1 displays the hardness ranges of some ubiquitous low carbon steels against the hardness range of the electromagnet. The data show that it is reasonable to conclude that the electromagnet is a low carbon steel since the hardness ranges of a number of widely available low carbon steels encompass the experimental hardness interval. Only the 1018 and 1144 steels seem to be unlikely choices. However, all of the listed steels have very similar magnetic properties. The electromagnet steel is therefore

assumed to follow the general BH relationship of low carbon steel as shown in section 3.2.

The total magnetomotive force (*mmf*) generated by an electromagnet is found by multiplying the number of coils *N* by the exciting current *I* through them. In order to predict the performance of an electromagnet, both values must be known accurately. Coil information for both the 1" and 6" round electromagnets was not provided by the manufacturer. A coil number estimation method was used to predict *N* using the resistance of the coil pack and the geometric constrains of the windings. A 1" electromagnet was cut open to validate the coil number estimation method. The method was also used to estimate N for the 6" electromagnet. The larger electromagnet was not destroyed to verify the estimation; the results of for the smaller electromagnet were accurate and the large electromagnet was far more expensive than the small ones.

Slots of 0.25" diameter were milled along the top and side of the 1" electromagnet to reveal its interior geometry. Figure 4.3 shows the dimensions of the interior features of the 1" round electromagnet.

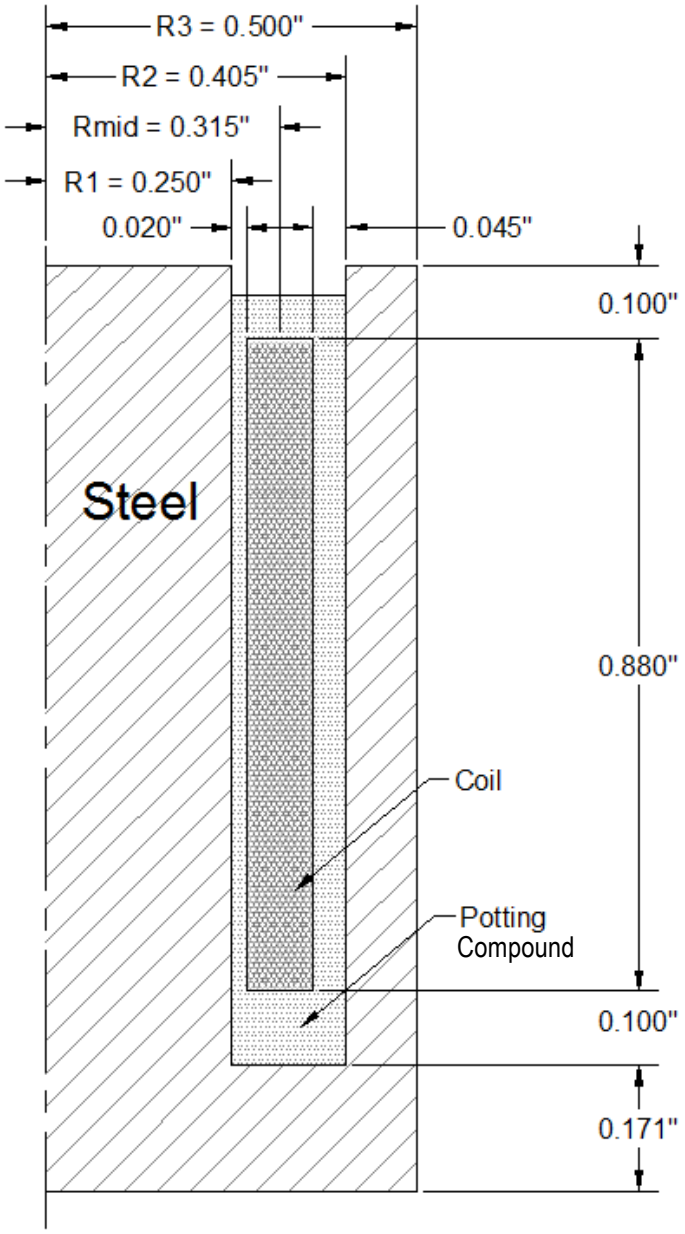

Figure 4.3 Dimensions of 1” electromagnet in cross section (to scale)

The centerline indicates the axis of symmetry at the center of the electromagnet. The coil pack is offset on all sides from the back iron and filled with urethane potting compound for insulation. It should be noted that the potting compound does not fill the coil pack but merely surrounds it. The top and bottom of the coil is offset by 0.1” of potting compound while the inner and outer radii are offset by 0.02” and 0.045”, respectively. Of primary

interest is the radius of the center of the coil, r_{mid} = 0.315", which is used to determine the average coil circumference. Also, the yoke thickness of the electromagnet was measured to be 0.1705". This dimension is in agreement with standard electromagnet design for yoke thickness, y, which is given by Equation 4.1,

$$y = \frac{r_3^2 - r_2^2}{2r_1} \tag{4.1}$$

where r_1 is the radius of the core, r_2 is the inner radius of the pole, and r_3 is the outer radius of the pole. This relationship causes the reluctance of the core, yoke, and pole to be roughly equal so there is no unnecessary flux constriction or wasted metal (Roters, 1941). Equation 4.1 predicts y = 0.172" which is only 1% over the actual thickness. As the yoke thickness of the smaller electromagnet was correctly estimated with the equation, it was also used to estimate the yoke thickness of the 6" electromagnet as 0.81".

Figure 4.4 shows the measured dimensions of the core and pole and the calculated dimensions of the yoke. The 6" electromagnet was not destructively investigated so the exact dimensions of the surrounding potting is unknown. However, it was estimated from the construction of the 1" electromagnet that the upper and lower potting offset of the 6" electromagnet is 0.1" and the offset on the sides is 0.05". The exact potting offset dimensions are not critical to the coil number estimation method or for FEA modeling.

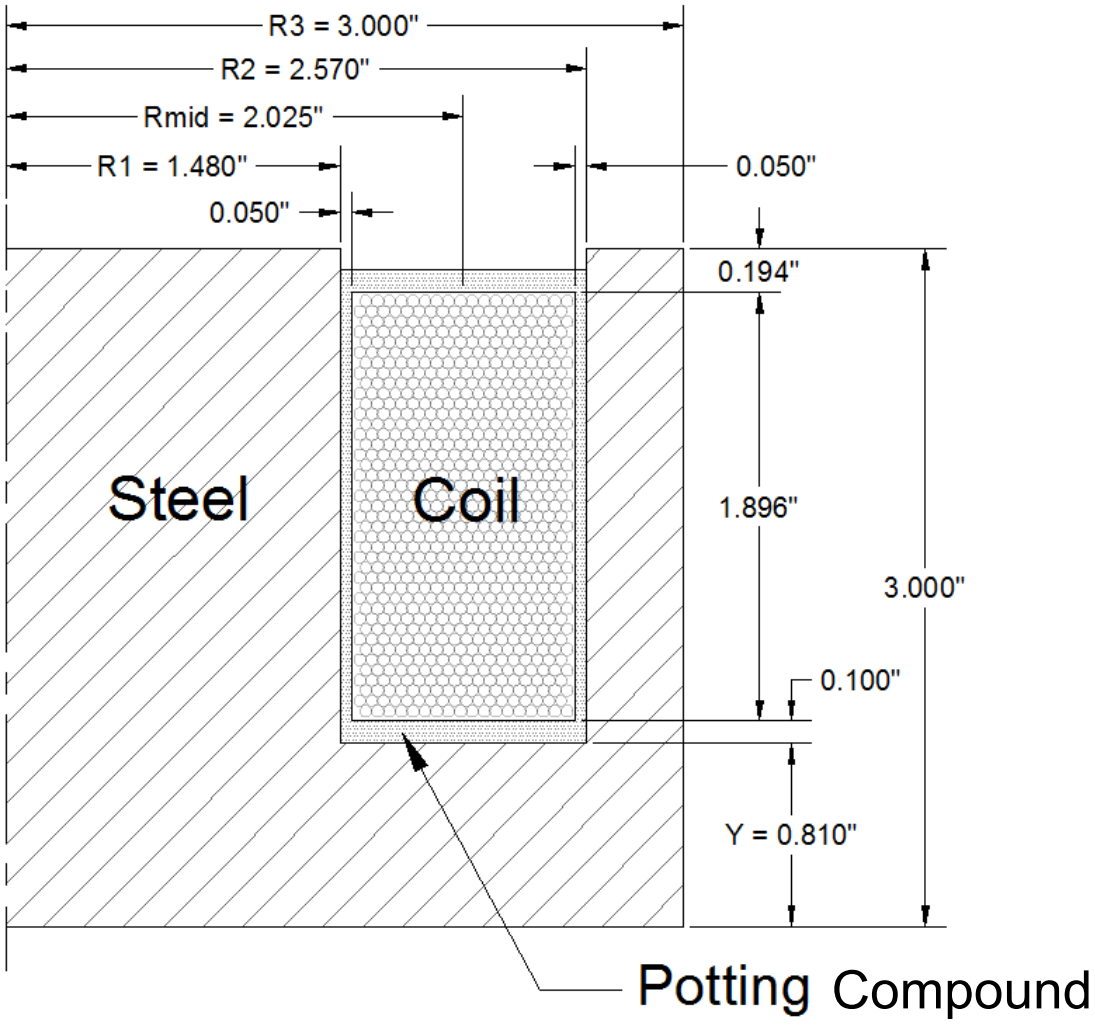

Figure 4.4 Dimensions of 6" electromagnet in cross section (to scale)

The coil number estimation method involves four steps. First, the electrical resistance, R, and the center radius, r_{mid}, of the coil pack are measured. These are the two main values necessary for estimation. Secondly, the dimensions of AWG single-build copper magnet wire are used for resistance comparison. The nominal diameter of the solid copper, d_{copper}, and the total outer diameter including the enamel coating, d_{wire}, for such wires are tabulated in Tables 4.2 and 4.3. It is assumed that single-build magnet wire (standard insulation coating thickness) is employed because it allows for the most efficient electromagnet construction. The room-temperature resistivity of copper, ρ =

0.6717 μΩ-inch, is used to calculate the total length of the wire in the coil, l, by the following equation:

$$R = \frac{\rho l}{A_{wire}} \tag{4.2}$$

where A_{wire} is the cross sectional area of the wire. Thirdly, the number of coils for each possible magnet wire type is calculated using the following:

$$l = 2\pi r_{mid} N \tag{4.3}$$

Equation 4.3 shows that the total length of the wire is equal to N times the circumference of the coil pack at its center, r_{mid}. Finally, an area comparison is used to determine the wire size. The cross-sectional area of the measured coil pack space, A_{space}, is compared with the necessary cross-sectional area of a coil comprised of N coils of a certain wire size, A_{coils}. The necessary coil area is calculated with Equation 4.4 using the total wire diameter and a coil packing factor, p_f.

$$A_{coils} = \frac{\pi d_{wire}^2}{4 p_f} \tag{4.4}$$

The wire size that causes the ratio of the two areas to be close to unity is the most plausible one.

Table 4.2 shows the progression of the four coil number estimation steps for each possible AWG magnet wire size (ANSI/NEMA, 2008). The resistance of the 1" diameter electromagnet was measured to be 41.6 Ω. Larger diameter wires have lower resistance per unit length and therefore result in a higher prediction of N, which is based on the total resistance of the electromagnet. The packing factor reduces slightly for smaller wires (Roters, 1941).

Table 4.2 Coil number estimation for 1” electromagnet

AWG	d_{copper} (in)	d_{wire} (in)	length (in)	N
30	0.01000	0.01095	4863.9	2458
31	0.00890	0.00975	3852.7	1947
32	0.00800	0.00880	3112.9	1573
33	0.00710	0.00785	2451.9	1239
34	0.00630	0.00700	1930.5	975
AWG	p_f	A_{space} (in^2)	A_{coils} (in^2)	**ratio**
30	0.80	0.0769	0.2893	0.27
31	0.80	0.0769	0.1817	0.42
32	0.79	0.0769	0.1211	0.64
33	0.79	0.0769	0.0759	1.01
34	0.78	0.0769	0.0481	1.60

AWG 33 magnet wire calculations result in a space ratio very close to unity. One wire size up and down results in ratios of 0.64 and 1.60, respectively, which makes the choice of AWG 33 obvious. The intermediate calculation values for AWG 33 are highlighted in the table. The method results in a coil number estimation of $N = 1239$ for the 1” electromagnet.

A length of magnet wire was extracted from the 1” electromagnet and the diameter was measured to be $d_{wire} = 0.0078$”. The wire was verified to be AWG 33 single-build film insulated magnet wire, the dimensions of which are shown in Table 4.2. Experimental knowledge of the wire size confirms the validity of the coil number estimation method.

The coil estimation method was applied to the 6” electromagnet, the dimensions of which are shown in Figure 4.4. The resistance was measured as 3.35 Ω. Table 4.3 displays the calculation procedure for finding N of the 6” electromagnet. The dimensions of the electromagnet are shown in Figure 4.3.

Table 4.3 Coil number estimation for 6” electromagnet

AWG	d_{copper} (in)	d_{wire} (in)	length (in)	N
14.5	0.06050	0.06250	14336.6	1127
15	0.05710	0.05900	12770.5	1004
15.5	0.05340	0.05630	11169.1	878
16	0.05080	0.05265	10108.0	794
16.5	0.04800	0.04980	9024.4	709
17	0.04530	0.04710	8037.7	632
AWG	p_f	A_{space} (in^2)	A_{coils} (in^2)	**ratio**
14.5	0.90	1.877	3.841	0.49
15	0.90	1.877	3.049	0.62
15.5	0.90	1.877	2.428	0.77
16	0.90	1.877	1.922	0.98
16.5	0.90	1.877	1.535	1.22
17	0.90	1.877	1.223	1.54

A packing factor of 0.9 is used for all of the wire sizes considered. Larger wires may be packed more efficiently than small wires and are limited by the hexagonal circle packing factor of 0.906. As in the case of the 1” electromagnet, inspection of the area ratio column shows that only AWG 16 wire that satisfies the area constraints. The results of the AWG 16 calculations are highlighted in the table. A coil number of $N = 794$ is the final result of the procedure and the area ratio is very close to unity which further validates the result.

In brief summary, the number of coils of the two types of electromagnets was determined. The necessary length of wire to make up the total resistance of each electromagnet was calculated and compared with the possible packing configurations for different AWG magnet wire sizes. The number of coils in the 6” and 1” electromagnets was found with reasonable certainty to be 1239 and 794, respectively. These values are used in the FEA models of the electromagnets along with the interior geometric details.

4.1.2 Power Supply and Cold Plate

The electromagnets used in the experiments were subjected to high currents in order to study the response of the magnetic rubber material to high magnetic fields. A DC power supply was constructed to supply up to 20A at 80V to the electromagnets. The electromagnets are designed to operate continuously at 12V with only natural convection cooling. Thermal management is required to drive the electromagnets with more than 12V for any significant time. A water-cooled cold plate was built to control the temperature of the electromagnets when operated at higher voltage. This section provides details about the construction and operation of the power supply and cold plate, which were successfully used to increase the operating current of the electromagnets and allow greater flexibility in experimentation.

The power supply consists of a variac and an AC-to-DC converter. The variac is used to set the AC voltage applied to the converter and is limited to 20A. The converter is constructed of a 35A, 600V bridge rectifier with a 470 μF, 160V capacitor in parallel. The rectifier dissipates heat to an aluminum plate that is grounded to the variac. During operation, the current through the 6" electromagnet is measured with an Extech 38389 clamp-on ammeter. The ammeter is positioned on one of the main leads to the electromagnet. The current in the 1" electromagnet is measured with a Fluke 8050A digital multimeter.

A cold plate is used to cool the electromagnets during operation. The device is constructed of two 8" square aluminum plates that sandwich six lengths of 0.25" copper tube. The plates have half-circle channels milled into them that hold the tubing securely. Silicone-based thermal grease is applied between the plates and tubes to take up any air

space and maximize heat transfer. Figure 4.5 shows the 6” electromagnet installed on the cold plate in the test frame.

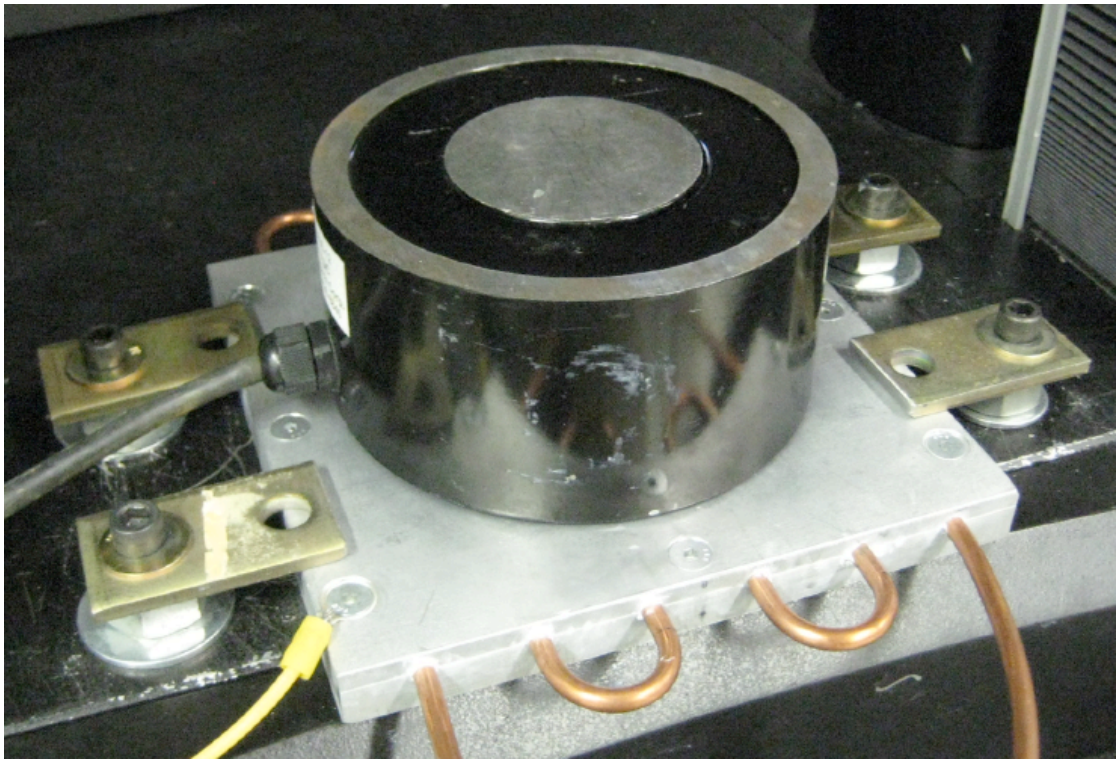

Figure 4.5 6” Electromagnet on cold plate

A 5/8” bolt fastens the cold plate to the bottom of the electromagnet. The four clamps on the sides are used to restrain the device. The wire in the bottom left of the figure is the ground wire for the cold plate. Faucet water at 20°C flows through the tube at a rate of 1.3 gallons per minute. At continuous 12V operation with only natural convection, the surface temperature of the electromagnets reaches about 80°C. Use of the cold plate reduces the 12V steady state surface temperature to about 30°C. The 80V power supply and cold plate allow the 6” electromagnet to be driven with 20A for a few seconds or at 6.5A continuously; the 1” electromagnets may be driven at 2A briefly or at 0.7A continuously. Forced cooling also allows for high-current experimentation to be

performed much more rapidly as the electromagnet must be allowed time to cool between measurements. The continuous amperage values possible with cooling were determined by incrementally increasing the applied current until the resistance of the electromagnet became unstable due to Joule heating. The power dissipated by electrical resistors is known to be I^2R, where R is the resistance and I is the current through the resistor. As such, use of the cold plate allows the electromagnets to be driven at more than four times their intended power.

4.1.3 Load Frame and Hanger

An Instron, model 33R4466, with a 500N load cell is used to measure the attractive forces generated between the electromagnets and samples of the magnetic rubber. A non-magnetic hanger suspends the magnetic rubber directly over the electromagnets.

Figure 4.6 shows the setup used to measure the forces generated by the electromagnets. This particular setup shows the cold plate and three 1" electromagnets mounted to the base of the Instron frame. The crossbar of the Instron holds the load cell that measures the tensile force in the system. The hanger consists of a 14" aluminum rod of 0.5" diameter that is pinned to the load cell and two parallel aluminum plates. The length of the rod prevents the load cell from experiencing a significant magnetic field from the electromagnets. The lower section of the rod is threaded and is connected to two 6"x8" aluminum plates. The plates are spaced 4" apart with stainless hardware.

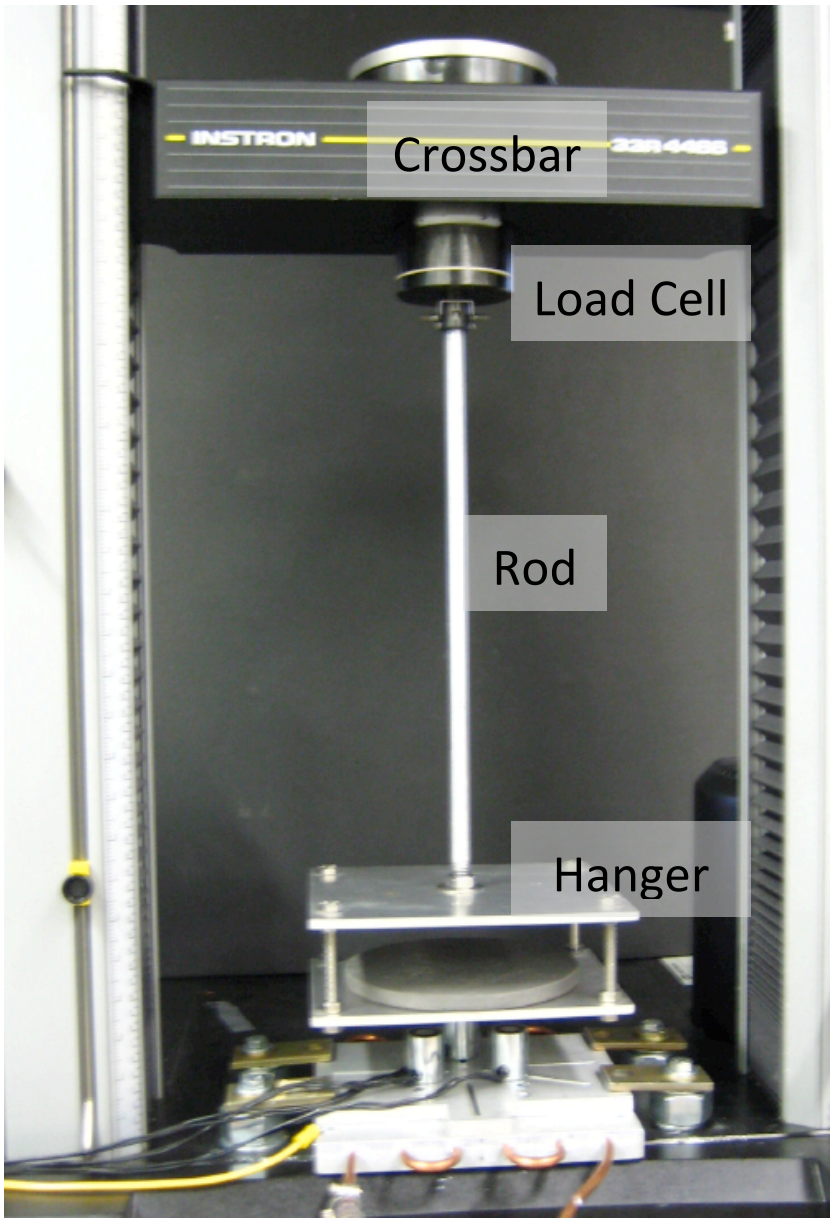

Figure 4.6 Experimental setup for attractive force measurements

The lower plate of the hanger holds the magnetic rubber sample over the electromagnets as shown in the figure. The vertical position of the crossbar is adjusted to position the sample with the desired air gap from the face of the electromagnet. In the maximum possible field, the hanger experiences an attractive force of only 0.25 N. This maximum field occurs at a minimal air gap over the 6" electromagnet at 20A of applied current. The

force is due to the slight magnetization of the stainless hardware. However, the effect is small enough to be considered negligible.

While the 6” electromagnet is bolted directly to the cold plate, the 1” electromagnets are mounted via an intermediate slotted plate. The slotted plate allows either one electromagnet to be mounted in the center, three to be mounted along slots with 120° spacing, or four to be mounted on slots with 90° spacing. In this way hexagonal and square electromagnet arrays may be mounted accurately. The intermediate plate is made of aluminum and is securely fastened to the cold plate in order to maintain heat transfer between the electromagnets and the cold plate. Figure 4.7 displays the intermediate plate shown for mounting the 1” electromagnets. The left hand image shows three electromagnets in a hexagonal configuration mounted to the cold plate. The right hand side shows the underside of the intermediate plate.

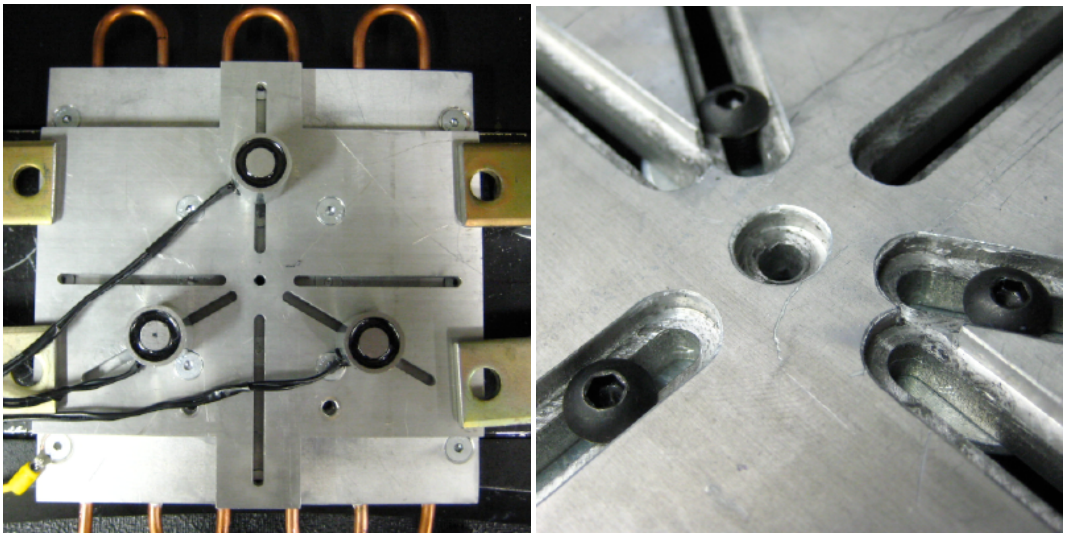

Figure 4.7 Intermediate plate shown mounted (left) and detail (right)

Six slots with recesses for #10-32 button head cap screws are milled into the plate to allow for secure and accurate mounting of the electromagnets. The central hole also

allows a 1” electromagnet to be mounted in the center of the plate for experiments requiring a single electromagnet.

4.1.4 Gaussmeter and Probe

The field in the gap between the magnetic rubber and the electromagnet is measured directly in order to provide a comparison with the FEA modeling results. A handheld Alphalab Trifield DC magnetometer, serial #3075, is used to measure the field. A probe is attached to the magnetometer, or Gaussmeter, which contains a transversely mounted Hall effect meter. The presence of a magnetic field normal to the Hall effect meter causes a voltage differential in it, which is read by the Gaussmeter and displayed in units of Gauss. The center of the Hall effect meter is 0.75mm from the face of the probe. This dimension is important for accurate comparison with the FEA model.

4.1.5 Vibrating Sample Magnetometer

As discussed in the theory section, the intrinsic response of a ferromagnetic material determines how it will respond to an applied magnetic field. In order to predict the forces generated in a magnetizable structure the BH curves of the involved materials must be known. A Lakeshore vibrating sample magnetometer (VSM) system was used to measure the BH curves of magnetic rubber with varying high-purity iron powder loading percentages. The VSM contains two large, water-cooled field coils that generate up to a 1 Telsa B-field in a 3” gap between them. A thin quartz rod is used to suspend a small sample in the gap. The rod is fixed to a head drive that oscillates the sample at a fixed frequency. The head drive is manually adjusted in order to position the sample in the region of most uniform field, the very center of the gap between the field coils. A Gaussmeter records the disruption of the field in the gap due to the harmonic motion of

the magnetized sample. Lakeshore VSM software controls B-field values and records the magnetic moment, *m*, of the sample. A built-in script ramps the field from -1T to 1T and records *m* at 101 points.

A sample of volume *V* magnetized with a magnetic moment of *m* experiences a magnetization field of $M = m/V$. In other words, *m* represents total magnetization while *M* represents volumetric magnetization. The VSM measures *m*, in units of emu (electromagnetic unit), of a sample within a field *B*, in units of Gauss. The VSM output of emu vs. Gauss is converted to the standard SI convention for BH curves of Tesla vs. A-t/m. Recalling section 5.1, in air *B* and *H* fields are the same because no magnetization term is present. As such, the field between the coils may be expressed simply in terms of applied field, *H*, using equation 5.1. The total induced B-field, *B*, within the sample is found with equation 5.2, which sums the applied field and the magnetization field. The BH curve of the sample is then given by *B* vs. *H*. Details about the samples measured by the VSM are given in the next section.

4.2 Magnetic Rubber Material

The magnetic rubber used in the clamping structure is a two-part silicone rubber filled with ferromagnetic powder. This section describes the constituent materials and the fabrication process. Various samples were made in order to determine the effects of filler material, filler loading level, and sample thickness on the forces developed by the material in a magnetic field. The details of the samples are described in this section. The magnetization curves of the material as measured by the VSM also are presented and discussed here.

4.2.1 Constituent Materials

Rebound 25 silicone rubber by Smooth-On was used as the matrix material in the magnetic rubber. Silicone elastomers can endure high strain, are chemically and thermally resistant, may be easily mixed and cast, and are often able to cure in confinement. The rubber involves two liquid parts that are mixed in equal weights. Low-viscosity silicone oil was added to the mixture to thin it out and allow the powder fillers to be mixed in more easily. Addition of the oil also softens the cured rubber. Four ferromagnetic powder fillers were used in the samples. Nickel powder, Permalloy powder, and low-purity iron filings were used for initial filler material selection experiments. High-purity iron powder was used in the samples that are involved in the majority of the experiments.

4.2.2 Sample Fabrication

Samples of magnetic rubber material were fabricated with varying amounts of filler material at different thicknesses. The two parts of the silicone rubber were measured on a gram scale and thoroughly mixed by hand. Silicone oil was weighed and mixed in. Greater amounts of oil were used for higher filler fraction samples to aid in the mixing process. The powder filler material was weighed and added to the mixture gradually and stirred at intervals. Low volume fraction samples, such as 15%, remained relatively thin while those of higher volume fraction were highly viscous. After weighing and mixing, the material was poured into a 158mm diameter straight-walled aluminum pan. The pan was filled to a marked level such that the desired sample thickness was obtained. The filled pan then was transferred into a vacuum chamber for degassing. The chamber was evacuated with a vacuum pump and left for 30 minutes. The pan was removed and

allowed to cure overnight in room temperature and atmospheric pressure conditions. The sample was then removed from the pan. The degassing step aids in the removal of voids from the bulk of the sample. However, more heavily loaded samples were difficult to degas due to high viscosity and more voids remained.

The first set of samples was made in order to compare the effects of filler material type. Seven samples of 158mm diameter and 4mm thickness were cast with nickel, permalloy, and low-purity iron filing fillers. Three samples were filled with Novamet type CHT nickel flakes, -325 mesh and 10μm thickness, at 25%, 50%, and 75% by weight. One sample was filled to 25% by weight with Novamet permalloy flakes. Higher loadings were not used since the filler did not mix well with the rubber. Coarse, low-purity iron filings supplied by Master Magnetics were used in three samples, which were filled to 25%, 50%, and 75% by weight. The results the comparison test, discussed in section 7, indicate very clearly that iron is the superior filler material shown by the measured attractive forces.

The second set of samples was fabricated with 99+% purity, < 200 mesh (diameter < 74 μm) iron powder by Alfa Aesar. Five 158mm diameter samples were cast to test the effects of filler volume fraction and sample thickness on magnetic forces. Thick (~10mm) and thin (~6.5mm) samples were made with a nominal filler volume fraction of 30% and 15% as well as one thick 23% sample. Table 4.4 provides the dimensional and filler details of the five iron powder filled samples. Samples 1, 3, and 4 are the “thick” bags and samples 2 and 5 are the “thin” bags. The actual thicknesses and diameters are shown in the table.

Table 4.4 Details of samples filled with high-purity iron powder

	Sample #	**1**	**2**	**3**	**4**	**5**
Nominal Iron V.F. %		30	30	23	15	15
Thickness (mm)		10.7	6.5	10.2	10.1	6.4
Diameter (mm)		158	158	158	158	158
Product	Density (g/cc)	Weight % of Product				
Silicone Oil	0.97	5.65	4.62	7.94	12.81	12.84
Part B	1.17	8.91	9.57	11.20	14.58	14.59
Part A	1.17	8.97	9.59	11.20	14.57	14.59
Fe Powder	7.874	76.47	76.23	69.66	58.04	57.98
		Measurements of Samples				
Mass (g)		622.3	399.4	517.5	411.3	270.1
Volume (cc)		209.8	127.4	199.5	197.0	125.5
Void Volume (cc)		18.0	4.4	12.3	9.9	2.5
Void Volume %		8.6	3.4	6.2	5.0	2.0
Density (g/cc)		**2.97**	**3.13**	**2.59**	**2.09**	**2.15**
Iron Volume Fraction (%)		**28.9**	**30.4**	**23.2**	**15.5**	**15.9**

The weight percents and densities of the constituent products that were measured during the fabrication process are included. The densities of the final parts were compared with their theoretical densities calculated from the product weight percentages in order to determine the volume of the voids. Void percentages increase for more heavily loaded samples and for thicker samples. This is reasonable because loading increases viscosity and bubbles have farther to travel in thicker parts. With knowledge of the void content, the actual iron volume fraction, ϕ, is calculated. These values, shown on the bottom row, deviate slightly from the nominal volume fractions. The calculated density is used in the next section to determine the volume of the samples measured in the VSM.

4.2.3 VSM Tests of Rubber Samples with High-Purity Iron Filler

Small pieces of the magnetic rubber were cut from the sides of the three thick rubber samples (numbers 1, 3, and 4). The pieces are very small; at most 3mm square and

0.7mm thick. The volume of each sample piece is calculated from its mass and the density of the bulk sample from which it was cut. This method provides better accuracy than measuring the dimensions of the samples directly.

Figure 4.8 displays the results of the VSM tests performed on the sample pieces cut from the three thick bulk rubber samples.

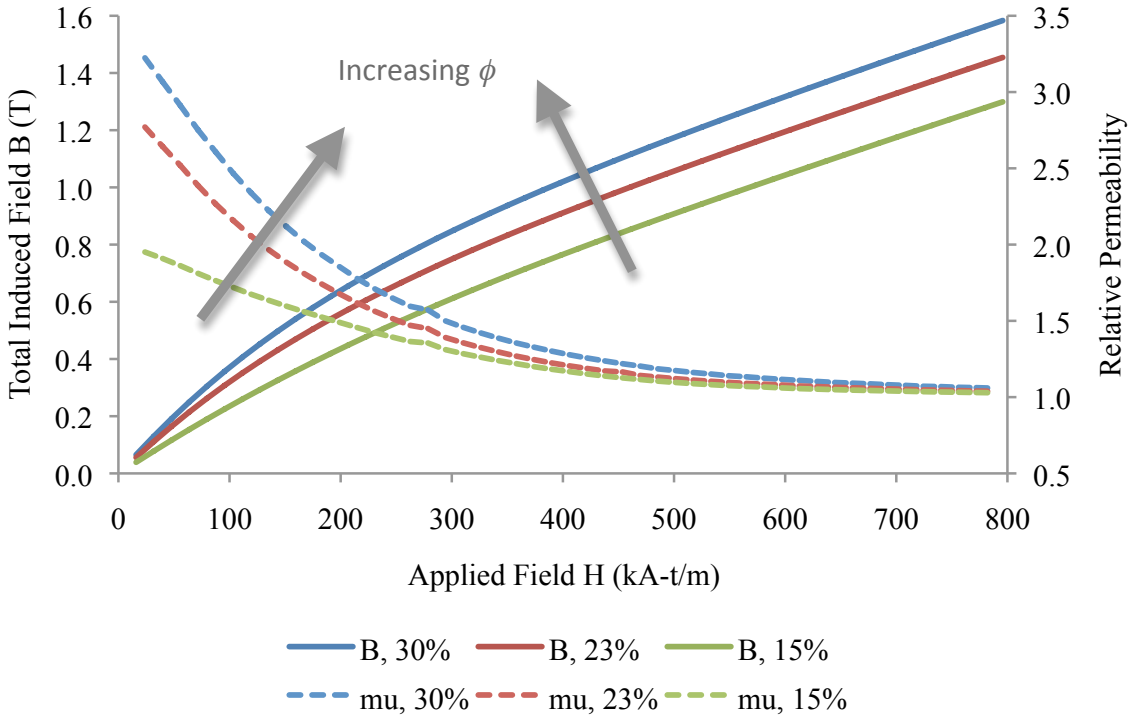

Figure 4.8 Plot of BH curves and relative permeability curves from VSM measurements of thick, iron powder filled sample pieces

The solid curves are the BH curves of the three materials. The results have been converted to SI units by the method described in section 4.1.5 using the volumes of the pieces, shown in Table 4.5. All three BH curves become nearly linear above H = 500 kA-t/m. As expected, samples of higher loading percentage show greater magnetization. The dashed lines display the relative permeability of the samples as a function of applied field. As discussed in section 3, the permeability is essentially the derivative of the BH

curve. Samples with higher loadings display higher permeability at all applied field values. All three fall asymptotically to a value of unity. Around H = 275 kA-t/m there is a small deviation which is due to an auto-ranging error in the Lakeshore system. The BH curves are used as the magnetization models in the FEA model in ANSYS.

Table 4.5 shows important information about the VSM test pieces cut from the bulk samples including the measured mass and the calculated volume.

Table 4.5 Mass, density, and saturation B-field of VSM samples

Sample Number	1	3	4
Nominal Loading (%)	30	23	15
Mass (g)	0.0165	0.0073	0.0046
Bulk Density (g/cc)	2.97	2.59	2.09
Volume (mm^3)	5.56	2.81	2.20
Actual Loading (%)	28.9	23.2	15.5
B_{sat}, Theory (T)	0.622	0.499	0.332
B_{sat}, Actual (T)	0.583	0.454	0.299

The validity of the measured BH curves may be verified by inspection of the saturation flux density, B_{sat}. Recalling Equation 3.16, the saturation field of a magnetic composite has been shown to be equal to the volume fraction of the filler times the saturation field of the filler. Given that iron saturates at 2.15 T, the theoretical saturation fields are shown in the table. The actual observed saturation field is shown for comparison. Note that B_{sat} here does not include the response of vacuum; it is the magnetization of the material, equivalent to $B_{total} - \mu_0 H$. The observed B_{sat} values are all close to the theoretical values and show proportionality with the loading percentage. The observed values are slightly less than the theoretical values because the sample material was not fully saturated by the VSM, as evidenced by the fact that the three relative permeability curves shown in Figure 4.8 have not entirely decayed to a value of unity. This discrepancy is minor, however,

and it is concluded that the observed saturation flux densities of the magnetic rubber samples are in accord with the theoretical expectations.

4.3 ANSYS FEA Model

A finite element analysis (FEA) model was developed in ANSYS v.11 to numerically model the magnetic field phenomena involved in the magnetic clamping device. The ultimate purpose of the FEA field model is for use as a design tool for the clamping device. The model must predict with reasonable accuracy the pressure developed by the device with inputs such as rubber and part thickness, applied current, magnetization models, and electromagnet geometry. The model was constructed initially to simulate a set of experimental conditions in order to verify the model's accuracy. Comparisons are drawn in section 7 and magnetic circuit calculations are used for secondary validation. Validation of the model allows for further characterization of the developed pressures, including high-field predictions and structural modeling. This section explains the construction of the model, boundary conditions, solution method, and convergence of the model mesh.

FEA modeling was used to solve the magnetic field problem and determine the forces caused by the field. Structural modeling was not performed, however, as it lies outside of the scope of this thesis. The field model solves the static magnetic field problem presented by an applied magnetomotive force and a set of boundary conditions. Magnetization material models are applied to the field model. This model provides the details of the *B*-field and *H*-field within the elements and displays the flux paths throughout the entire model. ANSYS predicts the forces developed by the magnetic field at the element nodes. A macro is employed to calculate the total force developed on a

specified component. For future work, structural modeling may be accomplished by applying the nodal forces found in the field model to a similar model using structural elements.

4.3.1 FEA Model Construction

Round electromagnets and magnetic rubber samples are used in the experiments. As such, a 2D axisymmetric modeling technique is used to model the experimental geometry in order to compare the model predictions with experimental results. 2D axisymmetric modeling offers significant benefits in simplicity and computational expense over a 3D model. Both the 1" and 6" electromagnets are modeled. The electromagnets are modeled with the exact geometries shown in Figures 4.3 and 4.4, including the airspace of the potting material. The rubber material of appropriate thickness is modeled with an air gap above the face of the electromagnet. Airspace is included around the outside of the system in order to simulate flux leakage and is modeled with a coarser mesh in order to minimize computation time. Linear and quadratic quadrilateral ANSYS magnetic elements, PLANE13 and PLANE53, respectively, were used to perform the field modeling. Linear elements offer the advantage of reduced computational expense compared to quadratic elements. The two are compared in the 4.3.3 mesh convergence section.

4.3.2 FEA Model Solution Method

This section explains the application of material models, boundary conditions, and applied loads in the field models. The steps taken to obtain solutions and necessary calculations also are discussed.

Relative permeability of unity is applied to the nonmagnetic materials including the air, coil, potting compound, and part. The magnetization models of the electromagnet steel and the magnetic rubber are applied to the corresponding regions. The steel and rubber BH curves that are used are shown in section 3.2.1 and 4.2.3, respectively. It is assumed that the materials have isotropic magnetic properties. Figure 4.9 shows a typical FEA model in ANSYS of the 6" round electromagnet.

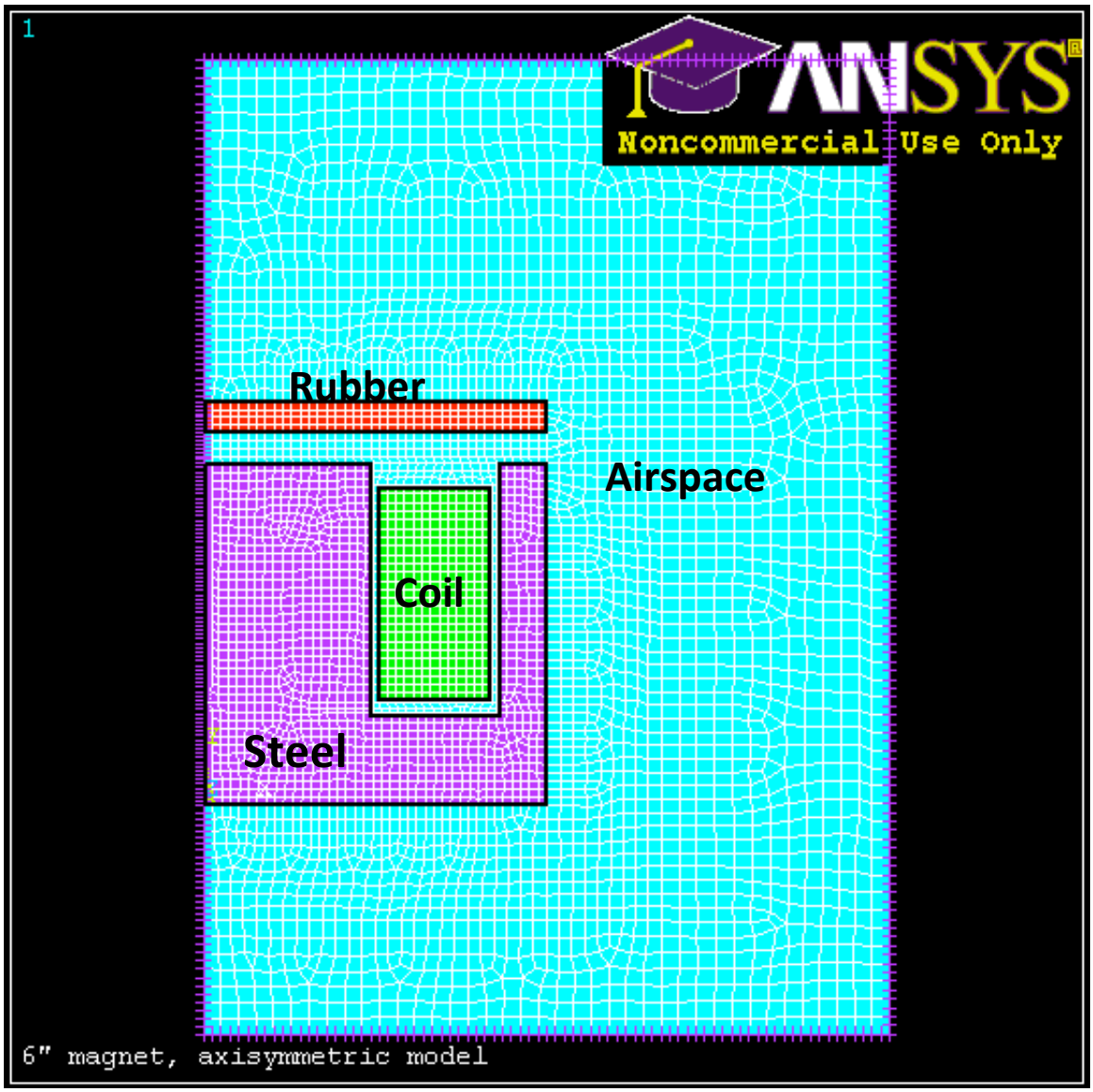

Figure 4.9 ANSYS model of 6" electromagnet

The left-hand edge of the model is the axis of symmetry. The model contains the electromagnet steel, coil, rubber armature, and air spaces, which are labeled in the figure. Borders are drawn around the different components for clarity. The rubber is separated from the face of the electromagnet by an air gap. The elements shown in the inner region, which includes the rubber, coil, steel, and potting space, are nominally 2mm square. The element mesh transitions to a larger 4mm square size in the outer region as seen in the figure.

A current density load, J, is applied to the electromagnet coil region, shown in Equation 4.5,

$$J = \frac{NI}{A_{coil}} \tag{4.5}$$

where N is the number of coil windings, I is the applied current, and A_{coil} is the cross-sectional area of the coil region. The value for N is chosen appropriately from the coil number estimation methods from section 4.1.1b. A flux-parallel boundary condition is applied to the exterior nodes. In Figure 4.9, this condition is indicated by the small dashes normal to the boundaries of the model. Essentially, the flux-parallel condition forces the flux lines to stay within the geometric scope of the model; flux lines cannot cross the outer boundary. This condition is necessary on the left-hand side of the model because it is the axis of symmetry. Airspaces are included on the top, bottom, and right-hand side to visualize flux leakage phenomena. The air spaces are large enough that essentially all of the flux generated by the *mmf* is contained naturally within the bounds of the model. In other words, the flux-parallel boundaries are far enough apart that the flux solution is not forced to bend unnecessarily to fit within the constraints.

Figure 4.10 shows the ANSYS model of the 1” round electromagnet. This model is validated with force experiments in the same manner as the 6” electromagnet model. All of the features of the large model are included such as the electromagnet features and surrounding air space. The primary difference is that the rubber material extends well beyond the face of the electromagnet since the same 158mm diameter rubber samples were used for all the 1” electromagnet force experiments.

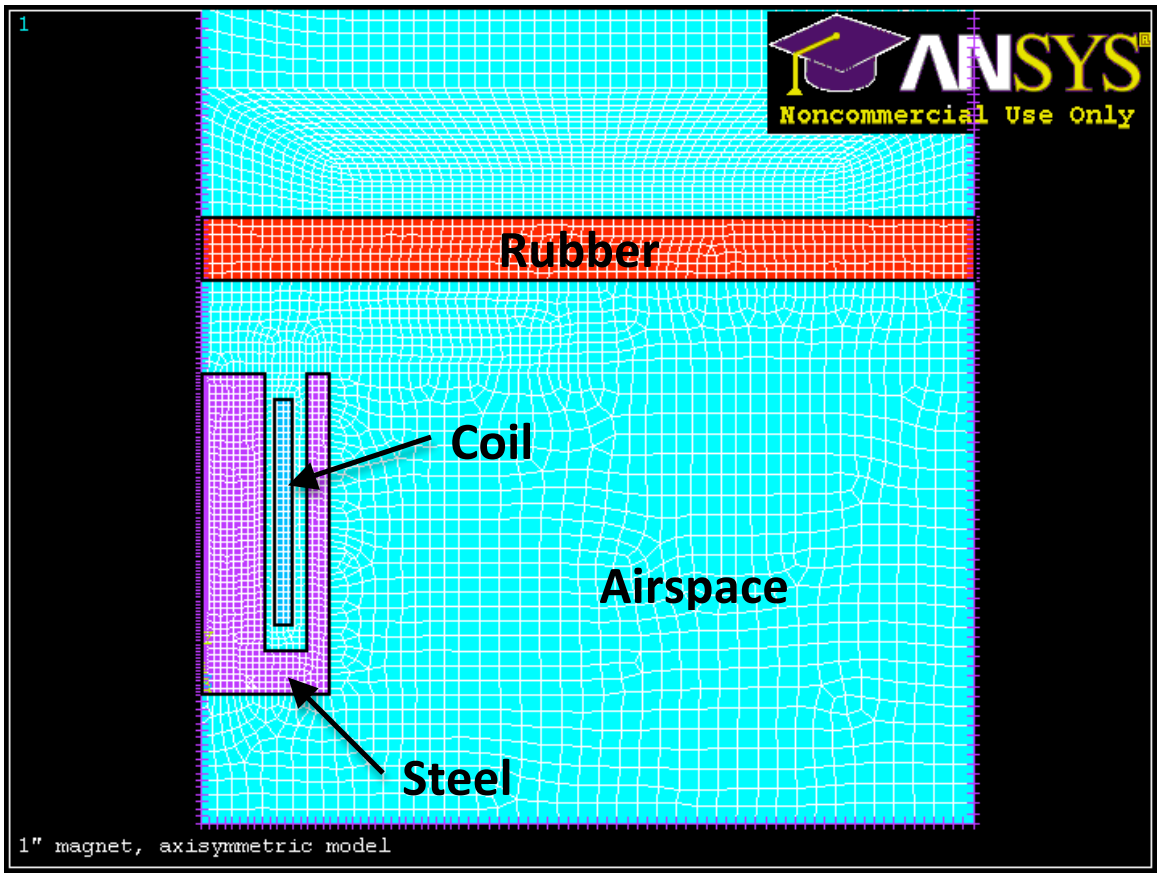

Figure 4.10 ANSYS model of 1” electromagnet

No air elements are included past the right-hand edge of the rubber component. Its edge is far enough away from the electromagnet that very little force is acting on it, so surrounding air elements at the edge are not necessary. The element mesh size in Figure 4.10 is the same as that in Figure 4.9; the elements in the rubber and electromagnet

component are 2mm square and transition to 4mm square in the surrounding airspace regions.

After application of the boundary conditions and loads, the model is solved using the MAGSOLV command in ANSYS. The command ramps the applied load over a number of steps until the solution converges, which is an especially valuable technique for convergence of non-linear solutions. ANSYS post-processor commands allow for inspection of the axial and radial components of the *B* and *H*-fields in the solution. Nodal forces also are calculated at nodes that lie along boundaries of materials with unlike magnetic properties. The FMAGSUM macro is used, which identifies the magnetic rubber as a component and calculated the total magnetic force applied to it by the magnetic field. The macro outputs the force calculated by a virtual work method and a Maxwell stress tensor method. These force outputs are used for comparison with experimental results.

4.3.3 Mesh Development and Convergence

A mesh convergence method was applied to the field model to determine the mesh size that optimally balances solution accuracy and computation time. The density of the element mesh was varied as well as the order of the elements. PLANE13 linear elements were used which contain four nodes, one node at each corner. The eight-node PLANE53 quadratic element also was used, which contains a node at each corner and at the midpoint of each side. An element size, *E*, was chosen for the elements that make up the electromagnet, the rubber, and the space between them. The value *E* corresponds to the side length of a nominally square element. The surrounding air space contains a

transition zone adjacent to the electromagnet and rubber with element size 1.5E. The outer zone of the air space has element size 2E.

A field model simulating the 6" electromagnet was built with the following experimental parameters: t = 10mm, g = 7mm, ϕ = 30%, I = 3A and 13.6A. The value t refers to the rubber thickness, g to the air gap between the rubber and the electromagnet, ϕ to nominal rubber loading fraction measured BH curve, and I to the coil excitation current. The two I values serve to indicate any difference in convergence between models with lower and higher applied currents. This check is important because high-current situations tend to require more iterations for convergence. The model was constructed with E ranging from 5mm to 0.8mm. The FMAGSUM macro was called and the values for the total force using virtual work and the Maxwell stress tensor were recorded. As computation time is directly related to the total number of elements, the force values are plotted against the nominal number of elements in the rubber component. This element number value is found by dividing the area of the component by E^2. For E = 5mm and E = 0.8mm the nominal number of elements are approximately 30 and 1200, respectively.

Figures 4.11 and 4.12 show the total force values calculated by ANSYS for the low and high current situations, respectively. Both scenarios show similar convergence trends. The low current scenario converges to a force value of 28.53N and the high current scenario to 454.61N. Note, however, that the experimental force values are 45.4N and 478.9N, respectively. Comparison with the experiment shows that the model's force value predictions are realistic. The error in the prediction is discussed in Chapter 5. In both cases the PLANE13 linear elements using the Maxwell stress tensor calculation converge much more slowly than the other three methods. It may be the case that the

linear interpolation within the PLANE13 elements is incompatible with the Maxwell stress tensor formulation due to rounding or interpolation error. Regardless, it is concluded that the linear Maxwell formulation is not reliable.

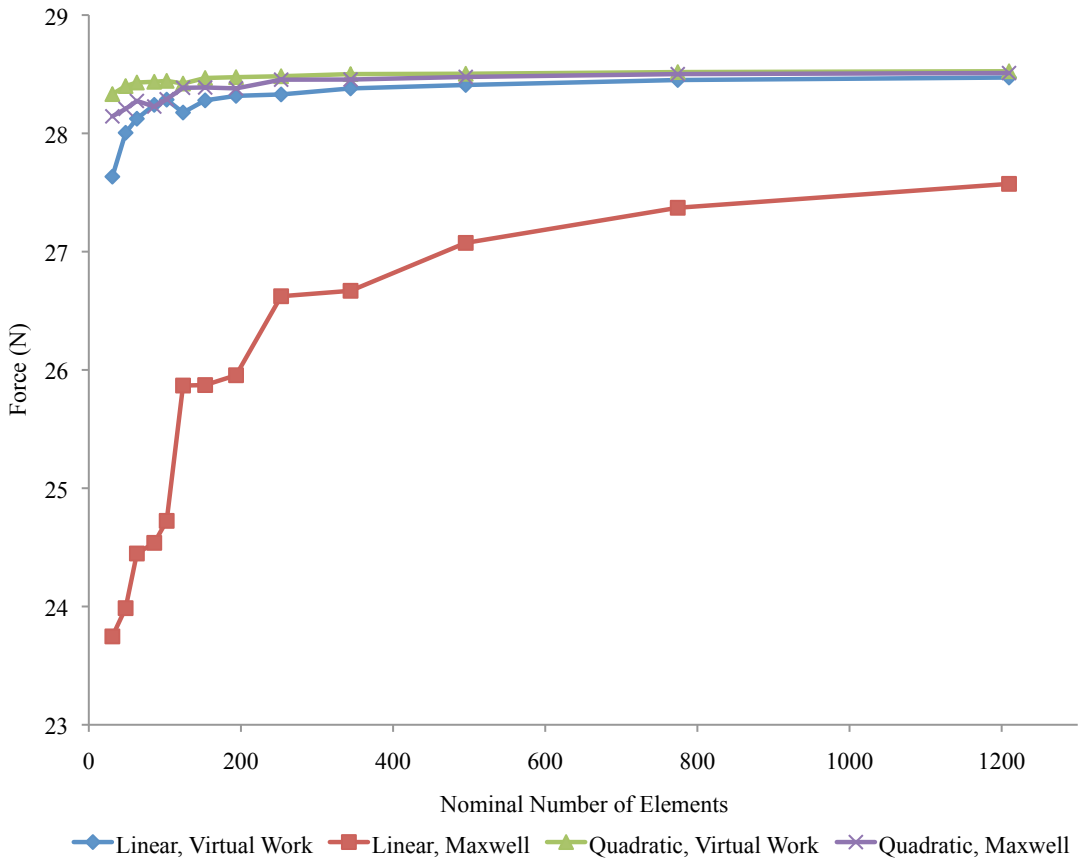

Figure 4.11 Mesh convergence data for low current (I = 3A)

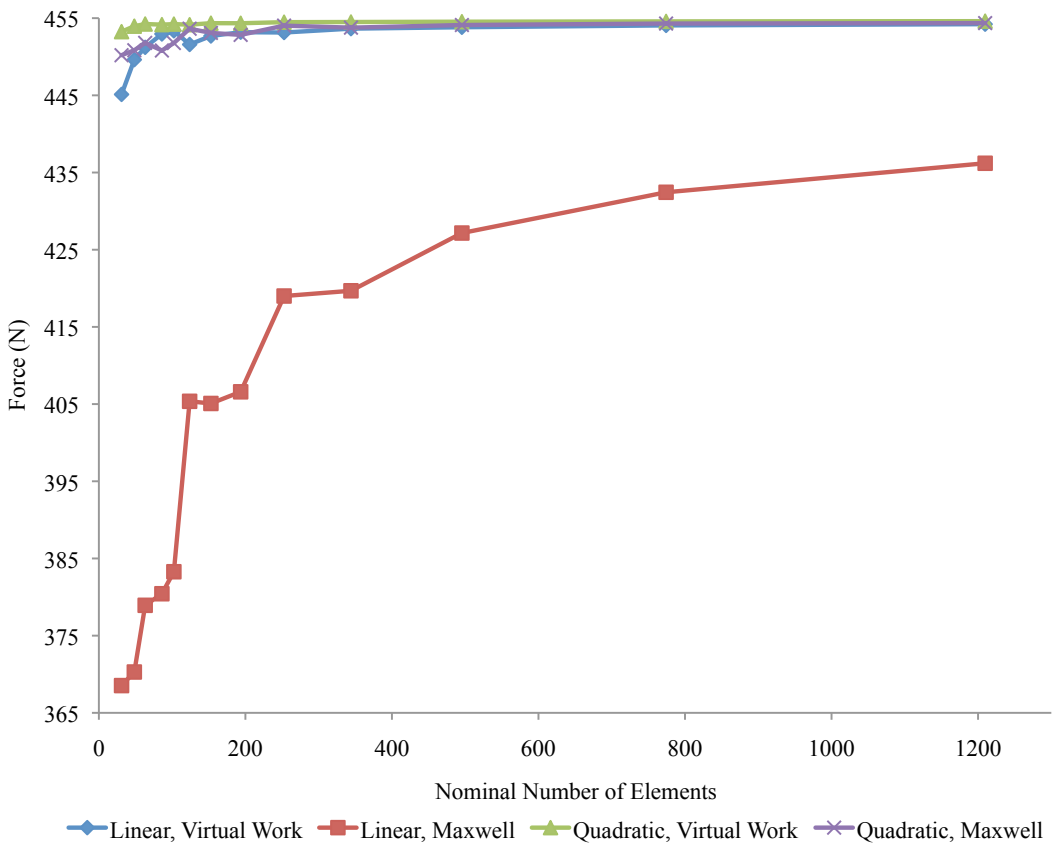

Figure 4.12 Mesh convergence data for high current (I = 13.6A)

Figure 4.13 shows the percent error of the three valid formulations at low and high currents. The low current curves are shown dashed and the high current curves are solid. The force values of the PLANE53 virtual work calculation at the densest mesh are used as the references for the percent error calculation. As such, both of the quadratic virtual work curves necessarily show zero percent error at maximum mesh density.

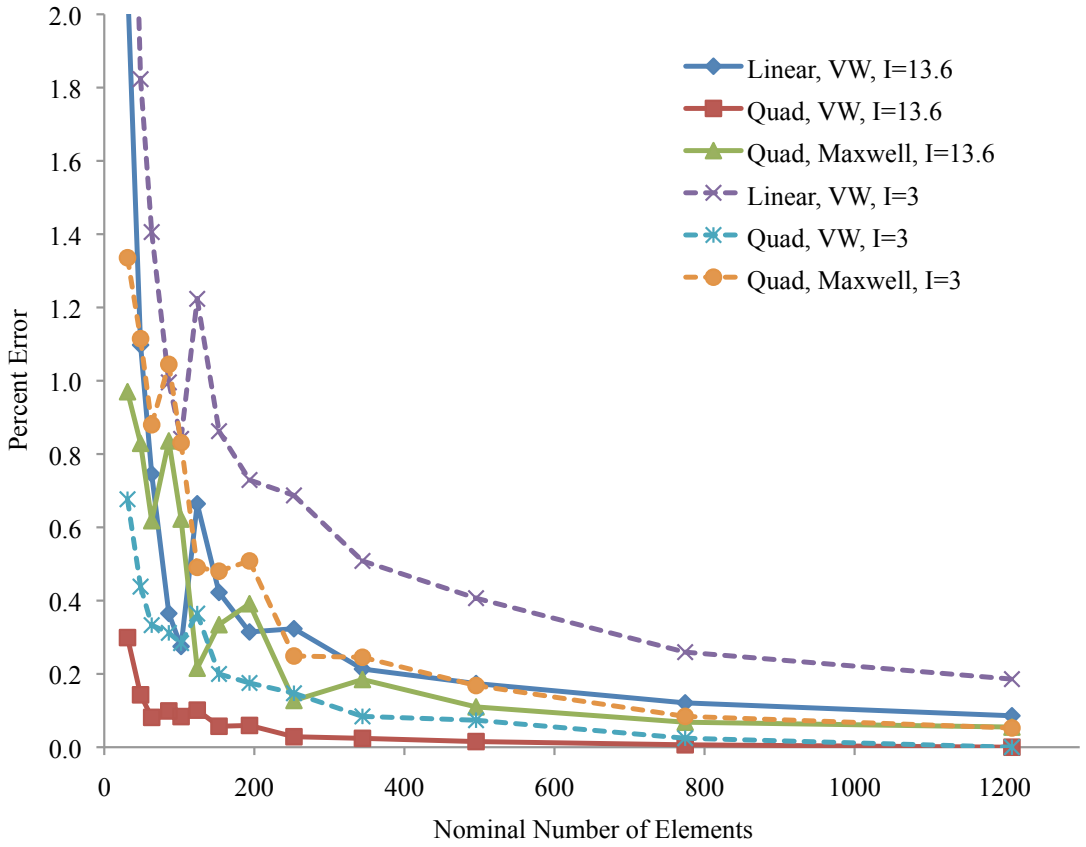

Figure 4.13 Mesh convergence data showing percent error

All six curves show some degree of oscillation at low element numbers. However, the quadratic virtual work curves settle the quickest and cease oscillation above the 194 element number point. This point corresponds to an element size of E = 2mm. At this point the low current curve displays 0.18% error and the high current curve has 0.06% error. The convergence speed and accuracy are superior for both the low and high current scenarios. Therefore, the E = 2mm using a PLANE53 quadratic element and virtual work formulation is used for the 6" electromagnet models.

Mesh convergence data were also collected for the 1" electromagnet model. A model was created with the same parameters as for the 6" convergence (t = 10mm, g = 7mm, ϕ = 30%) except an applied current of I = 0.5A was used. Only PLANE53

quadratic elements with the virtual work calculation were used to determine the total force on the rubber. The rubber component element size *E* was varied from 2.5mm to 0.7mm. The maximum size of 2.5mm was chosen to eliminate high aspect ratio elements due to the potting thickness feature of 0.5mm. The mesh of the magnet component is 0.667*E* in order to capture its small features. Transition zones and the outer airspace element sizes are 1.5*E* and 2*E*, respectively.

Figure 4.14 displays the mesh convergence data of the 1" electromagnet ANSYS model. The experimental value for this force is 0.239N. The element number corresponds to the nominal number of elements in the rubber component as described earlier.

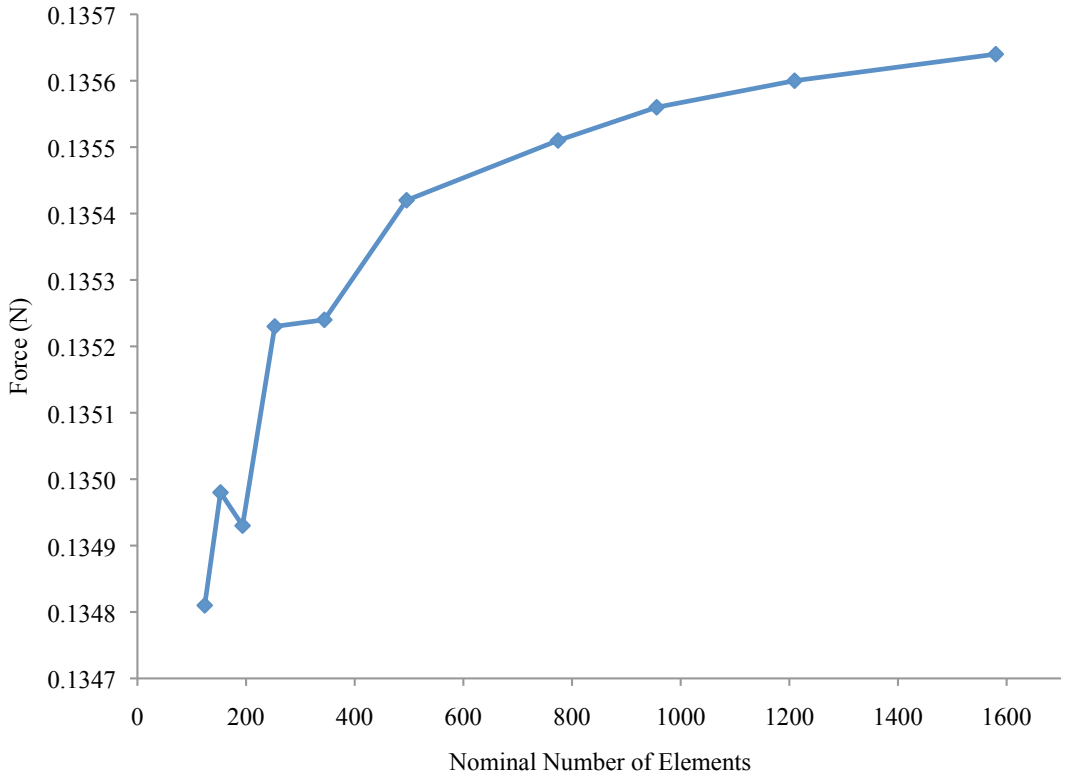

Figure 4.14 Mesh convergence for 1" electromagnet model

The force values oscillate until a value of about 400. At an element number of 800 the force value is only 0.1% less than the value with the maximum mesh value of

0.13564N. This point, corresponding to an element size of E = 1mm, is chosen for the optimum mesh size of the 1” electromagnet model.

4.4 Experimental Procedure

The previous sections explain the apparatus and materials used to characterize the forces developed in the magnetic rubber by applied fields. The purpose of this section is to outline the methods of the various experiments performed to quantify the magnitude and distribution of the forces. The FEA field model was solved at similar parameters for comparison with experimental results in order to gauge the model’s trustworthiness in both interpolation and extrapolation of the field problems. The results of the experiments, accompanied by discussion, follow in chapter 5.

4.4.1 Force Experiments

Five sets of experiments were performed with the electromagnets and load frame to measure the total attractive force generated within the magnetic rubber samples. In all cases the samples were 158mm discs with varying thicknesses. One 6” electromagnet and four 1” electromagnets were used in the experiments. In all cases the electromagnet was bolted to the cold plate, which was clamped to the base of the Instron frame. The sample was placed in the non-magnetic hanger suspended from the load cell. In order to calibrate the air gap distance, the Instron controls were used to drive the hanger down until the bottom of the plate contacted the face of the electromagnet. The distance readout on the Instron interface was zeroed and the hanger was driven to the appropriate gap distance accounting for the thickness of the hanger plate. After mounting and positioning, the load readout of the Instron was zeroed as well. Cooling water flowed through the cold plate to regulate the electromagnet temperature. In the case of the large 6” electromagnet the

clamp-on ammeter was zeroed and installed. The power supply was turned on and the voltage of the variac was adjusted until the required current was driven through the electromagnet. The resulting force was recorded manually after the readout of the Instron stabilized. At high applied currents, above approximately 0.5A and 7A for the small and large electromagnets, respectively, the current was not stable and tended to decrease with time due to Joule heating of the coils. In these cases the current source was turned on, allowed to stabilize, and immediately turned off at which point the reading was taken. At very high applied currents the electromagnet required up to one minute to cool between readings.

The first experiment set involved 4mm thick samples with different magnetic fillers: nickel, permalloy, and coarse iron filings. As discussed in section 4.2.2, the samples were loaded with 25%, 50%, and 75% filler by weight for each material except for permalloy, which was only fabricated at 25%. Attractive forces were measured with the 6" electromagnet at applied currents of up to 4.2A. Each sample was suspended at a distance of 8.4mm from the face of the magnet and the force measured by the Instron was recorded. The results of this experiment, detailed in the next section, demonstrated that iron is the best material for generating high attractive magnetic forces.

The second and third sets of experiments involved the five rubber samples filled with high-purity iron powder, which are detailed in Table 4.3. The high-purity iron is more magnetically responsive than the coarse iron filings that contain dirt and oxides. Single 6" and 1" electromagnets were used to generate the magnetic field in the second and third set, respectively. Four parameters were varied: the iron volume fraction of the rubber (ϕ), the thickness of the rubber sample (t), the air gap between the sample and the

electromagnet (g), and the current applied to the electromagnet (I). Table 4.6 displays the values of the experimental parameters used in the iron-filled rubber force tests with the small and large electromagnets.

Table 4.6 Experimental parameters for iron-filled rubber force tests

Variable	ϕ	t	g	I
# of Values	3	2	4	10 - 39
Range	15, 23, 30	6.4 - 10.7	7 - 25	0 - 19.2
Units	[%]	[mm]	[mm]	[A]

Three nominal values are used for the filler volume fraction. Two thicknesses are used, nominally 6.5mm and 10mm, although the actual values vary slightly. Four values for g are used that simulate a realistic thickness range of composite laminate parts. A minimum value of 7mm was chosen because the aluminum plate used to suspend the sample is 6.5mm thick. Some data for the small electromagnet with large air gaps (25mm) were not recorded because the forces were too small to register on the Instron with any accuracy. Forces were recorded at current values up to 0.5A in 0.1A increments and from 0.5A to 1.8A in 0.25A increments for the small electromagnet. Data points were collected up to 6.6A in 0.3A increments and from 6.6A to 19.2A in 1.4A increments for the large electromagnet. Additional points were collected for the experiment involving sample 1 and the large electromagnet between 6.6A and 9.4A at 0.3A increments. Due to load cell limitations, current values causing a force greater than 500N were not recorded. For example, the experiment with sample 1 and the 6” electromagnet at a 7mm air gap includes applied currents only up to 13.6A. The data are used to evaluate the effects of the parameters on the total attractive force. The FEA model is solved with similar parameters in order to verify it against the experimental forces.

The fourth set of force data involves 158mm diameter low carbon steel plates in place of rubber samples. Low carbon steel is primarily iron and is used here to show a theoretical maximum possible attractive force. A steel plate represents the ideal of a magnetic rubber that is filled to a 100% iron volume fraction. The experiment serves to demonstrate the difference in magnetic response between the iron-filled rubber and steel. Seven plate thicknesses in total were used. Five thicknesses were chosen to represent the same mass of iron in the five high-purity iron filled rubber samples. Their thicknesses are equal to $\phi \cdot t$ of the samples: 0.94mm, 1.52mm, 1.91mm, 2.34mm, and 3.05mm. These serve to compare the response of a fixed mass of iron in a bulk unit and dispersed through a larger volume. The five samples were composed of shim stock of different thicknesses to the appropriate total thickness. The other two steel samples are 6.4mm and 10.2mm thick which approximately matches the thin and thick rubber samples, respectively. Experimental current and gap parameters were chosen similar to those used in the force experiments involving the high-purity iron filler rubber samples. The steel samples yielded high attractive forces, which, in some cases exceeded 500N. When the 500N limit was reached the applied current was not increased due to the capacity of the load cell.

The final experiment set involves arrays of 1" electromagnets. The purpose of the experiment was to observe the effect of square and hexagonal array configurations on the total generated magnetic force. Only rubber sample number 1 (thick with 30% loading) was used for the experiment. The electromagnets were mounted in arrays on the aluminum intermediate plate as shown in Figure 4.6 with various spacing values. The array spacing value refers to the distance between the centers of two adjacent electromagnets. Four electromagnets were mounted in a square configuration at four

spacing values: 25.4mm, 26.9mm, 35.9mm, and 53.9mm. The hexagonal configuration involved three electromagnets with spacings of: 25.4mm, 33.0mm, 44.0mm, and 66.0mm. The smallest spacing used in both cases corresponds to the minimum possible spacing due to the 1" diameter of the electromagnets. The attractive force was measured with both array configurations at gap values of 7mm and 9mm with six applied currents ranging from 0.1A to 0.75A. The electromagnets were wired in parallel and driven by the DC power supply. Before wiring, the magnets were each placed face-to-face and energized to confirm that they all generate magnetic fields of the same polarity. In other words, the cores of each electromagnet when energized act either as North or South poles and not a combination of both.

4.4.2 Model Validation Experiments

As discussed in section 4.3, axisymmetric FEA models were constructed in ANSYS to simulate both the 6" and 1" electromagnets and their magnetic interaction with the high-purity iron filled rubber samples. The models use the exact geometry of the electromagnets, the magnetization model of low-carbon steel, and the number of coil windings as previously determined to simulate the electromagnets. The magnetization models of the rubber as measured with the VSM are also applied in the model.

The purpose of the FEA model is twofold: to allow for study of the flux paths and nonlinear magnetic phenomena and to provide a reasonable extrapolation of the system with higher applied currents and variation of other parameters. In addition, the model may be expanded to perform magneto-structural coupled analysis using structural material models. Validation of the model is necessary in order to use it for any of these purposes. The model was run at the same parameters shown in Table 4.6. The total force,

calculated by the virtual work FMAGSUM macro, was compared with the experimental results. Only a selection of approximately 8 of the experimental current values was used, however, to save processing time. The model validation was performed for both the 6" and 1" single electromagnets. Additionally, the model was run to simulate the force experiments performed with the steel plates. The main modeling difference in this case is that the BH curve of low carbon steel was employed in place of the experimental BH data of the magnetic rubber.

Additional model validation was performed by comparing the axial B-field profile near the face of the electromagnet along the radius to the profile solved for by the model. It is worth noting that, while comparison of the field profiles serves to validate the model in general, it also provides more specific validation of the B-field at the face of the rubber component as reported by the model. As discussed in Chapter 3, knowledge of the normal B-field on a magnetizable component allows the magnetic surface pressures to be calculated. The B-field was measured with the transverse probe Gaussmeter. The probe was fixed to a wooden stick in order to provide consistent positioning. The rotational position of the probe was manually adjusted to provide a maximum reading to ensure perpendicularity of the probe to the prevailing magnetic field. An inch-scale ruler was fixed to the face of the 6" diameter electromagnet as a reference. The probe and stick were moved relative to the ruler and readings were taken along the radial position at 15 or 25 locations. Figure 4.15 shows the apparatus used to take the field readings. Due to the thickness of the wooden stick and the half-thickness of the probe, the Hall-effect sensor was positioned 2.35mm from the face of the electromagnet. The procedure was performed with various process parameters outlined in Table 4.7.

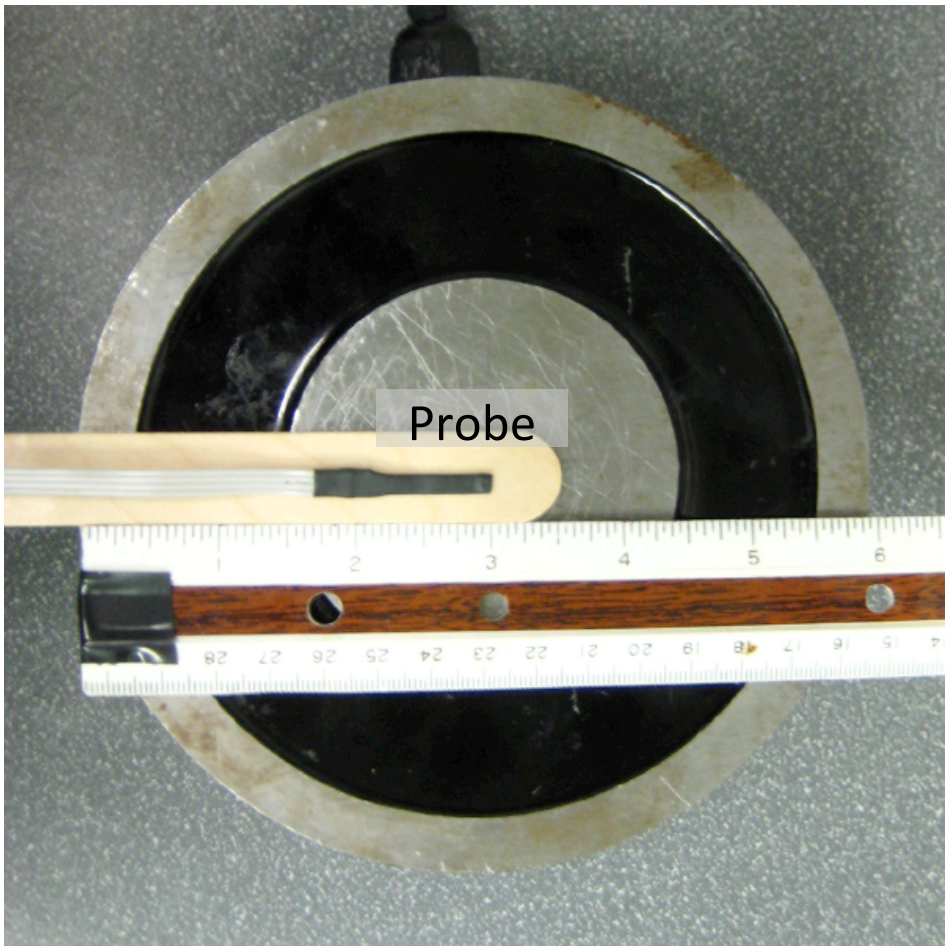

Figure 4.15 Experimental apparatus for measuring the axial B-field of the 6" electromagnet

Table 4.7 shows the parameters used in the B-field profile experiments. In the first experiment no rubber sample was used. Readings were taken at 25 locations for the low-current situations while 15 were taken for the I = 15A situation.

Table 4.7 Experimental parameters for radial position B-field Gaussmeter procedure

Sample	*g* [mm]	*I* [A]
None	N/A	1.5, 3, 4.5, 6, 15
#1 (thick, 30%)	10, 15, 20	1.5, 3, 4.5, 6, 15
#4 (thick, 15%)	20	1.5, 6, 15

The 30% loaded sample was suspended at three air gap values, *g*, and readings were taken at the four lower current values. The 15A data were only taken at the 20mm gap.

Only a 20mm gap and three current values were used as the parameters for the thick, 15% loaded sample. Note that a minimum air gap value of 10mm was chosen to facilitate the accurate positioning of the Gaussmeter probe.

The FEA field model was solved at each of the parameter combinations listed in Table 4.7. The PATH command in ANSYS was employed to list the B-field values in the y-direction along a radial path from the center of the electromagnet to its edge. The radial path was offset from the face of the modeled electromagnet by 2.35mm to accurately simulate the position of the sensor. Note that the y-direction in the model is parallel with the axis of symmetry and hence refers to the axial B-field. The model solution is compared with the experimental values and the results are discussed in Chapter 5.

In order to determine the clamping pressures realizable by a magnetic clamping device utilizing iron-filled rubber components, force data were taken at a variety of process parameters. Electromagnets of different sizes were used to determine scalability of the force and the possibility of using arrays of electromagnets. The numerical FEA model was solved at many of the same process parameters used in the force experiments in order to provide a comparison and validation of the model. Field data also were collected with the Gaussmeter and compared with the results of the model in order to determine how well the model simulates the magnetic flux paths involved in the system.

4.5 Chapter Summary

This chapter provided the details of the experiments performed to characterize the pressure developed by a magnetic clamping device involving DC electromagnets and composite magnetic rubber. The apparatus utilized in the experimentation were discussed including electromagnets, supporting devices, and an Instron load frame. The

electromagnets were investigated in order to determine details about their construction necessary for simulation. Details of the fabrication and constituent materials of magnetic rubber samples are included. The magnetization curves of high-purity iron filled silicone rubber samples of three loading percentages were measured using a vibrating sample magnetometer. An FEA model in ANSYS was developed to study the magnetic field details involved in the clamping device. This section discusses the details of the model and a mesh convergence procedure. Force experiments and B-field measurements involving the magnetic rubber samples and are outlined for comparison with the results of the model in chapter 5. Additional force experiments involving steel plates and experiments using arrays of small electromagnets are outlined in this chapter.

CHAPTER 5

RESULTS AND DISCUSSION

This chapter presents the results of the experiments performed to characterize the attractive forces developed by the magnetic clamping device. The effects of the experimental parameters are analyzed. The force data are compared with the results of the FEA model simulation in order to validate the model for use in the design of the clamping system. Error analysis and a first-order sensitivity study are performed. In addition, B-field data gathered with a Gaussmeter are compared with the model in order to validate the internal magnetic field state of the system as reported by the model. The possibility of expanding the model to include coupled magneto-structural effects is discussed. The device is analyzed from a magnetic flux standpoint to determine the scalability of the system and the critical design proportions. The model is used to optimize these proportions and a design method for the device is developed that is based upon these proportions. The use of electromagnet arrays is discussed and experimental array data are presented and analyzed. The use of steel in place of the rubber armature also is discussed. An example device is designed and power requirements are discussed. Finally, the model is used to simulate the effect of utilizing high-permeability armatures in order to predict the performance of the device with advanced materials as a theoretical upper limit.

The magnitude of pressure the clamping system is able to develop, the required power to operate it, and the ability of the system to effectively distribute the pressure over the face of a part are of primary interest in the development of a magnetic clamping device for consolidation of composite laminates. The device consists of an electromagnet

and a magnetizable armature, which together create compressive stress on a part placed between them. “Armature” is defined here as the component that is attracted to the electromagnets, which generates the exciting magnetic field. The armature is a magnetizable and mechanically flexible sheet of rubber that is filled with magnetic particles. The critical design parameters include electromagnet construction, applied electric current, armature intrinsic magnetic behavior and geometry, and the gap between the electromagnet and armature. Experiments were performed, as described in chapter 4, to observe the effects of these parameters on the consolidation pressure characteristics. FEA modeling of the device is compared with experimental data and used to gain further insight into the magnetic field phenomena involved in the system. The model also is used to predict the response of the device to higher applied powers and different geometric configurations. Characteristic proportions of the device also are discussed and developed as a method by which the clamping device may be designed based on processing requirements. Magnetic phenomena such as flux leakage and saturation are discussed as they pertain to the proper design of the clamping device. Experiments also were performed to investigate the possibility of employing arrays of electromagnets. Additional force data were measured using steel plates as the armature in order to provide a comparison with magnetic rubber. The results of these experiments are presented and analyzed in this section.

5.1 Magnetic Filler Material

A preliminary investigation was performed to determine the optimum magnetic filler material for use in the magnetic composite rubber. Only the material of the filler

was considered in the investigation; the effects of particle size, aspect ratio, and orientation on the rubber's magnetic properties were not investigated.

Figures 5.1 and 5.2 display the results of the attractive forces of the 4mm thick samples loaded with nickel, permalloy, and coarse iron filings with the large, 6" diameter electromagnet. The 25% by weight samples and the higher-loading samples are displayed on separate graphs for clarity. Figure 5.1 demonstrates that, at low applied currents, permalloy is a superior filler material. However, at an applied current of 4A, the iron surpasses the permalloy. Over the 1A to 4A range, the force curve of the permalloy sample is highly linear; in fact, a linear regression fitted through the three data points indicates an R^2 value greater than 0.999. However, the curves of both the iron and nickel appear to be quadratic in nature. This phenomenon may be explained by the magnetization curves of the three materials. Permalloy is designed as a magnetic alloy to exhibit extremely high initial permeability but to saturate at low B-fields, roughly 1.1 Teslas. Nickel and iron have initial permeabilities similar to each other but which are much lower than permalloy. Nickel saturates at about 0.6 Tesla, while low-purity iron (such as steel) saturates at about 2 Teslas (ASM, 1978). Hence, at low fields the iron and nickel samples display quadratic trends as they slowly approach saturation, whereas permalloy is already nearly saturated at the applied fields utilized in the experiment. The low B-field saturation of nickel also explains why it provides the least force of the three materials.

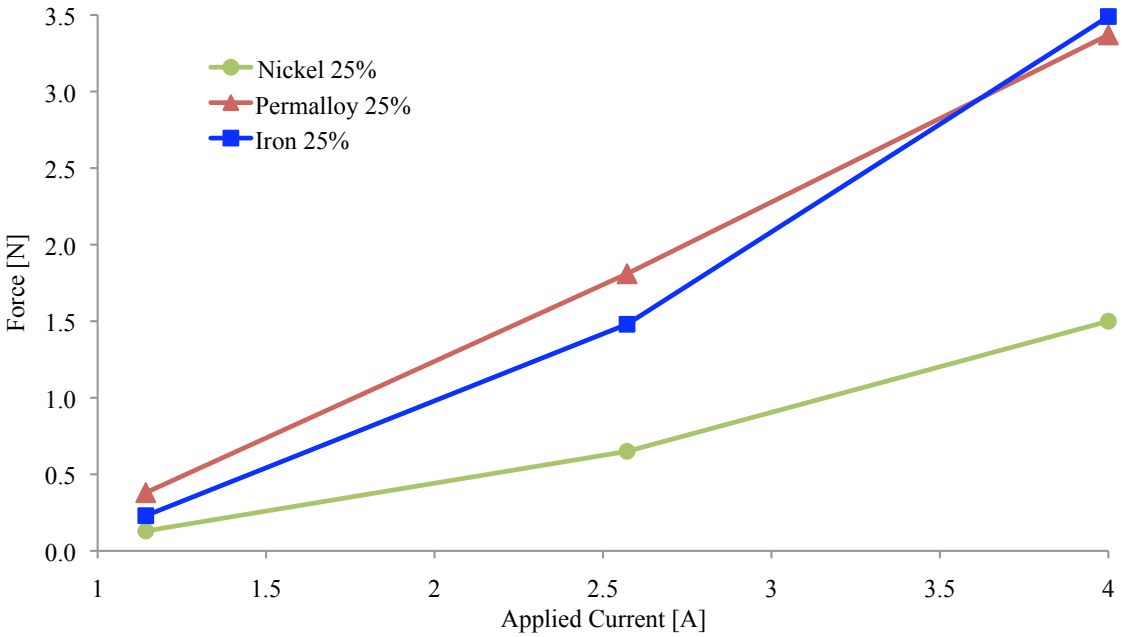

Figure 5.1 Force data for nickel, permalloy, and coarse iron samples at 25% loading by weight

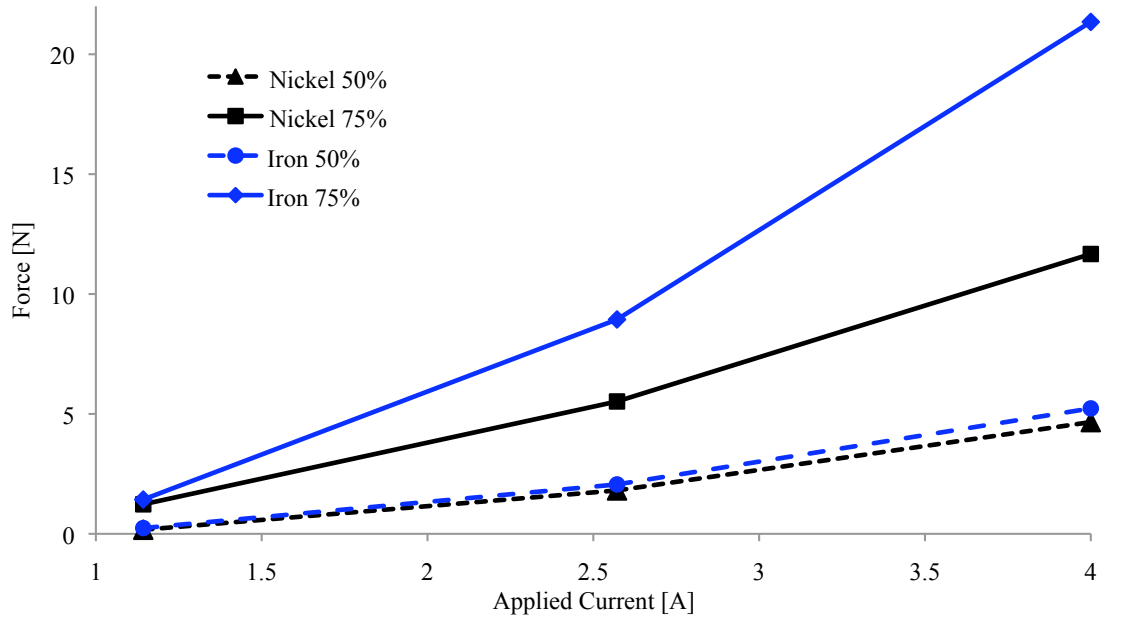

Figure 5.2 Force data for nickel and coarse iron samples at 50% and 75% loading by weight

Figure 5.2 shows the 75% (by weight) loaded sample curves with solid lines and the 50% loaded sample curves with dashed lines. Initial inspection of Figure 5.2 indicates that loading percentage is a very important factor. Comparing the 75% samples to the

25% samples shows an increase by a factor of 8 with nickel and a factor of 6 with iron. The 50% loaded iron and nickel samples show nearly the same performance, which is interesting because the 25% and 75% iron samples clearly surpass the nickel samples. The 75% iron curve shows a divergent trend from the 75% nickel curve indicating that higher applied currents will show even greater separation between the two. Therefore, it is concluded that the iron filings are the superior filler material for the magnetic rubber armature due to the higher observes forces. Furthermore, the saturation B-field of the material is shown to be a strong indicator of the magnetic force the material is capable of producing. As such, high-purity iron powder, which has a higher saturation point than low-purity iron, is chosen as the ideal material for the magnetic rubber.

5.2 Force Experiments and Parameter Discussion

Chapter 4 describes in detail the methods of a number of experiments performed to characterize the forces developed between electromagnets and a high-purity iron filled magnetic rubber armature over a range of experimental parameters. This section presents the results of the force experiments performed with both the large and small single electromagnets. The trends observed are discussed and the effects of the process parameters are analyzed.

Figures 5.3 to 5.7 show the measurements of the attractive force between the large 6" diameter electromagnet and the five high-purity iron rubber samples. The four independent parameters of interest are the volumetric loading percentage of the sample, ϕ, the thickness of the sample, t, the air gap, g, and the applied current, I.

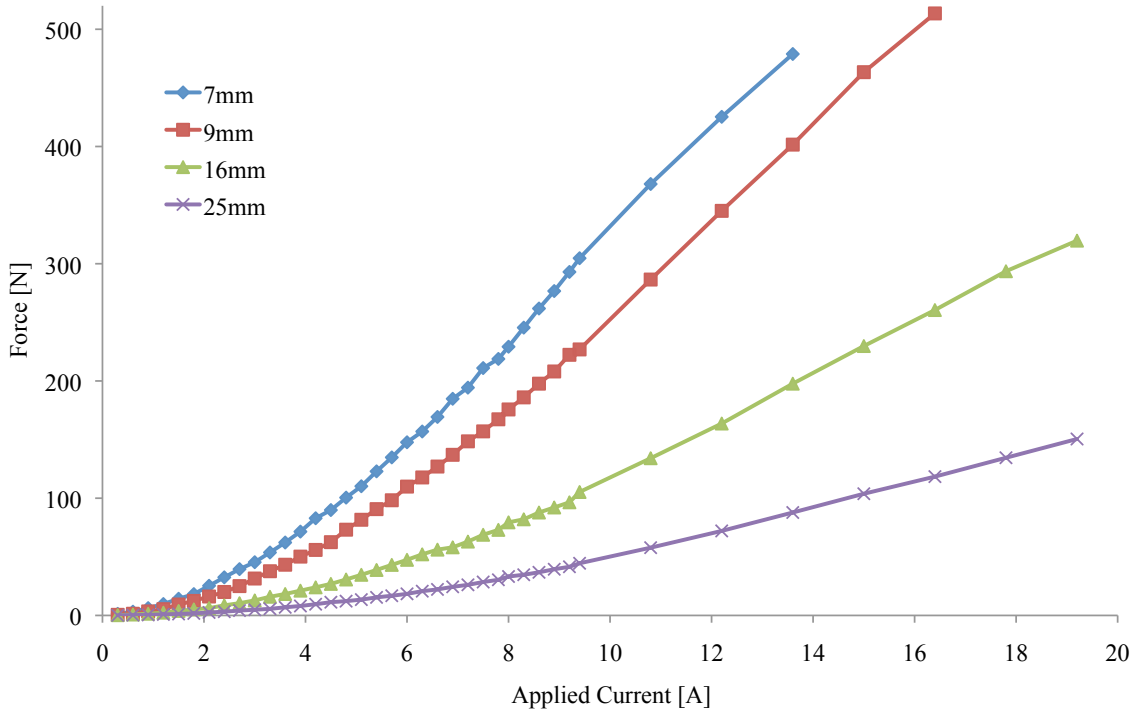

Figure 5.3 Force data of sample 1 (10.7mm, 30%) at four air gaps with 6" electromagnet

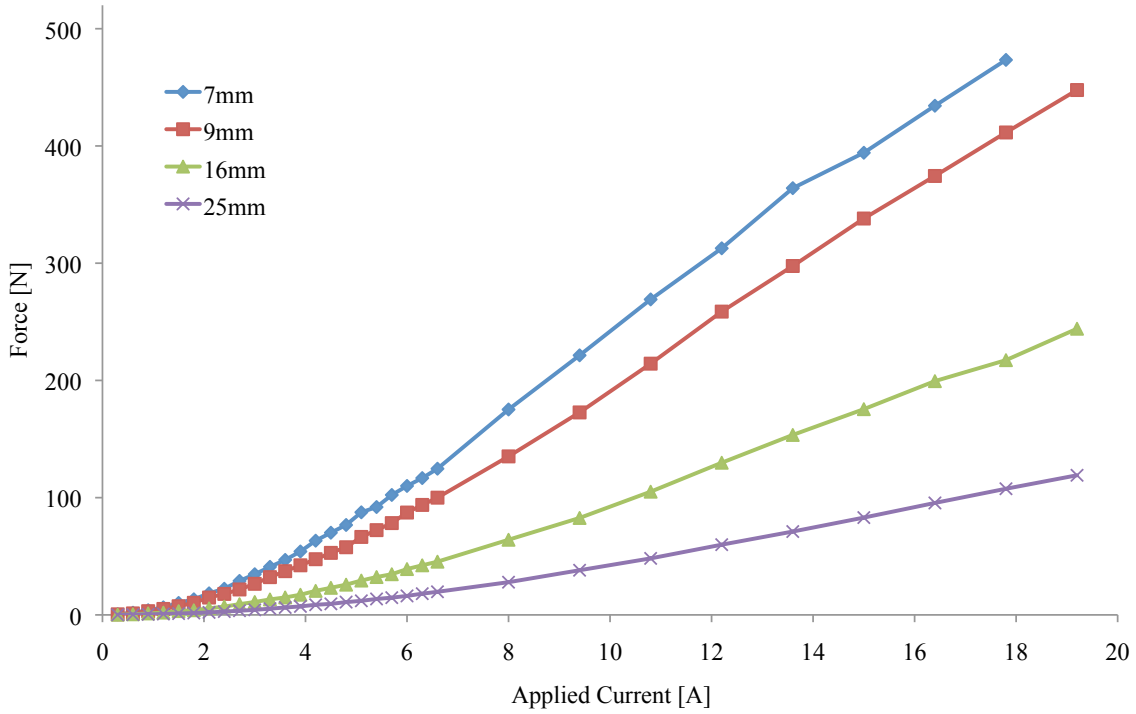

Figure 5.4 Force data of sample 2 (6.5mm, 30%) at four air gaps with 6" electromagnet

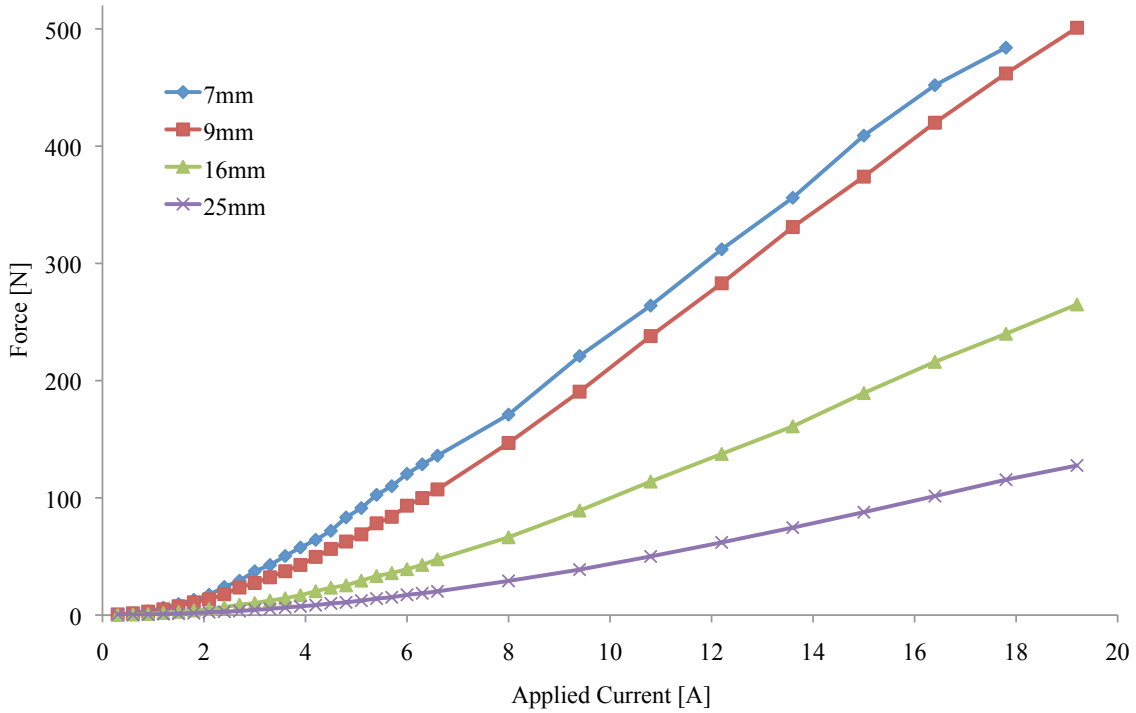

Figure 5.5 Force data of sample 3 (10.2mm, 23%) at four air gaps with 6" electromagnet

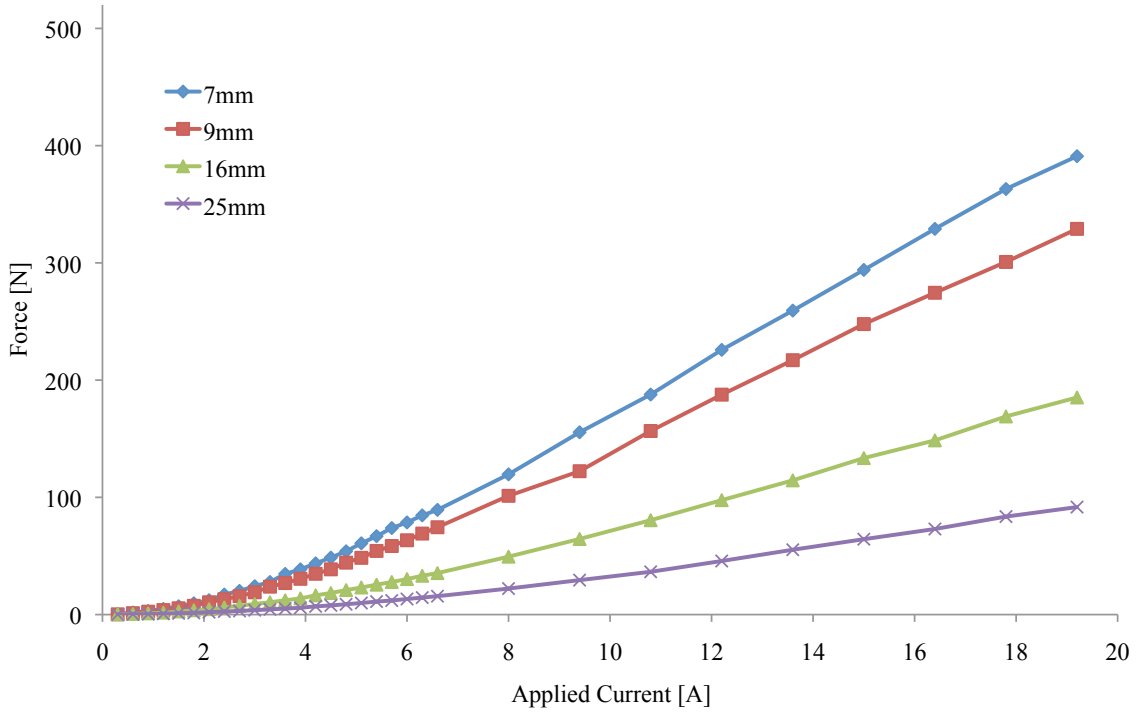

Figure 5.6 Force data of sample 4 (10.1mm, 15%) at four air gaps with 6" electromagnet

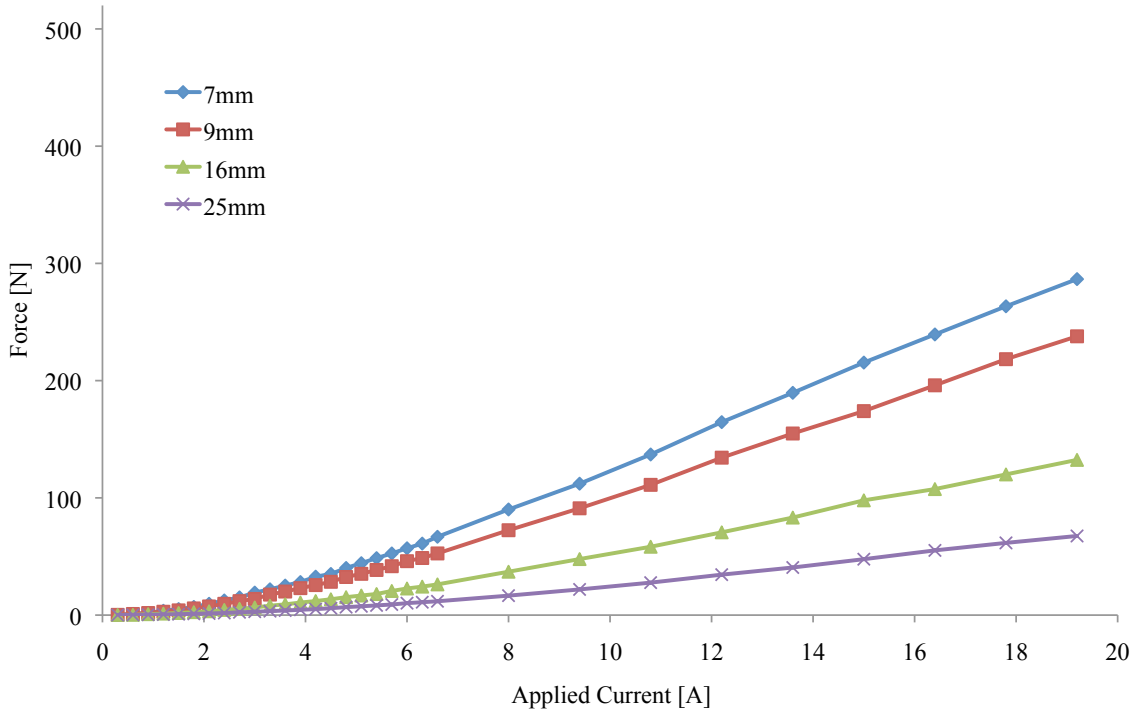

Figure 5.7 Force data of sample 5 (6.4mm, 15%) at four air gaps with 6" electromagnet

All 20 curves show similar trends with respect to current. The force increases quadratically and then levels out to a linear curve. The samples experiencing the highest forces, most notably the 7mm gap curve of sample 1 (Figure 5.3), show a distinct tendency of the slope of the force curve to decrease at high current values. The shift from the quadratic to the linear regime and the following shift to a lower-slope linear regime is due to the magnetic saturation of the electromagnet steel and of the magnetic rubber, respectively. This trend is visible in the sample 3, 7mm gap curve in Figure 5.5. The force as a function of I is quadratic up to 6A, very linear between 6A and 14A, and shows a distinct downward shift in the trend above 14A. Generally the curves with higher air gaps, such as 25mm, retain the quadratic trend up to larger current values than the curves with small air gaps. This phenomenon may be due to the decreased total magnetic flux developed in systems with proportionally large air gaps. For the same applied current, a

larger air gap presents a greater overall system magnetic reluctance (i.e., less magnetic coupling), which reduces the total flux developed. Therefore the electromagnet steel reaches saturation at higher applied currents. These phenomena are discussed later in greater depth.

The data demonstrate that in all cases and operating conditions the resulting magnetic force is increased with increasing applied current, rubber thickness and filler loading, and with decreasing air gap. A comparison of a selection of data points gives some indication of the effects of the independent variables on the force.

Figure 5.8 displays the isolated effect of ϕ on the measured force of the rubber samples at four selected operating conditions. The parameters I, g, and t are fixed for each curve and only the loading percent changes. In all cases, the force increases monotonically with increasing ϕ. The upper curve shows slight positive curvature while the lower curves show slight negative curvature indicating that the effect of ϕ on the force is somewhat dependent upon the other parameters.

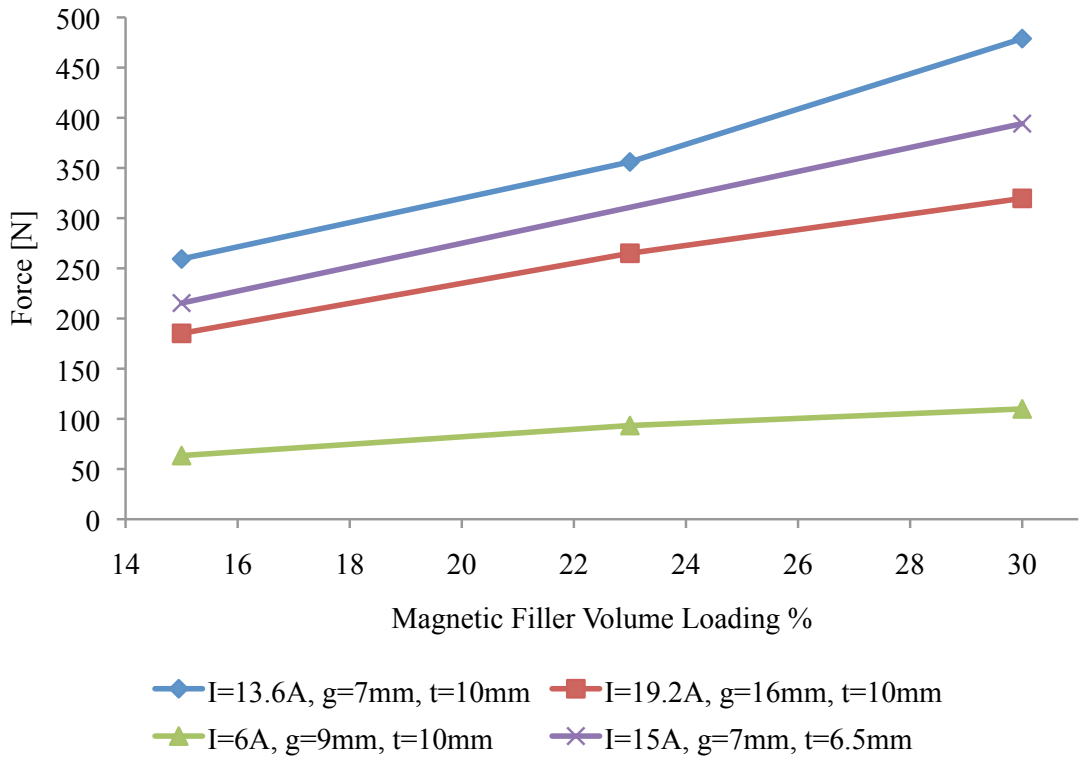

Figure 5.8 Effect of filler volume loading percent on observed force with 6" electromagnet

The thickness of the rubber sample also is an important factor in the force generated by the system. Referring to Equation 5.13, it is seen that the reluctance of an armature is directly related to its thickness. It is therefore expected that the thicker rubber samples should provide greater attractive forces than the thin samples.

Figure 5.9 shows a comparison of two force experiments over a range of current values: they vary only in the thickness of the sample. Rubber samples number 1 and 2 are used, which are the thick and thin $\phi = 30\%$ iron loaded samples. The two curves have similar trends but the force values for the thick (10.7mm) sample are approximately 30% greater than those of the thin (6.5mm) sample at each current value. A direct comparison of the force values between samples 1 and 2 and between samples 4 and 5 at all air gap values show that the thicker samples yield 20% to 40% greater forces over the range of applied current. The comparison serves to confirm that in all cases an increased armature

thickness increases the observed force. Further analysis is performed in section 5.5 with the FEA model to determine a detailed relationship between force and armature thickness.

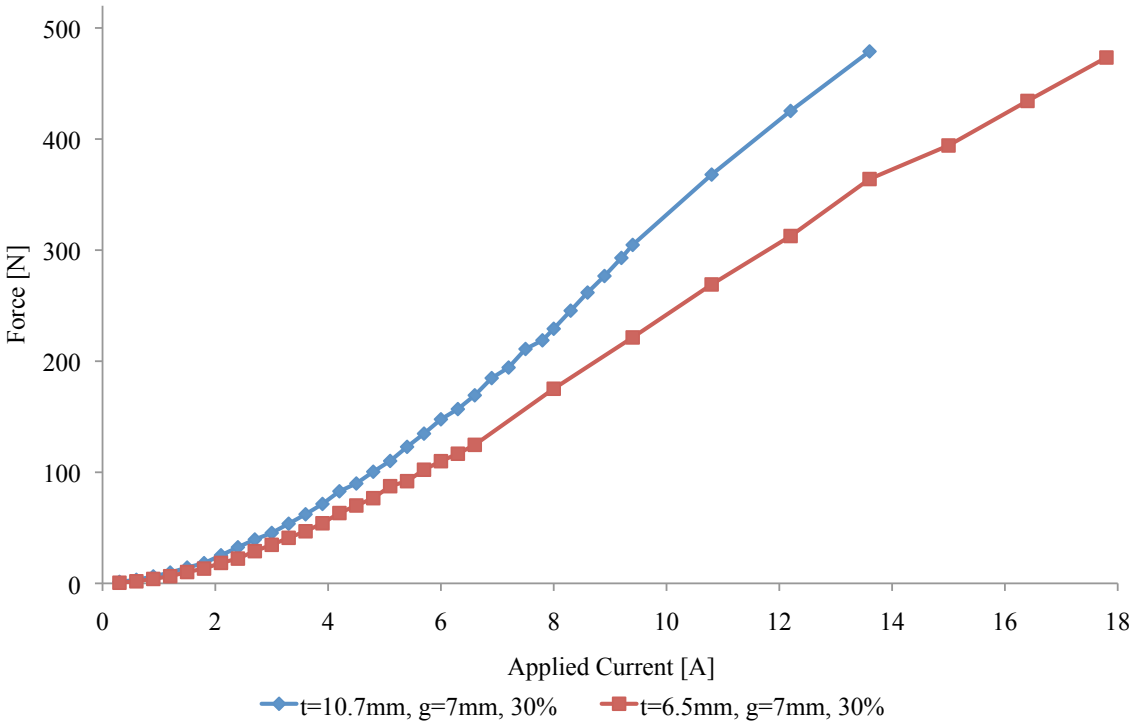

Figure 5.9 Force data of samples 1 and 2 at g = 7mm

Figures 5.3 to 5.7 each display force curves of a rubber sample at four air gap values. At all combinations of parameters, an increase in air gap always results in a decrease in observed force. As discussed previously, this phenomenon follows intuitively as an increase in the air gap increases the effective reluctance of the magnetic circuit. A set of current values from Figure 5.3 is displayed in Figure 5.10 with the air gap on the horizontal axis to visualize its effect on the force.

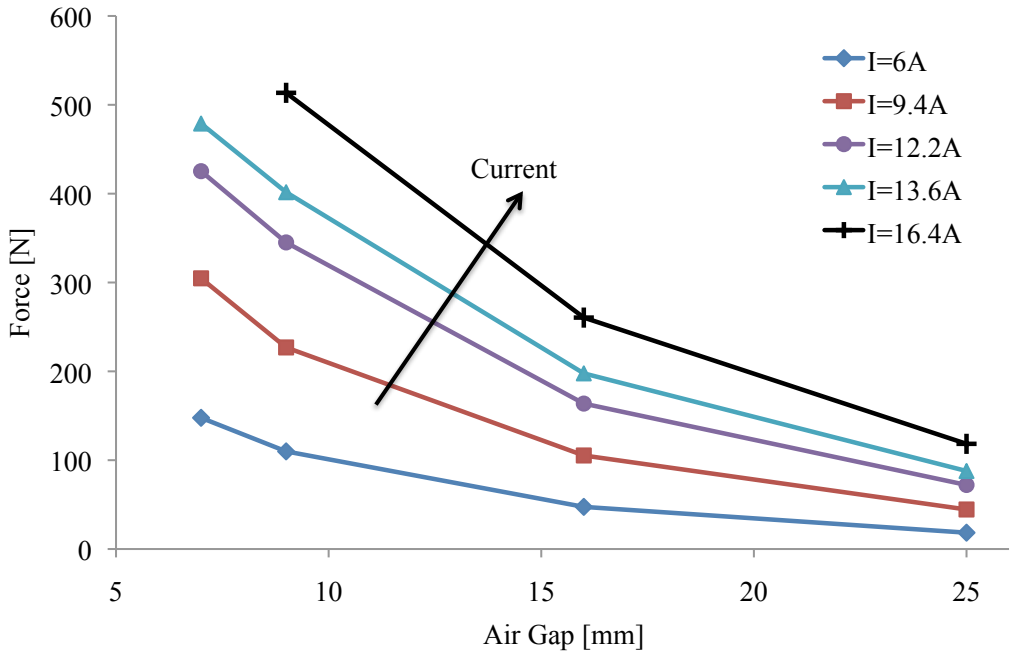

Figure 5.10 Effect of air gap on force at various currents for sample 1 data

Figure 5.10 highlights the effect of air gap on the observed force of sample 1 (t = 10.7mm, ϕ = 30%) at five values of applied current. In all five cases the curves very roughly follow the trend $F \propto g^{-2}$, which is well understood and documented in electromagnet design texts (Roters, 1941). The data indicate that the magnetic clamping device for consolidation of composite laminates may not be suited for thick parts, which act as the air gap in the system. The inverse squared relationship causes a substantial decrease in force for a small increase in part thickness. On the other hand, however, decreasing the part thickness does not result in a quadratic increase in force indefinitely. The attractive force between a flat-faced lifting electromagnet and an armature has a maximum value at zero air gap followed by a linear decrease to some point and finally an inverse squared decay. Figure 5.11 displays the divergence of the experimental values and the inverse squared trend for the I = 13.6A curve of Figure 5.10.

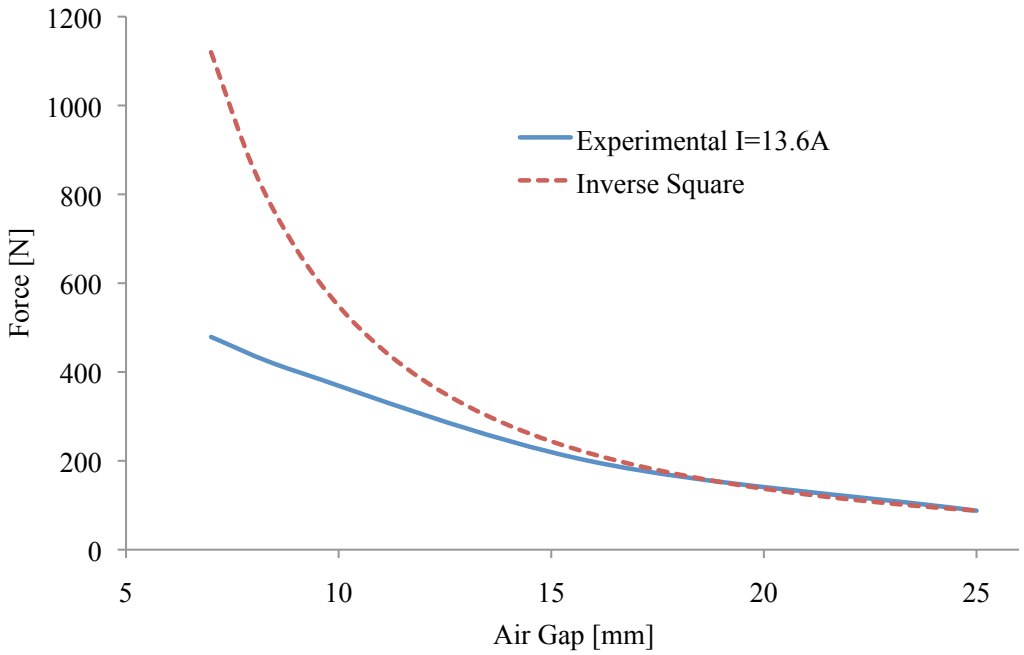

Figure 5.11 Experimental force vs. gap and inverse square theoretical curve

The experimental curve in Figure 5.11 is shown with a smooth fitting for clarity. As the inverse squared relationship holds more accurately at high air gaps, a proportionality constant was determined for the point g = 25mm. The constant was used with the inverse squared relationship to create the theoretical force vs. gap curve shown as the dashed curve in the figure. The inverse squared relationship matches the 16mm gap data point but diverges widely afterward. The linear trend of the experimental curve at smaller air gaps is due to saturation of the two magnetic materials (Roters, 1941). It is therefore concluded that the effect of air gap on the total magnetic force is proportional to the inverse of the gap squared for air gaps greater than 16mm, but follows a more linear trend at lower air gaps.

Force tests were performed with the 1" electromagnet as well. Figures 5.12 to 5.16 display the results of the 1" electromagnet force tests with the five high-purity iron filled rubber samples.

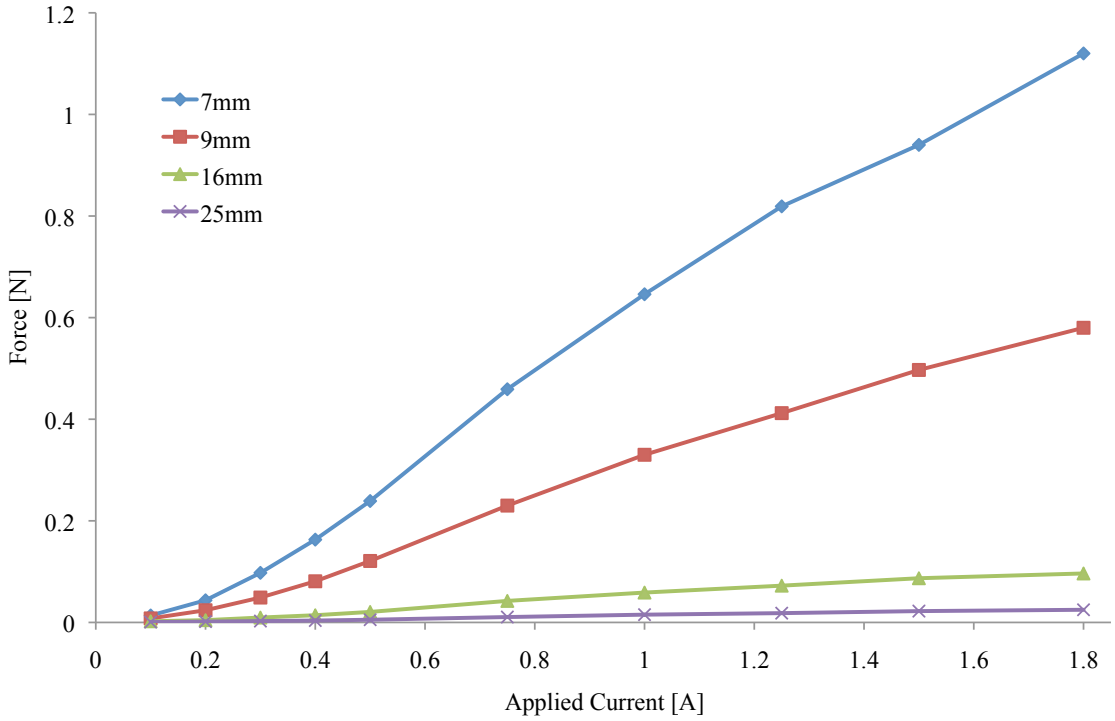

Figure 5.12 Force data of sample 1 (10.7mm, 30%) at four air gaps with 1" electromagnet

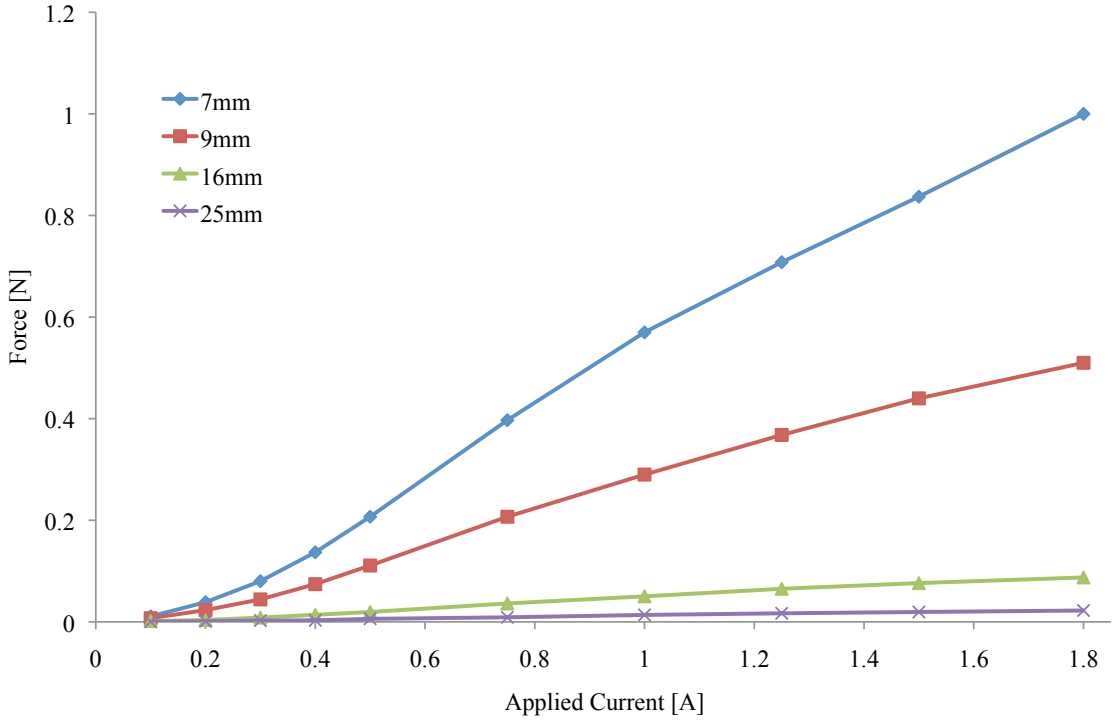

Figure 5.13 Force data of sample 2 (6.5mm, 30%) at four air gaps with 1" electromagnet

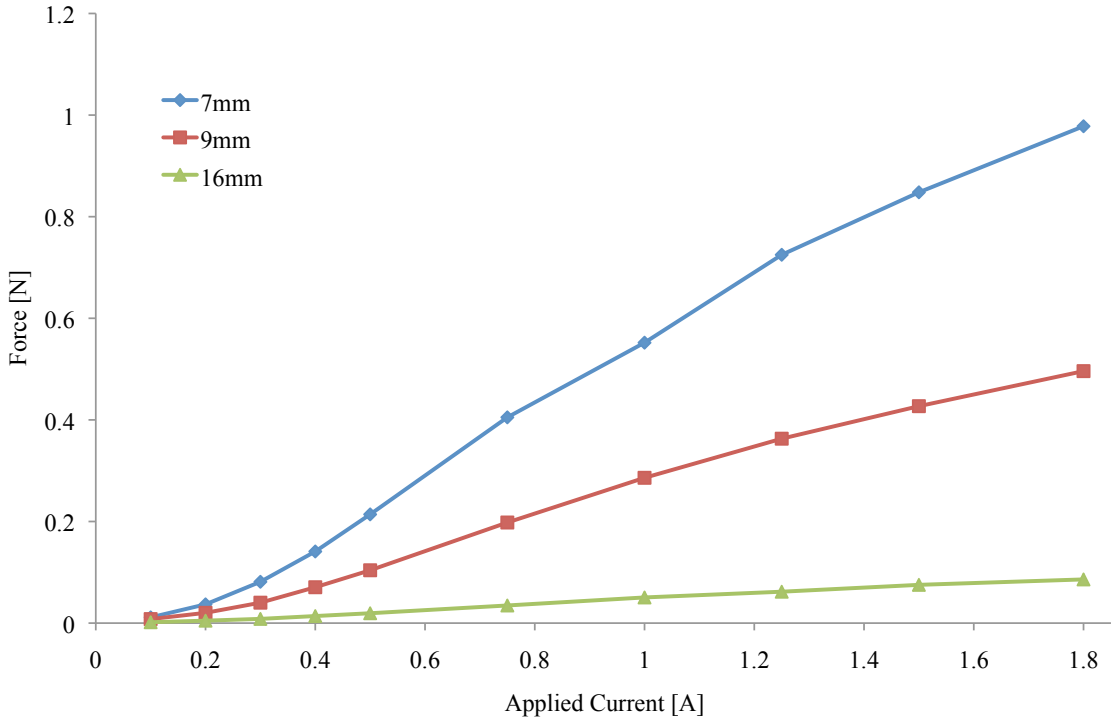

Figure 5.14 Force data of sample 1 (10.2mm, 23%) at three air gaps with 1" electromagnet

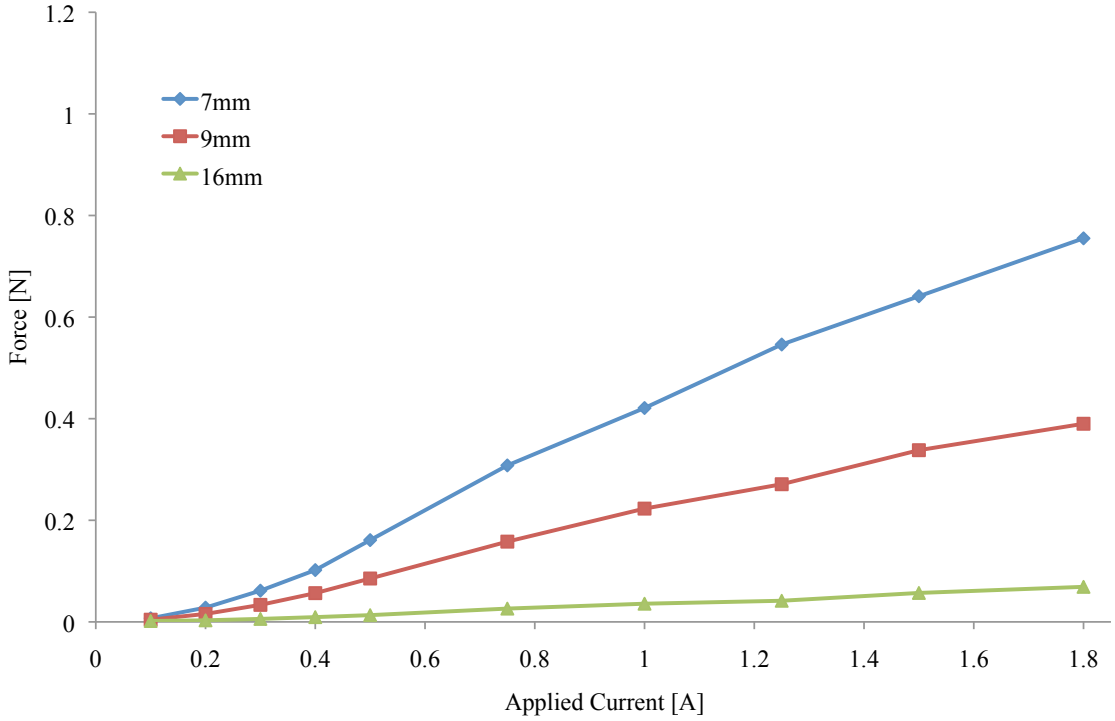

Figure 5.15 Force data of sample 1 (10.1mm, 15%) at three air gaps with 1" electromagnet

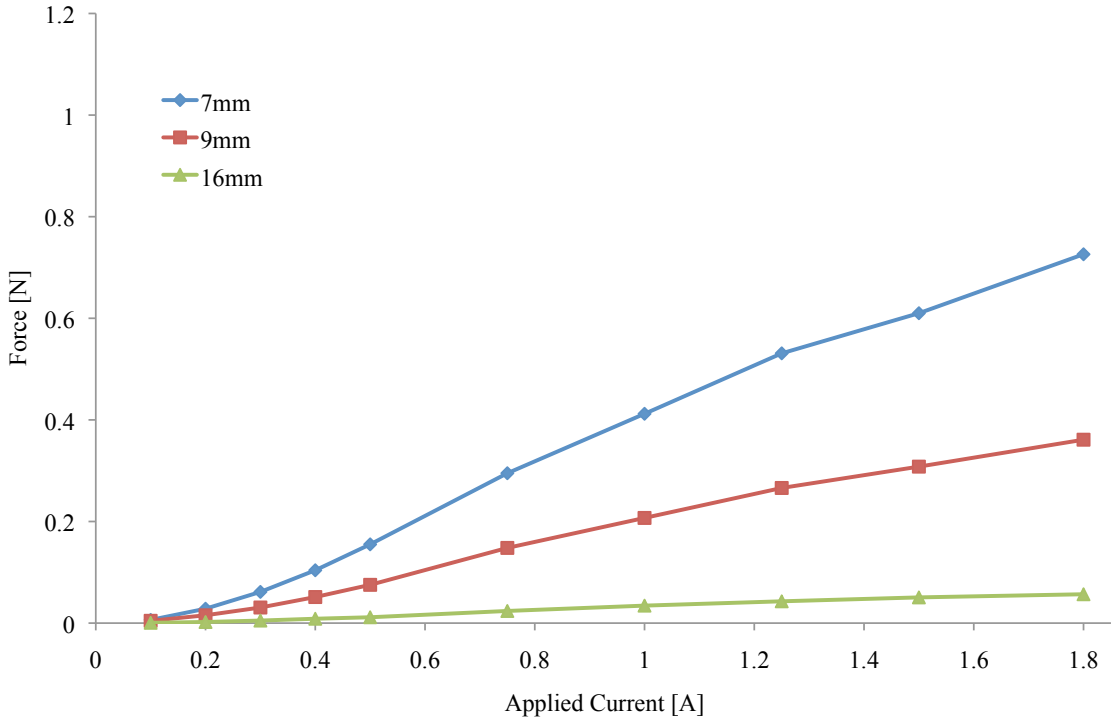

Figure 5.16 Force data of sample 1 (6.4mm, 15%) at three air gaps with 1" electromagnet

Figures 5.12 and 5.13 display attractive force data of the 1" electromagnet at four air gaps, whereas Figures 5.14, 5.15, and 5.16 show force data for three air gaps. The 25mm gap curve is omitted in the latter cases because its force values are extremely low. The curves display trends similar to those of the 6" electromagnet force experiments; they are initially quadratic but flatten out into more linear trends. The results with higher observed forces also show a slight downward curvature at high applied currents. The independent parameters t and ϕ also have effects similar to those for the 6" electromagnet force data. The air gap, however, has a much more pronounced effect. In the case of the 6" electromagnet the force data gathered at high currents are roughly 4 to 5 times greater from the 25mm air gap to the 7mm air gap. The proportion is closer to 50 in the case of the 1" electromagnet, due to a flux leakage phenomenon discussed in section 6.5.

This section shows the experimental results of the 6" and 1" single electromagnet force tests with the five high-purity iron filled rubber samples. The trends that were observed and the effects of the four independent parameters were discussed. Magnetic saturation and flux leakage were presented as phenomena responsible for some of the trends. These phenomena are investigated with the assistance of the FEA model and discussed in section 5.3 and 5.5.

5.3 Model Validation

This section discusses the ability of the FEA model to accurately simulate the magnetic system. The model is used to solve for the total magnetic force at a number of the experimental parameters, as presented in section 5.2, for comparison and validation of the model. The axial B-field along the radius of the face of the 6" electromagnet is measured and compared with the predictions of the model as a secondary validation method. These validation methods serve to verify that the model may be used to accurately simulate the field phenomena involved in the system and to predict the magnetic forces possible at higher applied currents and different system parameters.

5.3.1 Experimental and Model Force Comparison

The axisymmetric model of the 6" electromagnet and armature, the construction of which is discussed in section 6.3, was used to simulate the experiments performed with the five rubber samples of different thicknesses and iron loading percentages. The magnetization models determined experimentally with the vibrating sample magnetometer, shown in Figure 6.8, were applied to the rubber component. The model solved for the total force acting in the axial direction on the component.

Figures 5.17 to 5.21 display the experimental results as points and the model results as solid curves. The experimental data are identical to the curves displayed in Figures 5.3 to 5.7. The model was solved at 8 to 10 points in order to save processing time. Each figure displays experimental and model results for the four air gap values, which are labeled next to the curves for clarity. Recall that samples 1 and 2 are the $\phi =$ 30% rubber, sample 3 is the $\phi = 23\%$ rubber, and samples 4 and 5 are the $\phi = 15\%$ rubber.

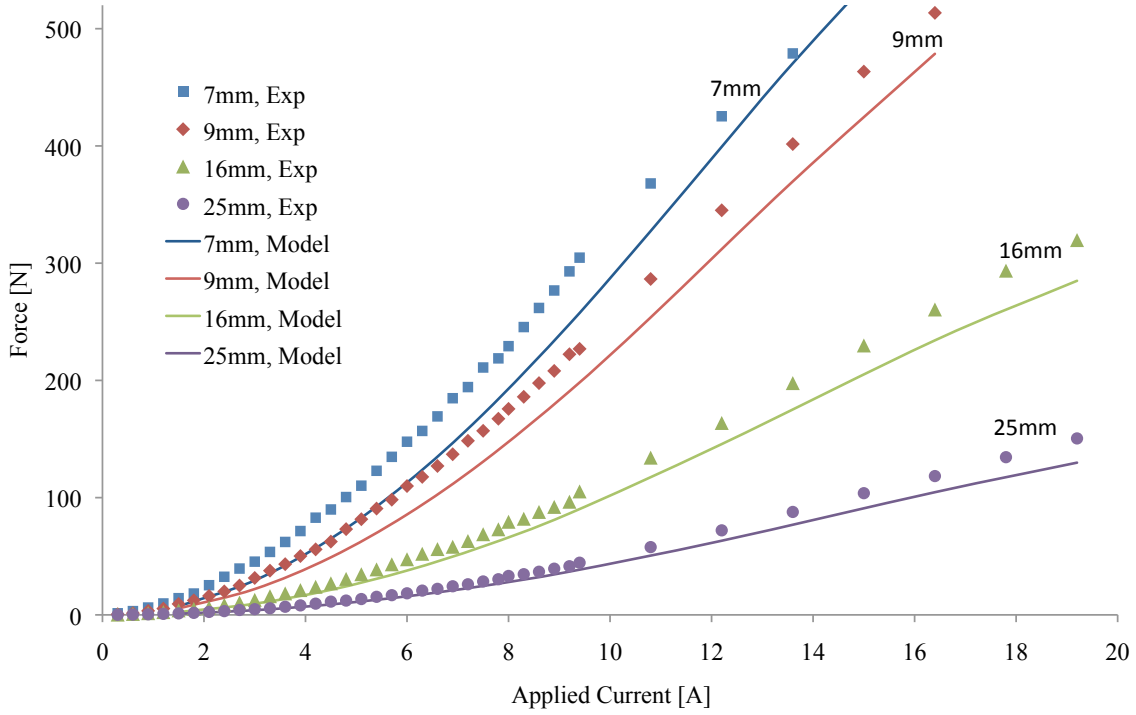

Figure 5.17 Sample 1 force data comparing experimental data and model at four air gaps

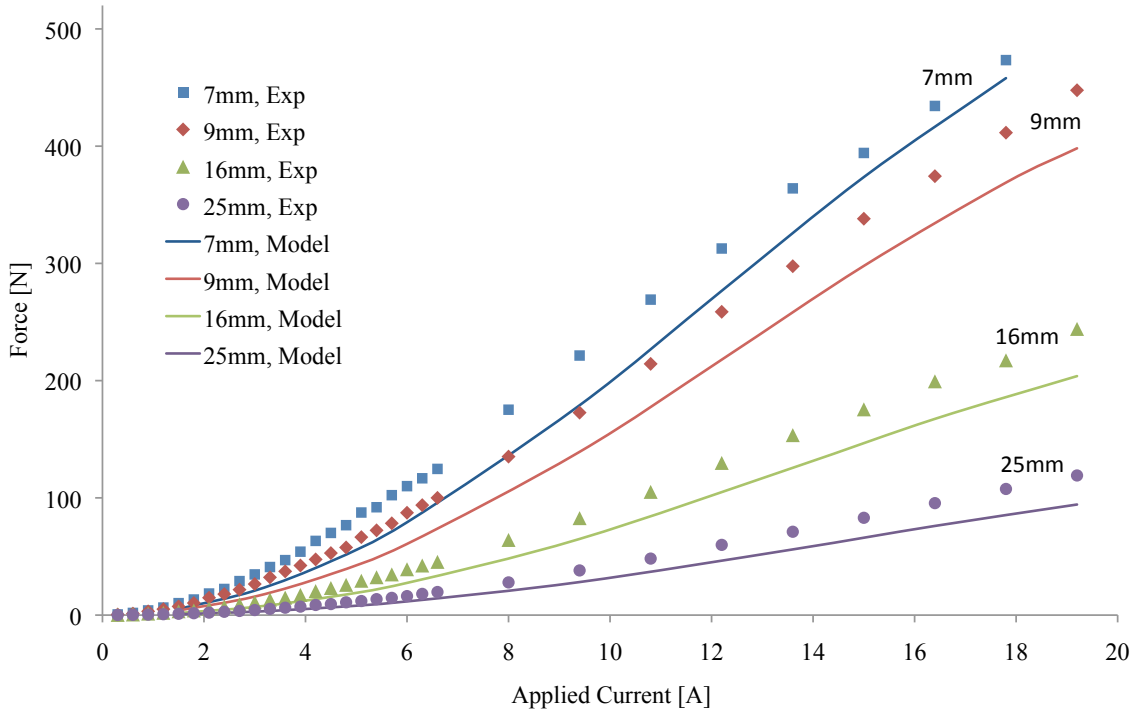

Figure 5.18 Sample 2 force data comparing experimental data and model at four air gaps

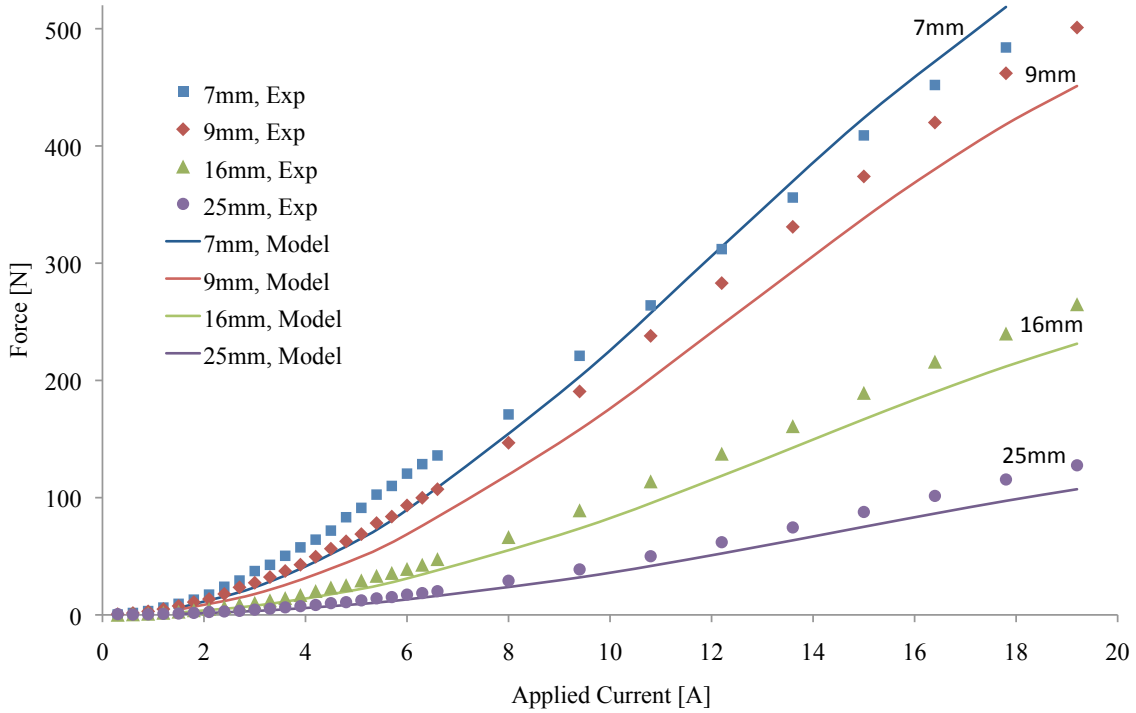

Figure 5.19 Sample 3 force data comparing experimental data and model at four air gaps

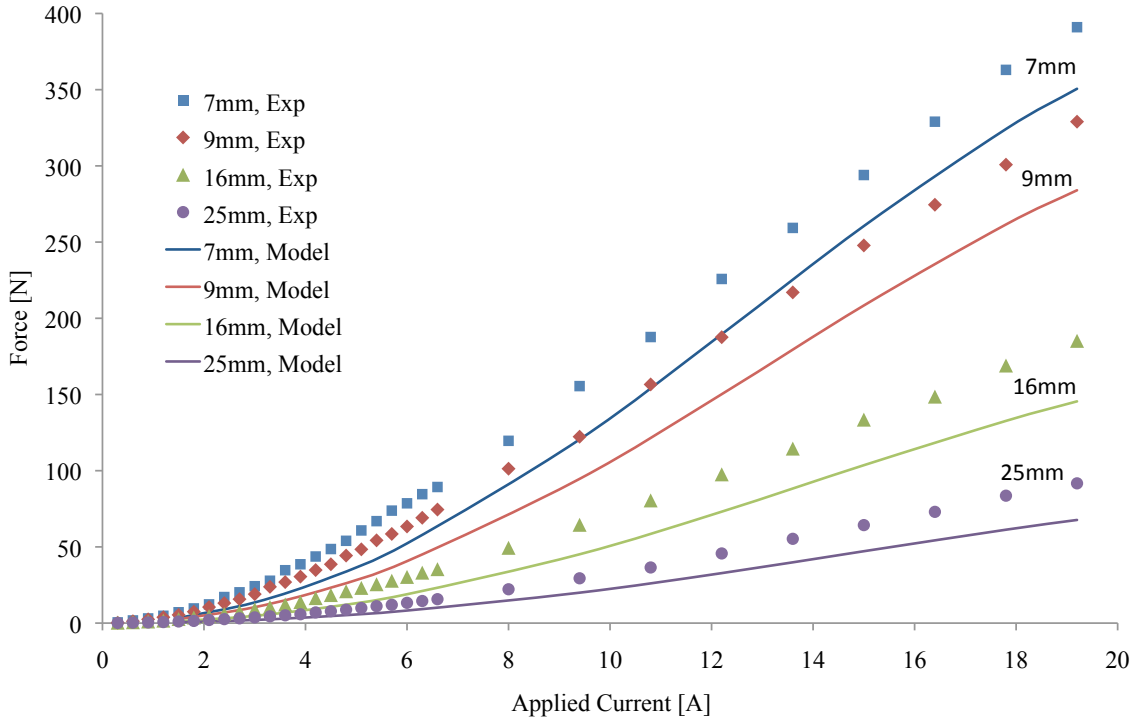

Figure 5.20 Sample 4 force data comparing experimental data and model at four air gaps

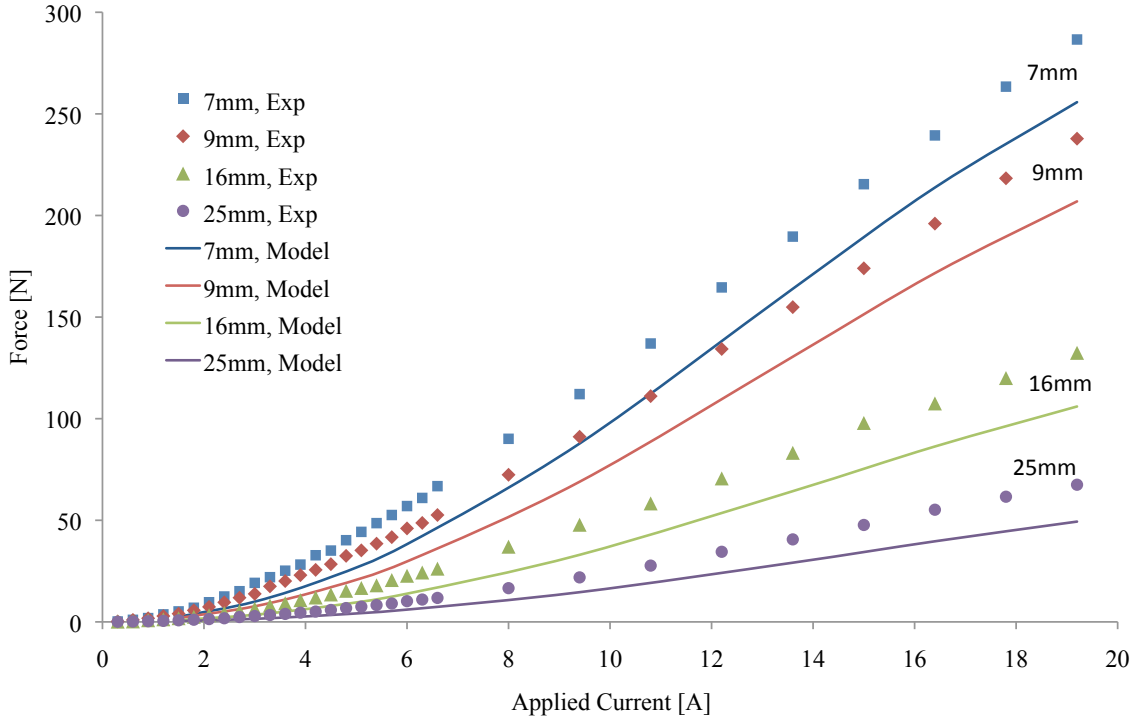

Figure 5.21 Sample 5 force data comparing experimental data and model at four air gaps

Figures 5.17 and 5.18, which refer to the $\phi = 30\%$ rubber samples, show good agreement between the experimental and model results. In all eight curves the model values are offset slightly below the experimental values, indicating that the model underestimates the magnetic force. In general, the error between the model and experimental values decreases with increasing current. This discrepancy is discussed later. Figure 5.19 shows that the $\phi = 23\%$ rubber samples are in good agreement with the model, although the 7mm gap case is slightly under predicted by the model. It is also noted that the agreement is slightly worse in Figures 5.20 and 5.21 which may indicate that the magnetization model used for the $\phi = 15\%$ rubber is not as accurate as the other magnetization models because no other experimental parameters were changed. It is important to restate that the primary purpose of the model is to allow for extrapolation. The experimental apparatus did not allow for the application of current over 20A and was limited to two sizes of electromagnets. Extrapolation with the model gives an approximate idea of the level of clamping pressure possible with a device of different geometry and air gaps and driven at higher applied current levels. As such, the fact that the model curves follow the experimental trends and remain parallel with the data at the maximum applied currents is encouraging. Furthermore, the model and data were compared at a broad range of experimental parameters and showed agreement across the range, which indicates that the model is robust. Because the thick, 30% loaded sample provided the greatest force, analysis is performed to quantify the error between its experimental forces and the model. Figure 5.22 shows the percent error of the model with respect to the experimental values for the thick 30% loaded sample at the four air gaps.

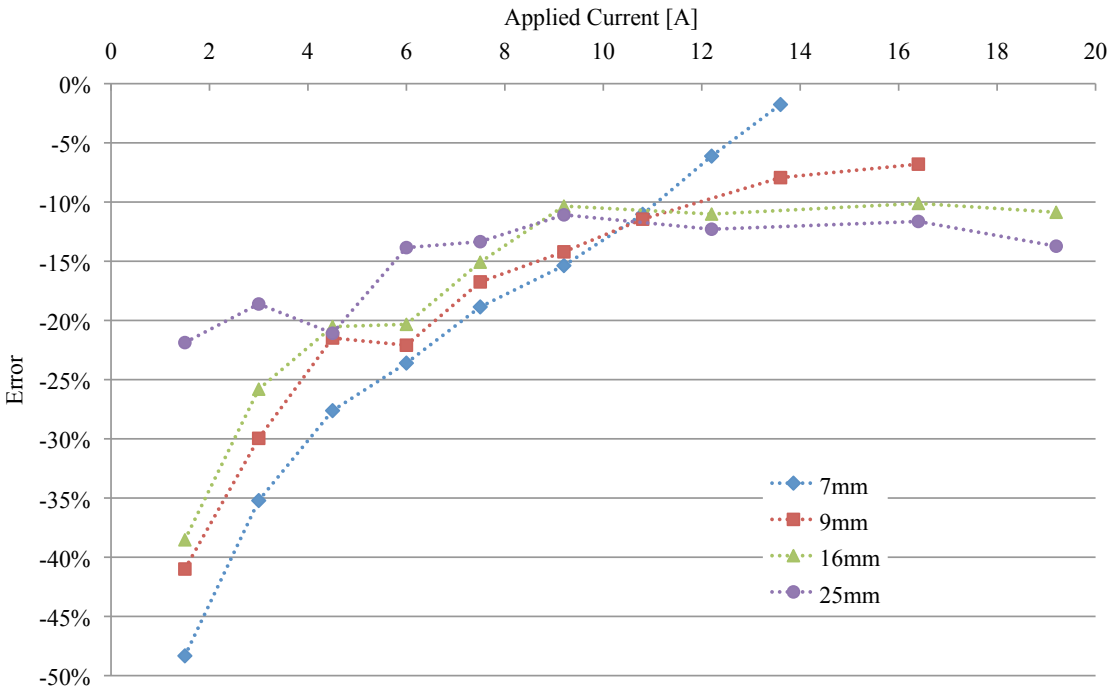

Figure 5.22 6" electromagnet model error for sample 1 data at four air gaps

As previously mentioned, the error is high at low applied currents and decreases with higher current. The 16mm and 25mm air gap cases model the system with 10% error at I = 10A, with the error tending to increase at current increases. The 7mm air gap case begins with the highest error and displays the lowest error at its maximum current value. However, its trend suggests that at even higher applied currents the model values may diverge from the data and over estimate the magnetic force. The 9mm air gap case converges to the lowest error at high currents. The observed trends of the error curves are similar for all of the other 6" electromagnet force experiments. With regard to current extrapolation, the error curves indicate that the model may overestimate the force in all cases at small air gaps and underestimate the force for air gaps over 9mm.

A first-order sensitivity study was performed on the sample 1 data at the 7mm gap to determine how sensitive the model is to small variations in the parameters. The

purpose of the study is to show how the model bounds the variation in the experimental data. The coil number N and the current I are both directly proportional to the force whereas the air gap, g, is inversely proportional to the force. These three parameters were allowed to vary by $\pm 5\%$, which is a reasonable estimate of the experimental error that is possible in the data. The model solved with N and I increased by 5% and with g decreased by 5% is used as the upper bound and the model with N and I decreased by 5% and with g increased by 5% is used as the lower bound. Figure 5.23 displays the experimental results as data points, the model as a solid line, and the upper and lower bounds as dashed lines.

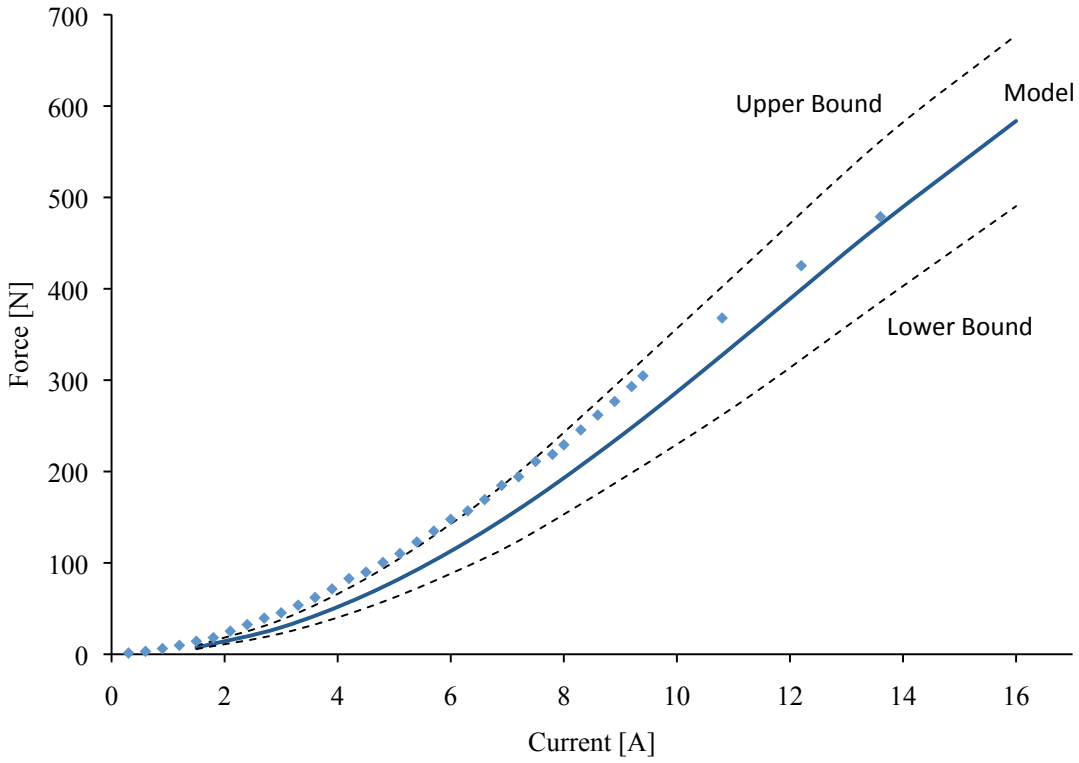

Figure 5.23 5% upper and lower bound on sample 1, 7mm data

The upper and lower bounds contain the data well above I = 6A but do not completely contain it below 6A. The results indicate that the model does not predict the

force accurately at low applied currents and that the error is likely not due to experimental variation. One possible explanation of the error is that the BH curve of the rubber material was not properly measured at low applied fields by the VSM. If the BH curve underestimates the rubber's initial permeability, it would cause the model to underestimate the force. Inspection of the upper end of the figure, however, shows that the model contains the experimental data well within the bounds of experimental variation. Fortunately, for the purposes of this thesis, error at low applied current is acceptable given that the model matches the overall trends of the data and does not diverge from the data. The primary concern of the thesis is to approximate the capabilities of the magnetic clamping device at high magnetic fields and the previous comparisons indicate that the model may be used for this purpose.

The axisymmetric ANSYS model of the 1" electromagnet was also used to simulate the magnetic force at the experimental parameters. Figure 5.24 shows the results of the 1" electromagnet model force simulation compared against the experimental data for the thick, 30% loaded sample. Only the 7mm and 9mm air gaps are shown because the larger gaps have only negligible forces. In both cases the model results follow the experimental curve trends well but have a large offset.

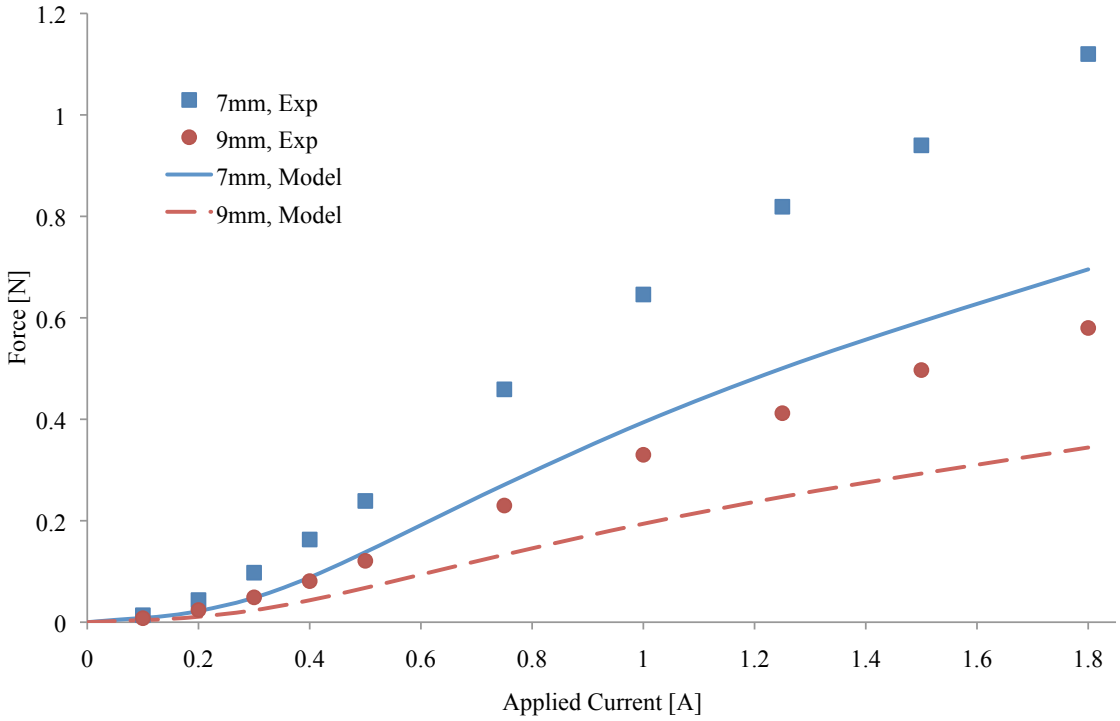

Figure 5.24 Sample 1 force and model data comparison for 1" electromagnet at two gaps

Figure 5.25 shows the error between the model and the experimental values. The model has higher error at lower applied currents just as was observed with the 6" electromagnet model. The error for both air gaps converges to approximately 40%. These results are typical for the rest of the 1" electromagnet model data with the other samples; in general, the model captures the experimental trends well but reports forces that are 40% less than the actual values.

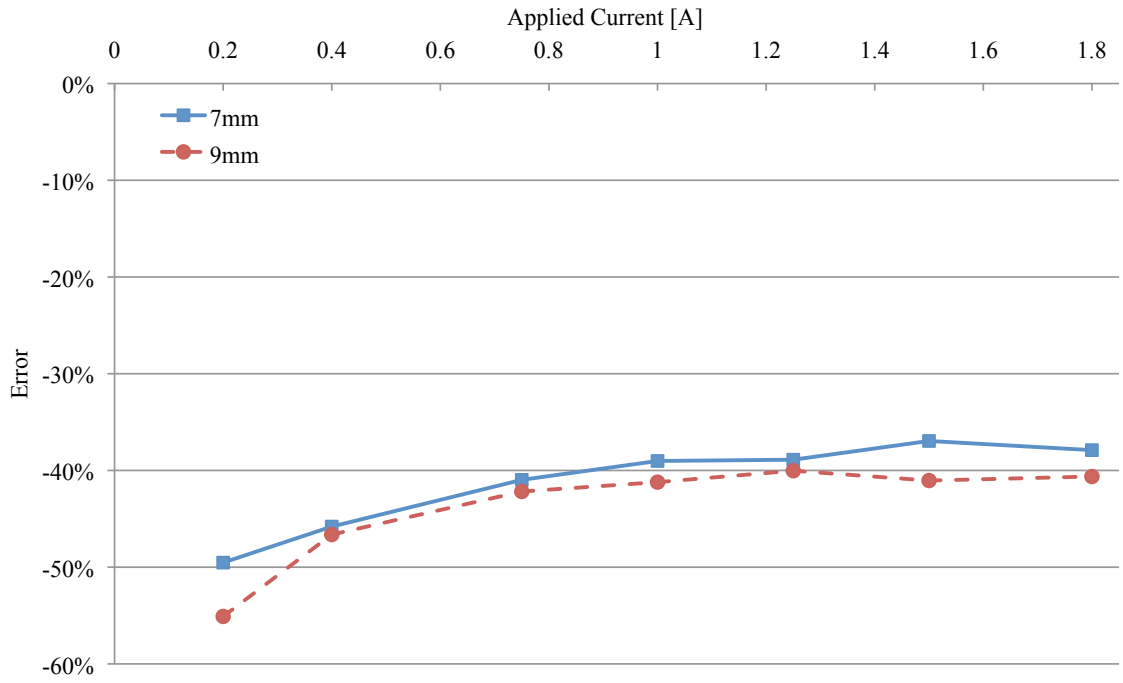

Figure 5.25 1” electromagnet model error for sample 1 data at two air gaps

The error analysis of the 6” electromagnet force data demonstrated that the model becomes more inaccurate at high air gaps. The 1” electromagnet model involves air gaps that are proportionally much higher than those in the 6” model. As such, it is likely that the 40% error observed between the data and the model is due to these large air gaps. The 1” electromagnet force experiments also showed poor clamping forces, which indicates that numerical modeling of very high air gap situations is not useful to the development of the clamping device. Further error analysis of the 1” electromagnet model is foregone, therefore, and it is recommended that the model not be used.

The 6” and 1” electromagnet models were solved at a number of process parameter values in order to simulate the magnetic force experiments. Both models displayed the ability to capture the trends of the experimental data over the range of parameters. However, in all cases the model underestimated the force at low applied

currents. The 1” model underestimated the force more severely than the 6” model. This may be due to the proportionally larger air gap with respect to the electromagnet diameter used in the 1” electromagnet force experiments. The model of the 6” electromagnet shows some tendency for the error to converge to approximately 10% for the 9mm, 16mm, and 25mm air gaps with the $\phi = 30\%$ and $\phi = 23\%$ samples. The error converges to about 15% to 25% for the $\phi = 15\%$ samples. The 7mm air gap results show a tendency of the model to overestimate the magnetic force at high current values.

The error observed in both models, as shown in Figure 5.22 and 5.24, show distinct patterns that cannot be attributed to experimental error or variability. The presence of such patterns indicates that there are physical effects in the system that the model does not capture entirely. It is possible that the magnetization models used for the rubber have some inaccuracies and that the model cannot capture the effects of very high air gaps in the clamping system. Direct comparison of the actual and simulated magnetic field is performed in section 5.3.2 as a further model validation step.

5.3.2 Gaussmeter Validation of Field Model

A Gaussmeter was used to measure the magnitude of the axial B-field along the radius of the face of the 6” electromagnet. The experiment was performed with the thick 30% sample, the thick 15% sample, and without a sample. A range of applied currents and air gaps were used. The process parameters were input to the field model of the 6” electromagnet and solved. The axial B-field (the y-direction in the model) reported by the model was recorded at the same locations as the Gaussmeter probe. The purpose of this procedure is twofold. First, comparisons of the B-field profiles generated experimentally and by the model serve to validate the ability of the model to show the field details of the

magnetic system. Second, inspection of the profile of the magnetic field gives insights into the pressure generated at the face of the part as given by Equation 3.9.

Figure 5.26 shows the B-field along the radius of the 6" round electromagnet at current values of 1.5A, 6A, and 15A. Note that the radial position of zero refers to the middle of the electromagnet. In this case there is no magnetic rubber coupling the flux to the electromagnet; the magnetic flux path is simply generated in the air space above the electromagnet. The experimental curves show a maximum peak at the 1.375" position and minimum peak at the 2.625" position. These extremes occur at the edge of the core and the inner edge of the pole.

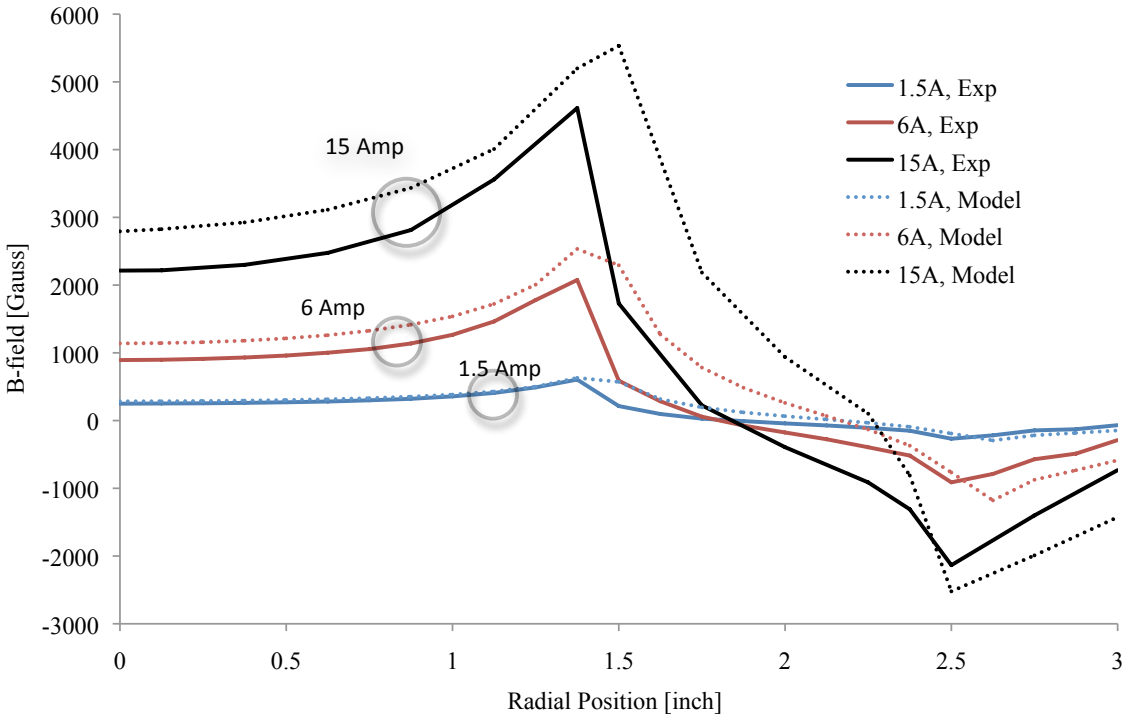

Figure 5.26 Model and actual axial B-field with no sample at three current values

The field is positive over the core of the electromagnet and negative over the pole because the flux must complete a path around the coils. As expected, higher applied currents result in higher B-field magnitudes. The model curves agree with the

experimental curves reasonably well. The field magnitudes are comparable with the model but show a tendency to overestimate the field magnitude. The model field profiles also appear offset from the experimental values by about 0.125". In other words, if the model curves were shifted by 0.125" toward the center of the electromagnet they would match the experimental values better. This may be due to an error in the positioning of the Gaussmeter probe or an internal feature of the electromagnet that was not modeled properly.

Figure 5.27 displays the model and experimental results of the axial magnetic field with the thick $\phi = 30\%$ sample at an applied current of 6A. Curves are shown for air gaps of 10mm and 20mm. The same trends in the profile appear as observed in Figure 5.26 including the local maxima and minima. The model matches the experimental field magnitude fairly well but again shows a radial offset. The field magnitude is higher at all points at the smaller air gap but the profile shape remains unchanged suggesting that the field profile shape at the face of the electromagnet is not strongly affected by the air gap.

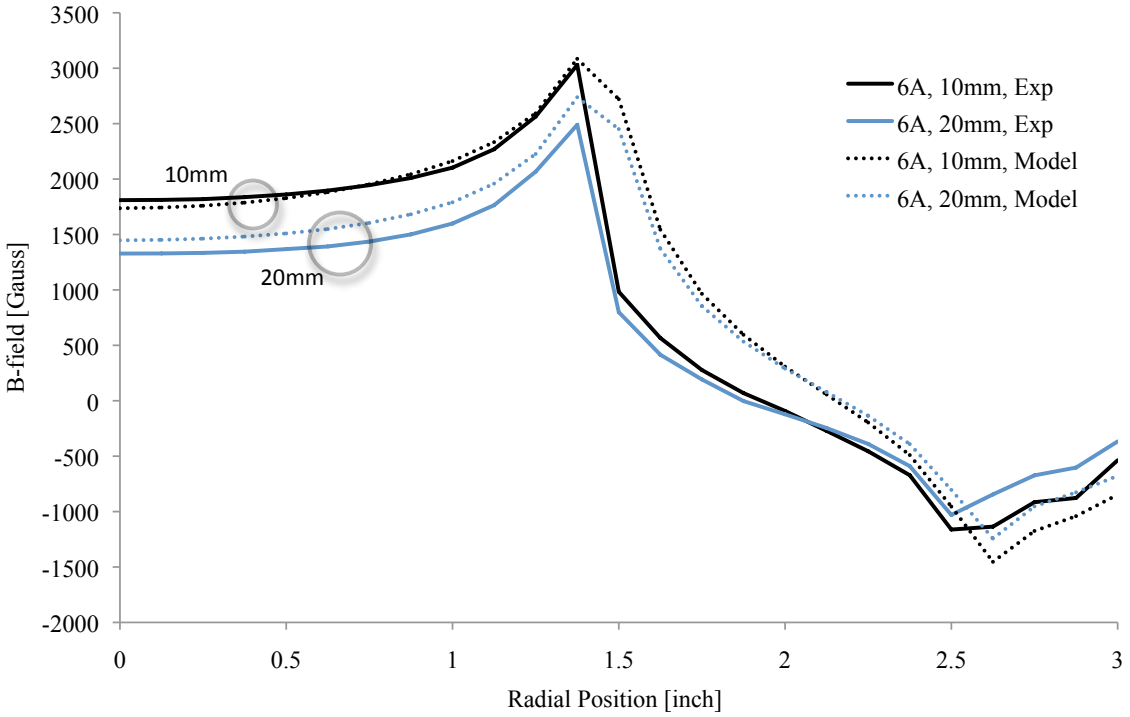

Figure 5.27 Model and actual axial B-field with sample 1 at two air gaps

Figure 5.28 displays the B-field profile with the thick 30% sample and thick 15% sample at an air gap of 20mm and applied current of 15A. The data for the 30% sample are shown as solid lines and the data for the 15% are dashed. The thinner-weighted lines refer to the model results. The results show that the B-field is greater with the more heavily iron-loaded rubber sample. As is the case with the previously discussed experiments, the model displays a tendency to overestimate the magnitude of the B-field and is shifted from the experimental profile in the radial direction.

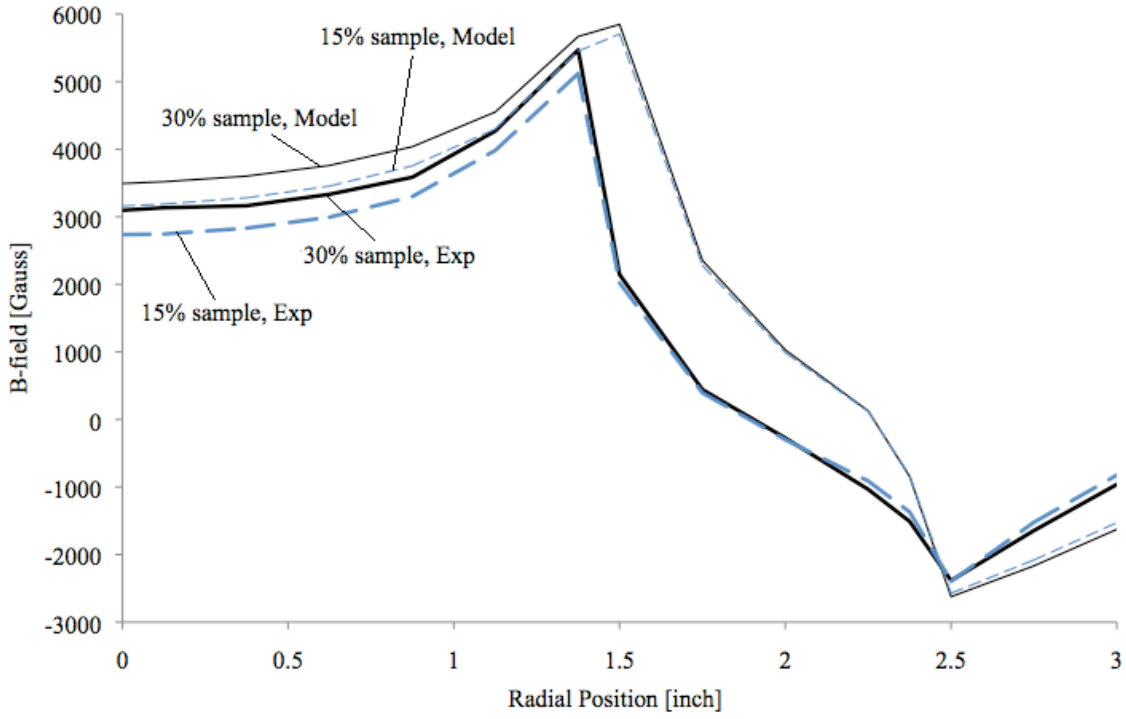

Figure 5.28 Model and actual axial B-field with samples 1 and 4 at g = 20mm, I = 15A

The results of the Gaussmeter tests demonstrate that the numerical model simulates the actual distribution of the magnetic field with reasonable accuracy. Some discrepancy exists with regard to the location of the maxima and minima of the field profile. The model overestimates the magnitude of the B-field by up to approximately 15% in the experiments with the two rubber samples. However, the model still offers valuable insights into the internal magnetic field characteristics of the magnetic clamping system and electromagnet.

An FEA model developed in ANSYS was used to simulate the magnetic field interactions in the magnetic clamping system and calculate the total attractive force between a magnetic rubber armature and a round electromagnet. Table 5.1 displays the pros and cons of the model.

Table 5.1 FEA device model pros, cons, and comments

Cons	Comments
Poor accuracy at low applied currents	Possibly due to error in low-field magnetization of rubber. Not a concern for well-designed clamping device
Poor accuracy at very high air gaps	
No structural modeling	Needs direct magneto-structural coupling, structural models of components and part, and field stiffening effect of rubber
Pros	**Comments**
Converges at high currents	Useful for device design and current extrapolation
Robust and flexible	Allows for wide variation in most parameters without error penalty
Scalable	Model results are applicable at different geometric scales
Solves for internal state of system	Internal phenomena such as saturation and flux leakage may be analyzed

Table 5.1 provides brief comments about the pros and cons of the numerical model. Comparison of the force values predicted by the model with experimental values indicates that the model is able to qualitatively capture the effects of the experimental parameters: volume fraction of the rubber, air gap, armature thickness, and applied current. The fact that the accuracy of the model is not severely compromised with a combination of changes in the experimental parameters means that the model has robustness and flexibility. The model of 6” electromagnet showed a better fit to the experimental data than the 1” electromagnet, which may be due to the proportionally large air gaps involved in the 1” electromagnet model. Both models simulated the trends of the force curves well but with varying degrees of error. The B-field along the face of the electromagnet also was simulated and compared to the experimental measurements. The model demonstrated the ability to predict the internal magnetic field state of the

system with reasonable accuracy despite the geometric complexity of the problem and the magnetic nonlinearity of the materials. Later sections discuss the ability of the model to scale with the geometry of the clamping system and to provide structural modeling of the clamping forces. In conclusion, the FEA model may be used to qualitatively investigate the internal magnetic field characteristics of the clamping system and the effect of process parameters on the total attractive force. Quantitative results obtained with the model at low applied currents must be treated with care as substantial errors may exist in its force predictions. However, at large applied currents and smaller air gaps the model displayed force prediction errors of approximately 10%. In addition, inspection of the error trends indicate that the model can be used to predict the effects of applied currents greater than utilized experimentally. Therefore, it is concluded through experimental validation that the FEA model may be used as a tool to predict approximate clamping forces, which will aid in determining the feasibility of a magnetic clamping device for consolidation of composite laminates. In the following sections, the model is used to determine the realistic limits of operation of the device.

5.4 Device Design Proportions from Theoretical Considerations

Whereas the previously described force experiments involved single electromagnets, a large-scale clamping structure must utilize an array of similar electromagnets in order to consolidate large composite parts. The design of the individual electromagnets is considered in this section. Section 5.6 discusses the utilization of an array of such electromagnets and the magnetic field interactions between neighboring electromagnets. The design of a magnetic clamping device begins with the specification of the thickness of the composite part to be consolidated. The thickness of the part acts as

the air gap in the system, *g*, which is a critical design parameter. The electromagnet and armature geometry best suited to operate at a certain air gap is investigated theoretically in this section.

It is proposed that flux leakage phenomena inherent in the tractive electromagnet system requires that a characteristic proportion, *k*, relating the air gap to the size of the electromagnet, must be minimized for the device to be effective. This section discusses the development of *k* based upon flux leakage estimation methods in standard electromagnet design texts. Magnetic circuit analysis and flux path visualization via the FEA model are used to characterize flux leakage. Another proportional value, *z*, is introduced as a guideline in the specification of the armature design parameters. The development of *k* and *z* are discussed from a theoretical standpoint in this section. These ratios are used with the model in section 5.5 to optimize the design of the clamping device and determine the realistic clamping pressures the device may be expected to achieve.

5.4.1 Qualitative Discussion of Flux Leakage

As discussed in section 5.1.3, a flat-faced electromagnet generates magnetic flux through the coupling of a permeable armature across its pole and core. Referring to Figure 5.1, the objective of a tractive electromagnet and armature system is to produce flux normal to the air gap between the face of the electromagnet and the armature. The flux in the working air gap is referred to as useful flux. The path of the useful flux traverses the two working air gaps and the length of the armature in series. The B-field in the working air gap is found by dividing the useful flux by the cross-sectional area of the air gap. Equation 3.9 shows that the tractive stress on the face of the armature is related

directly to the square of the normal B-field. The useful flux developed in an electromagnet system is always less than the total flux due to the tendency of magnetic flux to leak through alternate paths and essentially "short-circuit" the useful flux path. It is desirable to minimize the flux leakage in order for the device to operate efficiently. The FEA model is used to develop flux path images for qualitative discussion of the leakage paths. Note that the model is solved using a high value for the permeability ($\mu_r = 1000$) of the electromagnet back-iron and the armature in order to develop clear, characteristic flux paths. Low permeability of the armature and saturation of the components distort these characteristic paths. As such, the leakage paths discussed in this section are not perfectly representative of those developed in the actual system. However, the high-permeability assumption offers a straightforward method to study the system and utilize classic electromagnet design methods.

In a flat-face electromagnet and armature system the total flux generated by the magnetomotive force, *NI*, may take four complete paths as it completes the circuit around the coil. It is helpful to break the complete paths down into discrete circuit elements, which is shown in Figure 5.29.

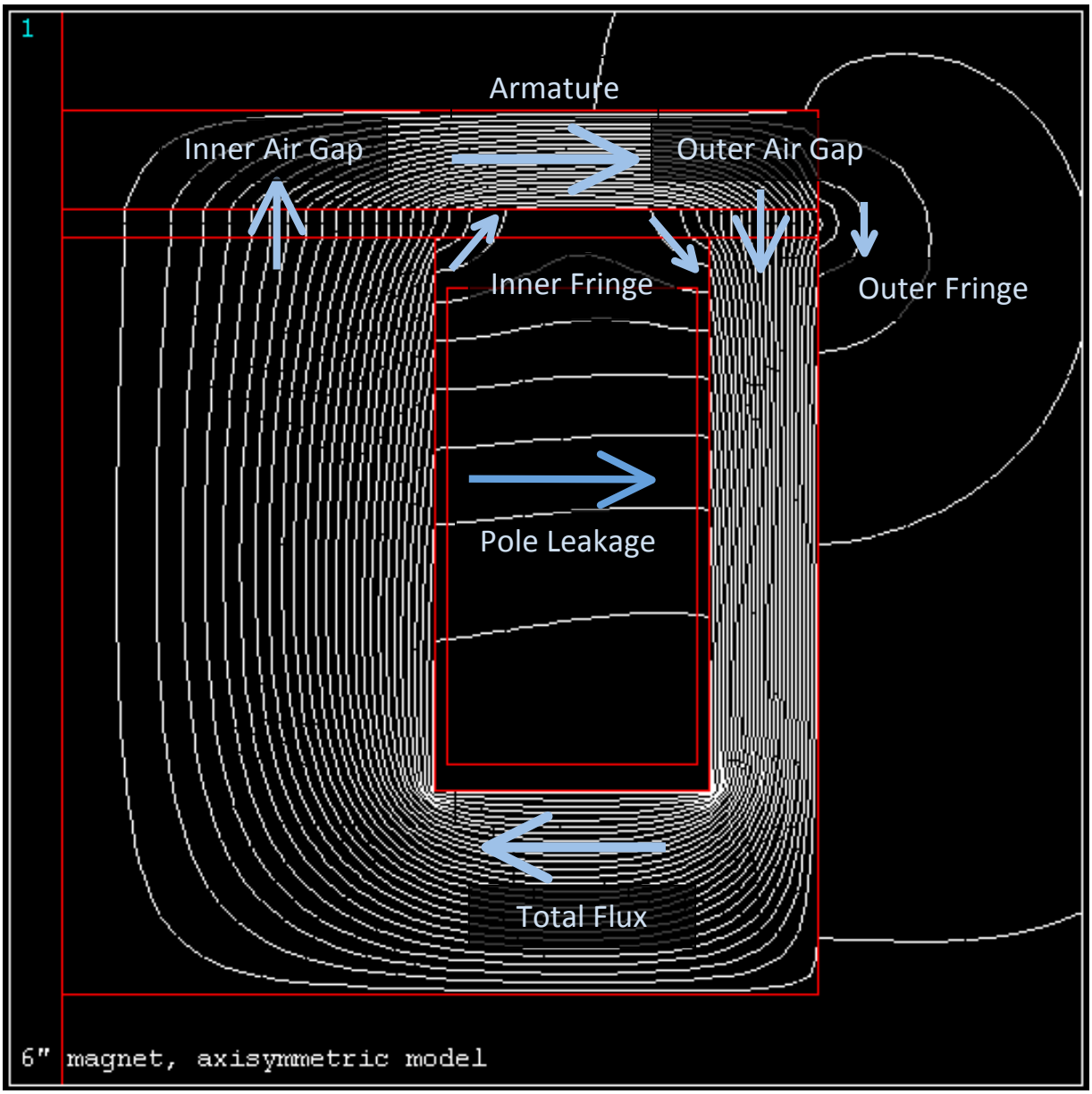

Figure 5.29 Flux leakage of general electromagnet system with small air gap

Figure 5.29 shows a variety of flux path circuit elements that comprise three of the four possible complete flux paths. The two elements directly between the armature and the core and pole face of the electromagnet are the inner and outer working air gaps, respectively. The center of the armature is also considered a path element. The fringe flux elements called out in the figure represent flux that is generated between the

electromagnet and the armature but which does not contribute to the attractive force between them. Finally, the air space of the coil presents a substantial path element called the primary pole leakage. The path elements in the figure constitute three complete parallel paths. The path of the useful flux follows the inner working air gap, the armature, and the outer working air gap elements. The second flux path passes through the armature via some combination of the fringe elements. The third path does not traverse the air gap but simply jumps from the core to the pole.

Figure 5.30 displays the flux paths present when the air gap is proportionally large. All of the path elements shown in the previous figure remain except that the inner fringe paths are replaced with a secondary pole leakage path. This secondary leakage path is visualized as a half-circular prism lying between the core and pole. The path begins to develop when the air gap is approximately equal to the width of the coil space. As the gap grows, the secondary path develops more fully as seen in the figure.

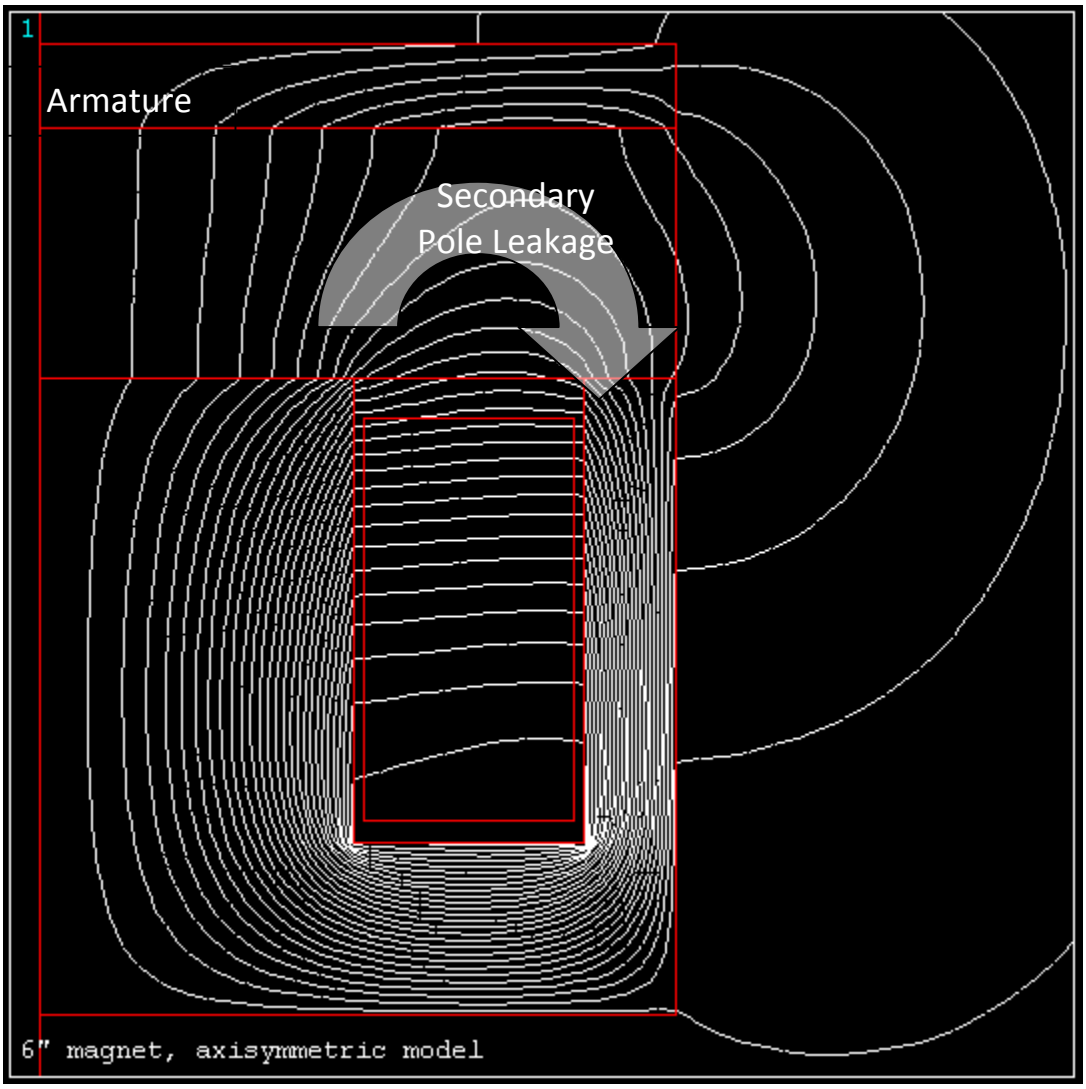

Figure 5.30 Flux leakage of general electromagnet system with large air gap

5.4.2 Air Gap to Electromagnet Radius Proportion, *k*

Round, flat-faced electromagnets, which are used for lifting, are generally designed with similar proportions regardless of their size. These proportions are chosen to minimize flux restrictions within the back-iron and minimize leakage across the coil width. The dimensions of such an electromagnet are shown in Figure 5.31.

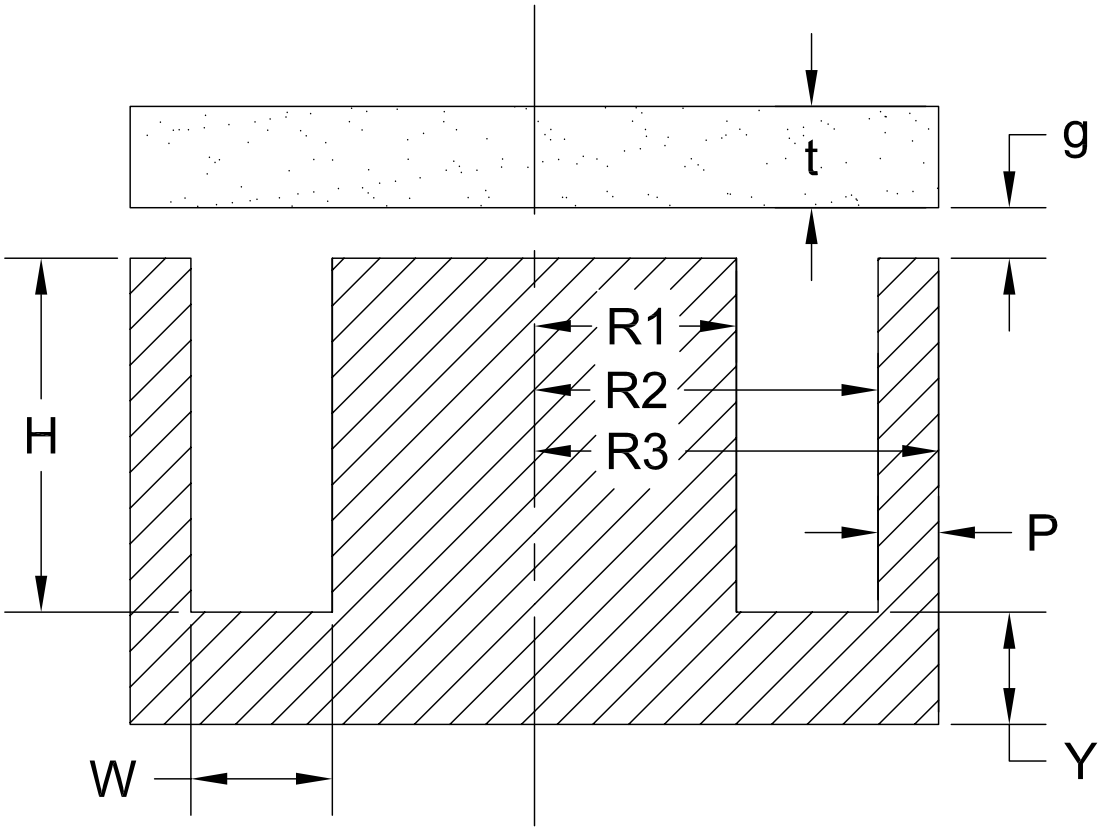

Figure 5.31 Standard round electromagnet design proportions

Figure 5.31 displays the cross section of a round electromagnet that is designed according to standard proportions, which are as follows (Roters, 1941):

$R_2 = 1.7R_1$ $R_3 = 2R_1$ $W = 0.7R_1$ $H = 2.5W$ $P = 0.3R_1$ $Y = 0.555R_1$

The proportions are all based upon the radius of the core, R_1. As such, for the purposes of this thesis it is assumed that any round electromagnets chosen for use in the clamping device will follow these proportions and may be specified simply by R_1. Inspection of the dimensions of the 6" electromagnet used in the force experiments, displayed in Figure 6.4, shows that the electromagnet follows these guidelines closely. The only discrepancy is that, for the 6" electromagnet, $H = 2W$. However, the operation of the electromagnet is not very sensitive to this parameter.

The portion of flux generated by an electromagnet that creates useful force on the armature may be determined from its geometry by the leakage ratio, ν. The leakage ratio is given by Equation 5.1,

$$\nu = \frac{P_{armature} + P_{leakage}}{P_{useful}} = \frac{\Phi_{total}}{\Phi_{useful}} \tag{5.1}$$

where P refers to the permeance (inverse of the reluctance) of the armature, leakage, and useful paths. Comparison of the total system permeance to the permeance of the useful flux path is equivalent the ratio of total flux to useful flux. Because the effective leakage path and useful flux path are in parallel, the flux through the useful path is dependent upon the magnetomotive force, NI, and not upon the leakage ratio. However, this reasoning is based upon the assumption of an armature and back-iron of unlimited permeability. In reality, a high leakage ratio is detrimental to the operation of an electromagnet system because it increases the total flux in the system, which must be carried by the back-iron. As the total flux in the back-iron increases it is pushed toward its saturation limit and the overall reluctance of the system is increased.

For well-designed electromagnets, the leakage ratio is given by Equation 5.2,

$$\nu = 1 + \frac{g}{R_1}\left(\frac{35.3 + 228\, g/R_1}{4 + 35.3\, g/R_1} + 5.1\right) \approx 1 + 13\frac{g}{R_1} \tag{5.2}$$

where g is the air gap in the system (Roters, 1941). The expression may be simplified as shown on the right hand side of Equation 5.2 if $\frac{g}{R_1} < 1$. It is helpful here to define this fundamental relationship as $k \equiv \frac{g}{R_1}$. To better illustrate the effect of the leakage ratio, an

example is considered using the 6" electromagnet with an air gap of 3mm as shown in Figure 5.29 and an air gap of 30mm as shown in Figure 5.30.

Table 5.2 displays the effect of the leakage ratio on the final pressure developed in the working air gaps, assuming infinite permeability of the armature.

Table 5.2 6" Electromagnet leakage ratio comparison

Bsat = 2 T R1 = 38.1mm	leakage ratio	system flux at iron Bsat	flux in air gap	B-field in air gap	Pressure on armature
g = 3mm	2.02	0.009 Wb	0.00445 Wb	0.975 T	**378 kPa**
g = 30mm	11.24	0.009 Wb	0.00080 Wb	0.176 T	**12.3 kPa**

The leakage ratios are calculated using Equation 5.2. Note that the system with the 30mm air gap has a leakage ratio 5 times that of the 3mm air gap system. The calculations in the table are performed such that the back-iron of the electromagnet is saturated at a value of 2 Tesla. The flux density of the back-iron multiplied by the cross sectional area of the core yields the total flux, in webers, of the back-iron and therefore of the entire system. The total flux divided by the leakage ratio, according to Equation 5.1, yields the flux in the air gap. The cross sectional area of the core is again used to determine the B-field in the air gap, which yields the tractive stress after application of Equation 3.9. The results of the calculations indicate that the armature pressure of the 30mm gap system is 26 times less than that of the 3mm gap system.

Figure 5.32 shows the results of the calculations performed in Table 5.2 over a range of values of *k* from zero (no air gap) to unity. The two calculations in Table 5.2 are shown as points on the figure. It must be noted first that the magnitude of pressures are artificially high due to the high-permeability assumption of both the armature and electromagnet back-iron. Given that the device is operating with armatures of relative

permeabilities of at most 2 or 3, the actual pressures will be much lower. However, the graph is still instructive in that it shows the tendency of magnetic pressure to decay exponentially with increasing *k*.

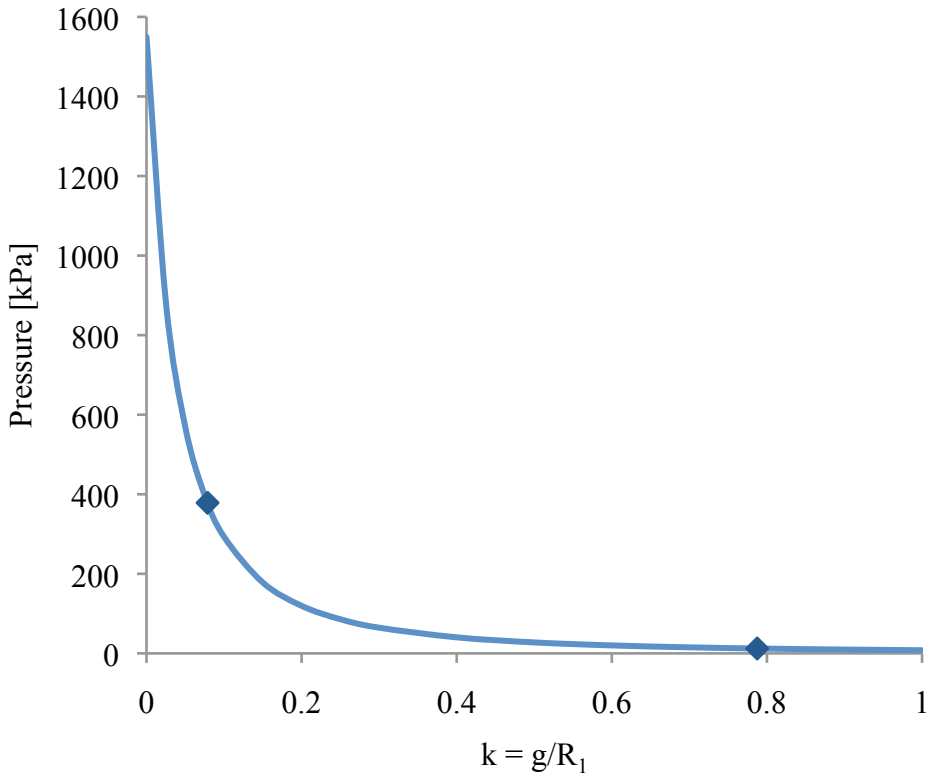

Figure 5.32 Theoretical pressure vs. *k* ratio with electromagnet at 2 Telsa

The calculation results shown in Figure 5.32 operate on the assumption that the leakage ratio equation (Equation 5.2) is valid for the large for values of *k* ranging from zero to unity. Roters developed the equation for use with *k* values below 0.1 as flat-faced lifting electromagnet systems are generally characterized by *k* values closer to 0.02. The equation is most applicable when the flux paths of the system resemble those in Figure 5.29. Figure 5.30 demonstrates the development of secondary flux paths, which become important at values of $k > 0.5$. However, it can be shown with Roters' method of flux path permeance estimation that even at higher values of *k*, Equation 5.2 gives an

acceptable result. Divergence begins at values of k >3; but for the purposes of the composite clamping device only much lower values of k need be considered.

The sample calculations in Table 5.2 and Figure 5.32 serve to verify that, due to saturation of the electromagnet steel, the leakage ratio of a flat-faced lifting electromagnet and armature is a valuable indicator of the ability of the system to develop useful tractive forces. It is also shown that the leakage ratio may be safely approximated as a linear function of the characteristic ratio k. As such, flux leakage is independent of the scale of the system. It is demonstrated that increases in k result in pronounced decreases in pressure, as seen in Figure 5.32. Therefore, it is recommended that an electromagnetic clamping system be designed to operate at k values of around 0.1 or less. In a later section the FEA model is utilized to verify the dependency of the system on k and to perform further optimization of the device in terms of the armature thickness and filler content.

5.4.3 Armature Design Proportions

The consideration of flux leakage phenomena is well-suited to theoretical approximations as air exhibits a linear response to magnetic fields. The iron-filled rubber armature, however, is a nonlinear magnetic material with relative permeability ranging from 3 to unity depending upon the loading fraction, ϕ, and the strength of the applied magnetic field. The reluctance of the armature is dependent upon these two variables and the armature's thickness, t, given by Equation 5.3.

$$R_a = \frac{l_{effective}}{\mu(H) S_{effective}} \tag{5.3}$$

Equation 5.3 is a restatement of Equation 3.13, where $l_{effective}$ and $S_{effective}$ are the effective length and cross sectional area of the armature, respectively. The permeability, μ, is a function of the magnetic field intensity, H, present in the armature as shown in Figure 4.8. In addition, due to the low permeability of the armature material significant flux exists on the side of the armature opposite from the electromagnet.

Figure 5.33 displays the flux paths typical of the actual clamping system. The image was generated by solving the FEA field model of the 6" electromagnet with an air gap of 3mm, current of 15A, and armature parameters t = 10mm and ϕ = 30%.

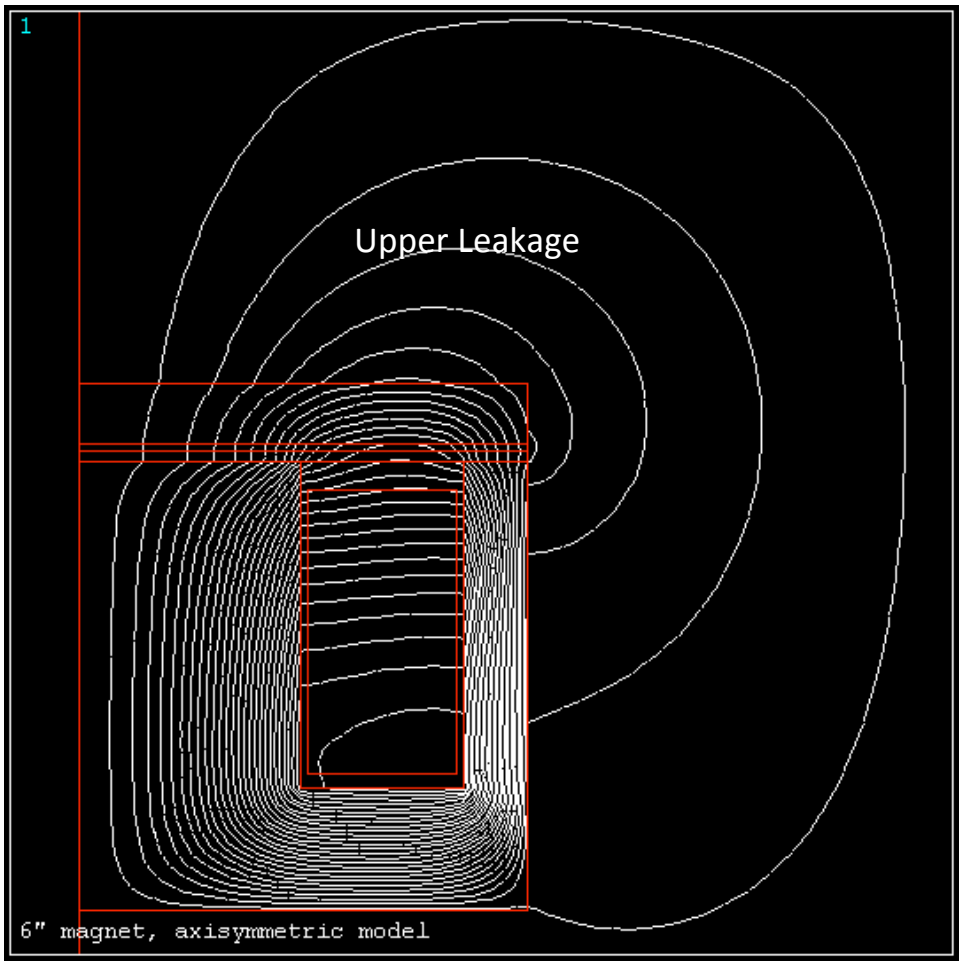

Figure 5.33 Typical flux paths of system with low-permeability armature

The figure shows that the armature is unable to conduct the entire flux that enters it via the air gap and a leakage effect is observed above it. With this in mind, it is expected that the effect of the two process parameters t and ϕ is complex to a degree that FEA modeling is best suited to study their effects. However, in the interest of providing design guidelines for the clamping device, it is proposed that another proportional constant involving these two parameters may be employed to characterize the system.

The useful flux generated by the magnetomotive force of the electromagnet must pass through the back-iron of the electromagnet, the inner air gap, the armature, and the outer air gap in series. The total reluctance of the useful flux path is therefore found by addition of the four reluctance terms. For the purposes of this analysis the back-iron is assumed to be of negligible reluctance due to the relatively high permeability of steel compared with the rubber. This assumption is valid because the permeability of low-carbon steel below saturation is approximately 100 times greater than air or the rubber. In order to minimize the upper leakage effect it is desirable for the armature not to present a significant restriction to the useful flux path. A comparison of the reluctance of the armature to that of the air gaps indicates the degree of such a restriction. The reluctance of the air gaps in series is given by Equation 5.4,

$$R_g = \frac{2g}{\mu_0 \pi R_1^2} \tag{5.4}$$

where g is the air gap, μ_0 is the permeability of air, and R_1 is the electromagnet core radius. It is assumed that the electromagnet follows standard design proportions. The factor of 2 is present because the inner and outer air gaps have the same reluctance and act in series. The effective length of the flux path through the armature, $l_{effective}$, is

approximated as R_1. The effective cross sectional area of the armature, $S_{effective}$, is approximated by Equation 5.5.

$$S_{effective} = 2\pi\left(\frac{R_1 + R_2}{2}\right)t = 2.7\pi R_1 t \tag{5.5}$$

The effective area is taken to occur directly above the center of the electromagnet coil and may be simplified as shown on the right hand side the equation assuming $R_2 = 1.7R_1$. The reluctance of the armature path element is therefore given by Equation 5.6,

$$R_a = \frac{1}{2.7\pi\mu_a t} \tag{5.6}$$

where μ_a is the permeability of the armature. It is interesting to note that the reluctance of the armature is not dependent upon the geometric scale of the electromagnet but only on t. Recalling the definition of k, the ratio of the armature reluctance to the air gap reluctance, defined here as z, may be expressed by Equation 5.7,

$$z \equiv \frac{R_a}{R_g} = \frac{R_1}{5.4\mu_r kt} \tag{5.7}$$

where μ_r is the relative permeability of the armature. The characteristic ratio, z, is seen to be proportional to the scale of the electromagnet, R_1, and inversely proportional to the system ratio, k, the armature thickness, t, and the relative permeability of the armature material. This indicates that for a well-designed system where k is constant, it is expected that the system performance is dependent upon the armature thickness, which scales with the size of the electromagnet. If k is kept constant in the design but the electromagnet size is increased, t must be increased by the same factor to preserve the ratio z. The use of a magnetic rubber with a higher relative permeability may offset this increase, but experimental magnetization data of the rubber show that there is not much flexibility in

μ_r. For example, if a reluctance ratio of unity is chosen for a system involving the 6" electromagnet with $k = 0.1$ and $\mu_r = 2$, then the armature thickness must be 35mm. If the air gap is doubled and k is preserved, then the armature thickness must be 70mm. Such thicknesses may not be practical in a real large-scale system, as the rubber armature may be difficult to maneuver due to its thickness and weight. It is expected from the theoretical considerations of the armature reluctance ratio that the armature will present a very significant restriction to the development of useful flux, and therefore clamping pressure, in the magnetic clamping device. Further inspection of the effect of the armature process parameters is carried out with the FEA model in a later section, which leads to recommendations of appropriate values of z for effective deployment of the device.

Theoretical considerations of magnetic flux paths in the clamping system, consisting of a round electromagnet and magnetic rubber armature, lead to the specification of two characteristic design proportions, k and z, which are important for efficient application of the system to particular composite part thicknesses. Flux leakage phenomena were discussed in this section and a recommendation of $k < 0.1$ was made to preserve the development of useful flux and minimize saturation of the electromagnet back-iron. In addition, the parameters of the rubber armature were discussed and z was proposed as a useful system design parameter. Further analysis with the FEA model follows in a later section to optimize the value of z. In conclusion, the effectiveness of the clamping system was proposed to be dependent upon the design proportions. These proportions are functions of the thickness of the part to be consolidated and indicate that

the electromagnet and armature must scale appropriately with the part thickness to preserve its utility.

5.5 Pressure Scaling and Design Parameter Optimization

In the previous section it was proposed that the characteristic parameters *k* and *z* can be used to generalize the development of useful magnetic flux in the clamping device. In this section, it is shown that these two parameters predict the pressure developed by the device as a function of the current intensity, NI/R_1, of the electromagnet. This relationship is independent of the air gap in the system and depends only upon *k* and *z*. In addition, both parameters are investigated in terms of real-world application considerations and device pressure optimization.

5.5.1 System Pressure Scaling Theory

The performance of the clamping system in terms of pressure exerted on the armature scales with a parameter defined here as current intensity, which is the ratio of the magnetomotive force of the electromagnet, *NI*, to a characteristic system length. For convenience this characteristic length is chosen to be R_1. The characteristic ratios also are based on it. Recalling the magnetic circuit analogy, the total reluctance of a system with constant *k* and *z* may be shown to be proportional to the reluctance of the useful air gaps. This is true because a constant *k* and *z* require the reluctance of the leakage paths and the armature element to be proportional to the reluctance of the air gaps, respectively. The total flux through the system is given by $\Phi = NI/R$, where *R* is the total reluctance. Equation 5.4 gives the reluctance of the air gap. The flux therefore follows the Equation 5.8.

$$\Phi \propto NI\frac{\mu_0 \pi R_1^2}{2g} = NI\frac{\mu_0 \pi R_1}{2k} \tag{5.8}$$

The B-field in the air gap is found by dividing Φ by the cross sectional area of the electromagnet core, πR_1^2, which results in Equation 5.9.

$$B \propto \frac{NI}{R_1} \tag{5.9}$$

Note that the permeability term and k factors are omitted because they are constant. Given that the pressure exerted on the armature scales with the square of the B-field, the pressure also is a direct function of the current intensity, NI/R_1.

5.5.2 Model Validation of Pressure Scaling

The FEA model was used to validate the claim that the characteristic parameters k and z uniquely define a function relating the clamping system pressure to the applied current intensity. The FEA model of the 6" round electromagnet was modified to simulate a system with an electromagnet of the same proportions that may be scaled as a function of R_1. The finite-element mesh density also retained the original proportions. The inputs to the model are the air gap, g, the characteristic ratios k and z, the relative permeability factor of the armature, μ_r, the magnetization model of the armature, and the applied current intensity. The parameters g, k, z, and μ_r completely define the geometry of the system including the thickness of the armature. The pressure exerted by the system, p, is defined as the total calculated force over the total area of the face of the electromagnet, πR_3^2.

The model was solved at k values of 0.05, 0.1, and 0.2, with z and μ_r both fixed at values of 2 and using the experimentally-determined BH model of the ϕ = 30% rubber.

The simplification of $\mu_r = 2$ is made here initially but is investigated further in the next section. The model geometry was defined with two values of g: 3mm and 10mm. Six values of current intensity were applied between 50 and 2000 A-turns/mm. It is helpful to note for reference that the 1" and 6" electromagnets used in the force experiments are rated to operate at 60 and 80 A-turns/mm, respectively. The highest current intensity applied experimentally is 400 A-turns/mm. As such, the maximum applied current intensity of 2000 A-turns/mm applied in the model represents an extremely large amount of electrical power. Table 5.3 shows the results of the calculations with the proportional FEA model.

Table 5.3 Pressure scaling at two air gaps with proportional FEA model

	g = 3mm			g = 10mm		
k =	0.05	0.1	0.2	0.05	0.1	0.2
NI/R =	Pressure [Pa]					
50	4712.9	2340.7	815.4	4712.7	2340.6	815.4
100	17719.4	9008.0	3184.2	17719.0	9008.2	3184.3
200	58095.7	31410.5	11572.9	58094.4	31410.0	11573.3
500	137112.5	86335.5	37412.6	137109.5	86332.1	37414.7
1000	198317.8	128530.6	58439.6	198322.1	128522.0	58439.9
2000	294685.6	191737.1	89861.2	294694.2	191737.1	89864.7

The results of the 3mm gap calculations are shown on the left hand side of the table and the 10mm gap calculations are shown on the right hand side. The two sections are almost exactly equal, which shows that the pressure vs. current intensity curve may be considered to be independent of the magnitude of the air gap and depends only on the characteristic ratios of the clamping system. Note that because the core radius of the electromagnet is defined by g and k, the columns each refer to different sized electromagnets. For example, the case of the 10mm air gap case with $k = 0.05$ refers to a magnet with core radius of 200mm and a total diameter of about 800mm. While the

system pressure is indeed a unique function of the current intensity for a given set of characteristic ratios, the dimensions of the actual system may not be realizable at all combinations of such ratios.

The preceding theoretical considerations and FEA model experimentation demonstrate that the performance of a magnetic clamping system in terms of overall exerted pressure is a function of the applied current intensity that is completely described by two characteristic ratios: k and z. The ratio k is related the amount of flux leakage inherent in a system based upon the relationship of the air gap to the length scale of the electromagnet. Note that it is assumed that any electromagnet chosen for use in the device is well-designed; that is, its dimensions retain the same proportional relationships regardless of its scale. The ratio z is based upon the relationship of the armature reluctance to the air gap reluctance and is dependent upon the thickness of the armature and the permeability of the armature material. Thus equipped, the FEA model may be used to generate operating curves that allow a designer to specify the characteristic ratios of the device based upon pressure and current intensity requirements. In addition, inspection of the operating curves shows the limits of the system and the realistic operating conditions.

5.5.3 Optimization of Characteristic Ratio k

The proportional FEA model was solved at a range of seven k values from 0.01 to 0.5 with the value of z fixed at 2. Again, the BH curve of the 30% filled rubber was used with a relative permeability value of 2. A value of 3mm was used for g, but the discussion of the previous section shows that this choice is irrelevant for the calculation of p vs. NI/R_1 performance curves. The applied current intensity ranged from 50 to 2000

A-turns/mm. The purpose of the experiment is to demonstrate the isolated effect of k on the system performance curves. The armature ratio z is developed later.

Figure 5.34 shows the effect of the ratio k on the system performance curves. The curves are generated with six operating points but are smoothed for clarity. All seven curves show trends similar to those observed in the force experiments. In all cases the pressure demonstrates a rapid increase up to 100 A-turns/mm, a slowing increase up to about 500 A-turns/mm, and a linear increase above 500 A-turns/mm. The lower values of k result in better system performance due to lower flux leakage ratios.

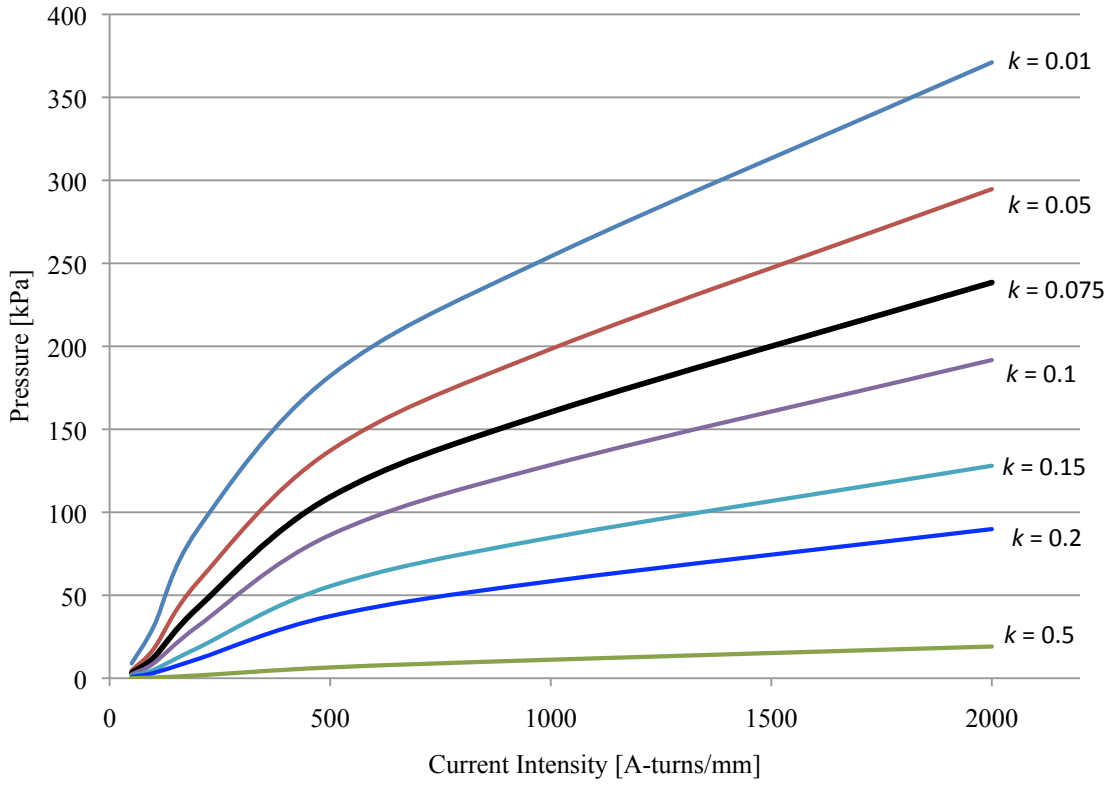

Figure 5.34 Device performance curves as a function of k

Table 5.4 shows, for an air gap of 3mm, the necessary device parameters to operate with the k values shown in Figure 5.34.

Table 5.4 Device parameters with g = 3mm and variable ratio k

Constants:	**g = 3mm**	mu_r = 2	z = 2				
k =	0.01	0.05	0.075	0.1	0.15	0.2	0.5
D [mm] =	1216.2	243.24	162.16	121.62	81.08	60.81	24.324
R1 [mm] =	300	60	40	30	20	15	6
t [mm] =	1388.9	55.6	24.7	13.9	6.17	3.47	0.556

A gap of 3mm represents the minimum part thickness that has any practical application for composite laminates. Due to the relationship of g and R_1, smaller values of k require large diameter electromagnets to maintain the low flux leakage. The upper curve, referring to k = 0.01, may be considered the lower bound on the value k. In order to consolidate a 3mm thick part with such a k value, an electromagnet greater than a meter in diameter is required and an armature of a 1.4 meter thickness is required to maintain z. For thicker parts, extremely large electromagnets would be required. The armature thickness is also unacceptable. Large values of k, such as the k = 0.5 curve, show that the clamping system is only able to develop clamping pressures on the order of 20 kPa even at very high applied current intensities. Using a pressure of 100 kPa as a guideline, the maximum consolidation pressure in the VARTM process, inspection of the upper and lower bounds of k shows that values of k between 0.05 and 0.1 are able to generate useful levels of pressure at realistic applied current intensities. Values of k below 0.05 are not considered, as they require the components of the device to be much too large. Systems with values of k over 0.1 are not able to develop pressures of 100 kPa at reasonable current intensities. The k = 0.15 curve reaches 100 kPa only when the curve is well into its final linear regime, indicating that it is an unfavorable operating parameter. It is therefore recommended that a value of k = 0.075 be used as a guideline in design on

a magnetic clamping system because it allows the system to create useful amount of pressure with reasonably sized components and current intensity requirements.

5.5.4 Optimization of Armature Parameters

The purpose of this section is to explain the effect of the armature parameters on the utility of the clamping system. It was previously hypothesized that the thickness and relative permeability of the armature must scale with Equation 5.7 in order to prevent significant restriction of useful magnetic flux in the system. The hypothesis is tested using the FEA model at a range of armature parameters at three acceptable k values: 0.05, 0.075, and 0.1. Inspection of the resulting data indicates that the critical design parameter z is better defined as the ratio of the armature thickness, t, to the electromagnet core radius, R_1. It was also found that the clamping pressure of the system is linearly proportional to the volumetric iron loading fraction of the rubber, ϕ. The FEA model was used to characterize the system performance at the optimum gap-to-electromagnet ratio, k = 0.075, at a range of z values. The results may be used as design guidelines in order to optimize the armature thickness and loading fraction based upon desired clamping pressure and constraints upon the armature parameters.

The FEA model was solved with g = 3mm at a range of armature thickness and filler fractions for values of k = 0.1, 0.075, and 0.05 at applied current intensities of 625, 450, and 350 A-turns/mm, respectively. These particular values of current intensity were chosen because they cause the pressure of the system to be approximately 100 kPa, as observed in Figure 5.34, when the ideal armature thickness, t_0, is given by Equation 5.10.

$$t_0 = \frac{g}{21.6k^2} \tag{5.10}$$

Equation 5.10 defines the ideal armature thickness using Equation 5.7 with values z and μ_r both equal to 2. The model was solved with five armature thicknesses of $t = 0.1t_0$, $0.5t_0$, t_0, $2t_0$, and $10t_0$. The three rubber materials models for $\phi = 15\%$, 23%, and 30% were also used. The results of the calculations are shown in tabular form in Table 5.5.

Table 5.5 Pressure in kPa of three k values and a range of t and ϕ

	$0.1t_0$	$0.5t_0$	t_0	$2t_0$	$10t_0$	
t [mm] =	5.5	27.5	55	110	550	k = 0.05
phi = 30%	27.8	88.0	109.4	115.0	115.4	**R1 = 60mm**
phi = 23%	22.4	69.6	86.8	91.6	92.0	NI/R1 = 350
phi = 15%	14.6	42.2	51.9	54.9	55.2	A-t/mm
t [mm] =	2.4	12	24	48	240	k = 0.075
phi = 30%	19.9	71.9	101.3	116.2	118.8	**R1 = 40mm**
phi = 23%	16.2	57.7	81.3	93.8	96.2	NI/R1 = 450
phi = 15%	10.8	36.7	50.5	58.0	59.7	A-t/mm
t [mm] =	1.36	6.8	13.6	27.2	136	k = 0.01
phi = 30%	16.5	64.4	97.8	122.0	129.2	**R1 = 30mm**
phi = 23%	13.5	52.1	79.0	99.1	105.6	NI/R1 = 625
phi = 15%	9.1	34.0	50.4	62.7	67.1	A-t/mm

Table 5.5 shows the k value, corresponding R_1 value, and current intensity of the three cases on the right hand side of the table. For each case the resulting pressure, in kPa, of fifteen combinations of armature parameters is shown. The effect of ϕ is seen to be nearly linear in all cases. The pressures obtained with $\phi = 15\%$ are half of those obtained with $\phi = 30\%$. As such, it is shown with the model that for k between 0.05 and 0.1, the system pressure is linearly dependent upon ϕ. This has important implications on the design of the armature for a clamping system. If a system generates some pressure, p_0, with an armature of loading ϕ_0, a change in the loading will change the pressure as shown in Equation 5.11,

$$p_1 = p_0 \frac{\phi_1}{\phi_0} \tag{5.11}$$

where p_1 is the new system pressure and ϕ_1 is the new armature loading.

Table 5.5 also shows the significance of t on the clamping pressure. For the k = 0.05 case, there is only a 5% increase in pressure from t_0 to $2t_0$ and a 0.4% increase from $2t_0$ to 10 t_0. With the k = 0.075 and k = 0.1 cases the percent increases are higher. However, it is seen that in all three cases the pressure does not increase significantly for $t > R_1$. For example, in the k = 0.1 case, where R_1 = 30mm, there is a 25% increase in pressure from t = 13.6mm to 27.2mm but only a 5% increase from t = 27.2mm to 136mm. The data demonstrates that the electromagnet core radius, R_1, is a good indicator of system performance. As such, the armature parameter z is redefined accordingly as:

$$z \equiv \frac{t}{R_1} \tag{5.12}$$

where a value of z = 1 is an optimum upper bound on the armature thickness. Equation 5.12 effectively replaces the definition of z given in Equation 5.7. The validity of the Equation 5.12 definition for z may be seen qualitatively by inspection of a pair of flux line images generated with the FEA model in Figure 5.35 with k = 0.075, NI/R_1 = 250, and ϕ = 30%. The image on the left with z = 1 shows how the armature routes a large amount of the flux into the electromagnet through the useful paths. On the right, the armature with half the thickness displays some flux lines that are missed. The difference between the flux paths observed in Figure 5.35, a low permeability armature, and those seen in Figure 5.29, a high permeability armature, demonstrate that the reluctance element approximations used in the formulation of Equation 5.7 are not valid.

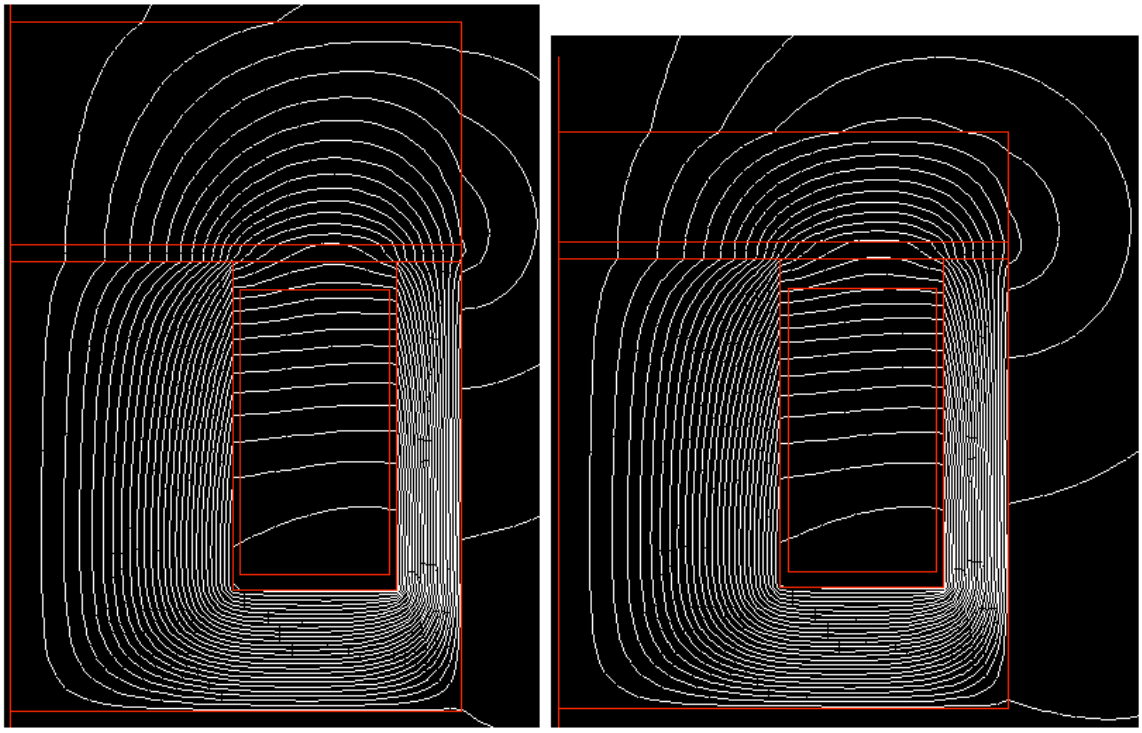

Figure 5.35 Flux comparison of system ($k = 0.075$) with $z = 1$ (left) and $z = 0.5$ (right)

The FEA model was used to generate performance curves using the new definition of z according to Equation 5.12. A gap ratio value of $k = 0.075$ was used with six values of the armature ratio, z, ranging from 0.1 to 1.25. The BH model of $\phi = 30\%$ rubber was used. Six current intensities from 100 to 1000 A-turns/mm were applied. An air gap of $g = 3$mm was chosen for use in the model; however, the resulting pressures are independent of g because z and k are fixed. Figure 5.36 shows the results of the experiment. The same trends from Figure 5.34 are apparent: a steep linear regime at lower currents, which transitions to a regime with a slope that is shallower. For values of z above unity there is little increase in the system clamping pressure. Below values of unity, the effect of z on the pressure is approximately a logarithmic trend, although a logarithmic regression does not provide an accurate enough fit for it to be modeled as such.

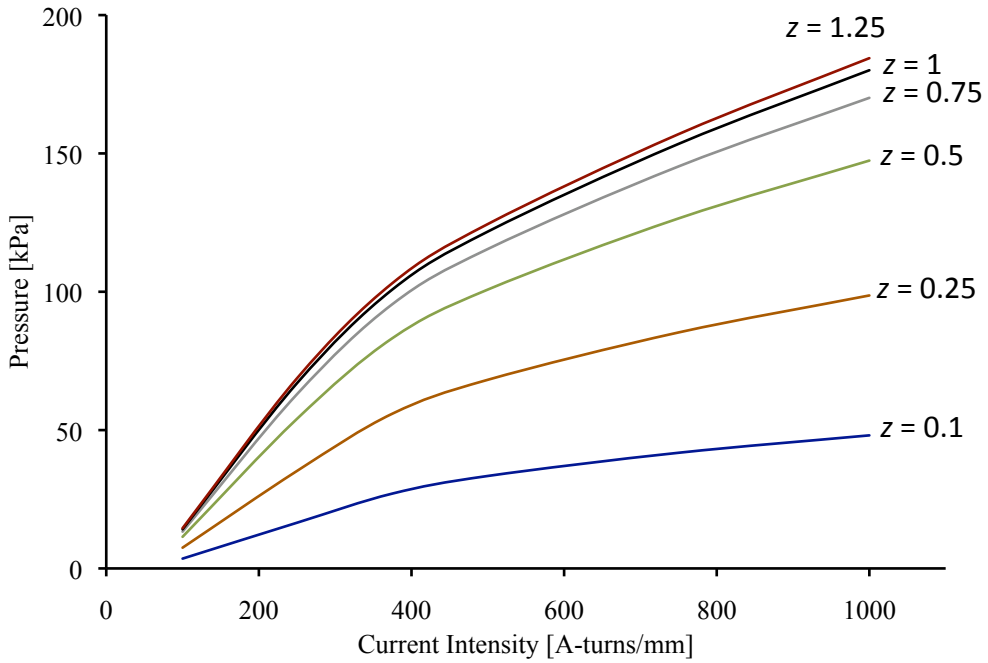

Figure 5.36 Performance curves for $k = 0.075$ at a range of z values

The curves in Figure 5.36 show that there is good reason to consider the use of an armature with ratio $z < 1$. For example, the $z = 0.75$ shows that a 25% reduction in armature thickness from $z = 1$ only causes a 5% reduction in system pressure. Table 5.6 shows the results of the model calculations from Figure 5.35 at each applied current intensity as a fraction of the pressure calculated at $z = 1$. The results show that the pressure fractions are approximately independent of the current intensity.

Table 5.6 Pressure normalized at $z = 1$ for $k = 0.075$

NI/R1	z = 0.1	z = 0.25	z = 0.5	z = 0.75	z = 1	z = 1.25
100	0.250	0.530	0.808	0.940	1.000	1.028
250	0.247	0.526	0.808	0.941	1.000	1.026
375	0.268	0.555	0.825	0.947	1.000	1.023
500	0.275	0.560	0.828	0.948	1.000	1.022
750	0.272	0.556	0.824	0.947	1.000	1.023
1000	0.267	0.548	0.819	0.945	1.000	1.024

Further model calculations with k values of 0.05 and 0.1 yielded the same results as shown in Table 5.6 with very little variation. The pressure fractions are therefore considered independent of k within the range of interest. A system designed with any air gap and a gap ratio k between 0.1 and 0.05 can be expected to yield clamping pressures dependent on the armature thickness as shown in Table 5.6.

Finally, the model was solved with $z = 1$ at a range of k values in order to determine if the effect of k on the system pressure is independent of the current intensity as is the case with z. The calculated results are also the system performance curves using the updated definition of z. The $\phi = 30\%$ model was used and five values of k between 0.05 and 0.1. Figure 5.37 shows the results of the model calculations.

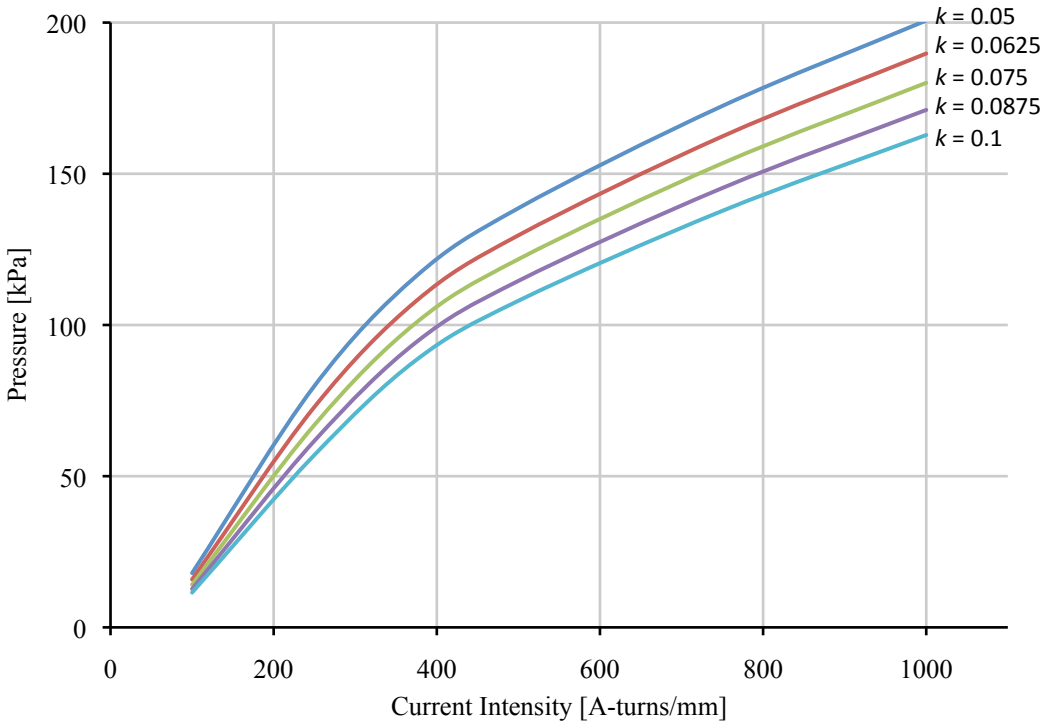

Figure 5.37 System performance curves with $z = 1$ at a range of k values

The results are similar to those in Figure 5.34, as would be expected, however it is important to note that these curves represent the performance of a generalized system with $z = 1$ at some gap ratio k. Inspection of the actual pressure results and their normalized relationships lead to the conclusion that the effect of k on the system pressure is not independent of the current intensity. This is also evident by comparison of Figure 5.37 to Figure 5.36. The former shows parallel, offset performance curves while the latter shows curves with very different final slopes.

5.5.5 Device Design Summary and Remarks on Limitations

This section demonstrated from a theoretical standpoint and using the FEA model that the magnetic clamping device may be designed to yield a desired clamping pressure by the correct application of characteristic system ratios. First, it was shown that the clamping pressure and current intensity scale together, provided the electromagnet geometry, armature ratio, and gap ratio are fixed. Second, the gap ratio k was shown to be a critical indicator of system performance due to flux leakage. Values of k between 0.05 and 0.1 were shown to yield acceptable clamping pressures with realistic current intensities and electromagnet sizes. The gap ratio depends upon the applied current intensity and therefore a set of curves, such as those in Figure 5.37, must be used to predict device performance. Third, an armature thickness ratio, z, was developed to determine the proper design proportions of the armature. The performance of a clamping device increases with the armature thickness up to a value of $z = 1$, after which additional armature thickness has little to no marginal benefit. The effect of z was shown to be effectively independent of the current intensity, unlike k. Finally, it was found that the clamping pressure of the device is directly proportional to the volumetric magnetic filler

loading fraction. This proportionality is independent of other device parameters. Figure 5.38 displays the design process based upon the characteristic system ratios in a flowchart format.

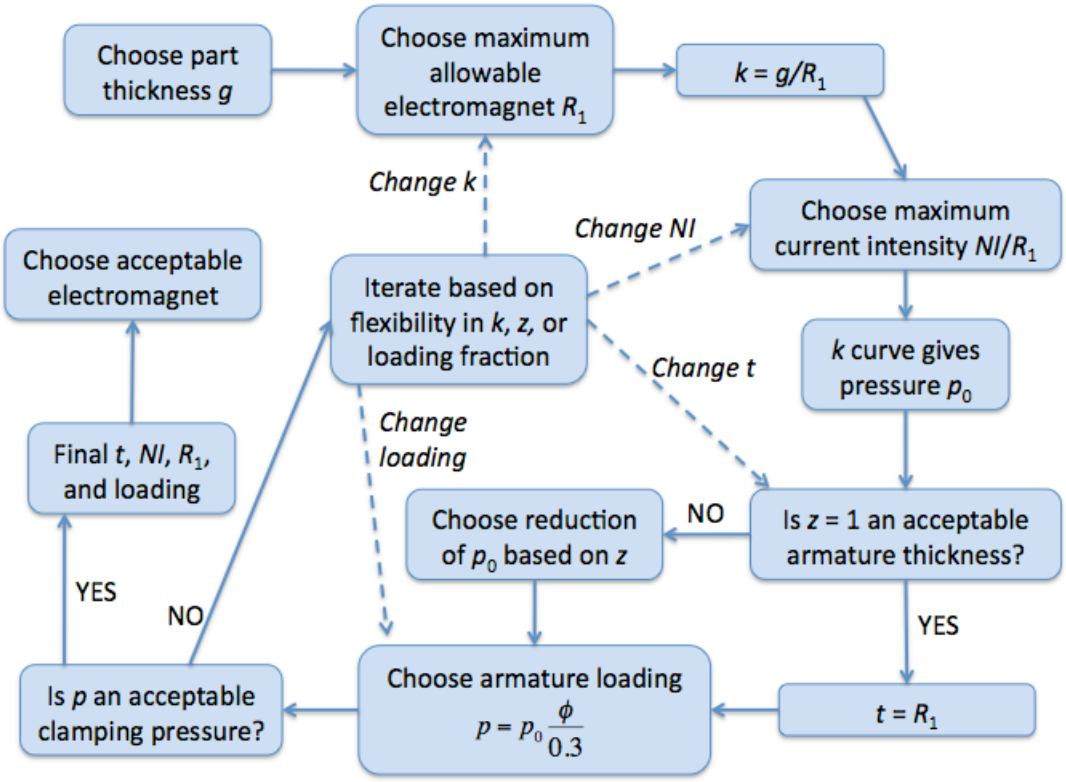

Figure 5.38 Clamping system design flowchart

Figure 5.38 shows the proposed design method for the clamping device. The device may be designed to achieve a required level of clamping pressure through a systematic choice of characteristic ratios. Initially, it is assumed that the device is required to consolidate a composite part of some thickness, which acts as the system air gap, g. The performance curves of Figure 5.37 are then consulted to determine an optimum value of $k = g/R_1$. The curves show the maximum pressure the device can generate for a given value of k. Ideally, the maximum feasible electromagnet size would

be used, resulting in the lowest possible value of k. A lower value of k also reduces the necessary applied current intensity, which has important implications on the power and cooling requirements of the final device. A current intensity is then chosen and the corresponding k curve gives an initial system clamping pressure, p_0. Next, an armature thickness is chosen using the reduction factors given in Table 5.6. If the armature thickness, t, must be less than R_1, the reduction factor is multiplied by p_0 to find the reduced clamping pressure. Finally, if an armature loaded at less than 30% is used, Equation 5.11 gives the resulting pressure reduction. If the clamping pressure is unacceptable, iteration must take place based upon one of the critical factors. After the design ratios and current intensity are chosen for an acceptable clamping pressure, the actual size and magnetomotive force, NI, of the required electromagnet are easily calculated as well as the actual thickness of the armature. These requirements may be compared with commercially available electromagnets or serve as the basis for a custom electromagnet design. The design process may be approached from a different starting point if a parameter other than the part thickness is the controlling factor.

The design method as described also provides useful insight into the practical limitations of the magnetic clamping device in terms of applied power. As previously mentioned, commercially available electromagnets, such as those used in the force experiments, are usually designed for steady-state operation at current intensities of approximately 80 A-turns/mm. Figure 5.37 shows that current intensities of at least 300 A-turns/mm are necessary to reach a useful clamping pressure of 100 kPa. Cooling of the electromagnets is therefore a requirement for continuous operation of any magnetic clamping device. Current intensities of up to 250 A-turns/mm were continuously applied

experimentally with a water-circulated coldplate via conduction on the bottom of the electromagnets. Higher applications of power may require more advanced cooling techniques such as water passages inside the electromagnet or coils. In addition, the performance curves in Figure 5.37 reach their final linear regimes around 400 A-turns/mm due to magnetic saturation of the device components. The marginal return in clamping pressure for increased power and cooling beyond this point is poor, which indicates that 100 kPa may indeed be the maximum realistic pressure for a device utilizing a low-permeability armature such as magnetic rubber. In the next section, the possibility of using a high-permeability armature such as steel is discussed briefly.

The restrictions placed upon the gap ratio k also have important ramifications in terms of the size of the device components required to achieve useful clamping pressures. The ratio k must be kept below 0.1 in order to prevent flux leakage from dominating the device. Given that the diameter of a well-designed electromagnet is four times its core radius, R_1, an electromagnet must be at least 40 times the thickness of the part to be consolidated. For example, a 3mm part requires a 120mm diameter electromagnet while a 25mm part requires an electromagnet diameter of a meter. Electromagnets of this size are commercially available but would cause the device to be extremely large and inflexible due to weight and power requirements. For the $z = 1$ ratio to be preserved the armature also would have to be around 250mm thick. Furthermore, the coil space on the face of an electromagnet causes a "dead spot" in the pressure distribution. For large electromagnets this dead spot may be large enough to be problematic in the consolidation process. The pressure distribution is discussed at greater length in a later section.

5.6 Electromagnet Arrays

The objective of the magnetic clamping device is to consolidate large-scale composite parts. In the previous section, it was shown that electromagnets on the order of a tenth of a meter to a meter are capable of providing up to 100 kPa of consolidation pressure. A large-scale device must incorporate arrays of such electromagnets. Tests were performed with arrays of 1" round electromagnets to observe interference effects. The results of the experiments are discussed as they pertain to the design of a large-scale device. The possibility of employing electromagnets of different shapes also is discussed.

5.6.1 Electromagnet Array Experimental Results

Attractive forces were measured for two array configurations of the 1" electromagnets: four in a square array and three in a hexagonal array. Four spacing values were used for each configuration, where the spacing value refers to the distance between the centers of two adjacent electromagnets. In both cases, the minimum spacing value was 25.4mm with the electromagnets touching. The electromagnets were wired in parallel and energized up to 0.75 A. Only the thick 30% loaded rubber sample was used. Two air gaps, 7mm and 9mm, were used in the experiments. The results of the experiments are displayed in Table 5.7.

Table 5.7 1” electromagnet array data

Hexagonal Array, Force [N]								
Air gap	7mm				9mm			
Spacing [mm]	25.4	33.0	44.0	66.0	25.4	33.0	44.0	66.0
Current [A]								
0.1	0.0249	0.031	0.0374	0.029	0.0185	0.016	0.022	0.014
0.2	0.0973	0.106	0.121	0.112	0.0567	0.054	0.064	0.055
0.3	0.2064	0.222	0.246	0.237	0.112	0.115	0.127	0.123
0.4	0.349	0.38	0.408	0.406	0.189	0.193	0.21	0.207
0.5	0.52	0.57	0.604	0.617	0.277	0.284	0.314	0.312
0.75	0.985	1.05	1.13	1.16	0.515	0.521	0.573	0.588
Square Array, Force [N]								
Air gap	7mm				9mm			
Spacing [mm]	25.4	26.9	35.9	53.9	25.4	26.9	35.9	53.9
Current [A]								
0.1	0.0199	0.028	0.032	0.0268	0.012	0.011	0.0125	0.015
0.2	0.0965	0.108	0.123	0.128	0.048	0.0501	0.059	0.064
0.3	0.212	0.238	0.263	0.273	0.11	0.113	0.122	0.135
0.4	0.376	0.407	0.451	0.477	0.193	0.2	0.218	0.235
0.5	0.58	0.625	0.68	0.725	0.298	0.304	0.323	0.351
0.75	1.14	1.19	1.32	1.4	0.575	0.579	0.636	0.695

The results in the table show some interesting trends with respect to the spacing value. For the square configuration the force increases monotonically with spacing at all applied current and gap values, except for the 7mm case with maximum spacing. However, for the hexagonal configuration the force increases with spacing for higher current values but shows a tendency to decrease from the 44mm and 66mm spacing values at lower applied currents. Qualitatively at least, it is apparent that electromagnet spacing has a significant effect on the overall force exerted by the clamping system. There also appears to be some dependency on whether the array is in a square or hexagonal configuration. It must be noted, however, that the gap ratio (k) values are 1.1 and 1.4 for the 7mm and 9mm air gaps. Referring to Figure 5.34, these gap ratios are

expected to yield extremely poor clamping pressures and are far from the sort of *k* values with which an actual magnetic clamping device would be designed.

Figure 5.39 shows the force per electromagnet normalized by the force results found with a single electromagnet at an applied current of 0.75A and an air gap of 7mm. These parameters were chosen because they resulted in the highest forces. The observed forces were divided by the number of electromagnets in the array and then by the force of the single electromagnet at the same experimental parameters, 0.495 N.

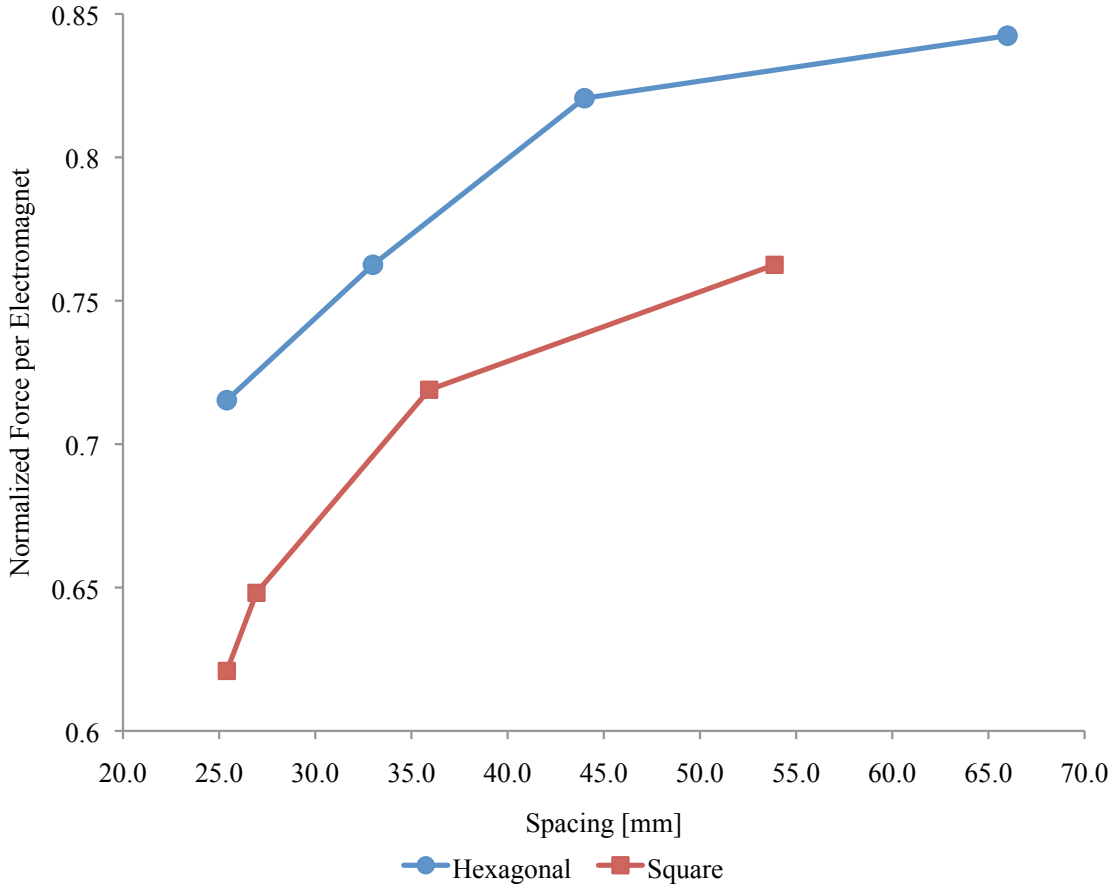

Figure 5.39 Normalized force per electromagnet vs. hex and square array spacing

The curves in the figure show that the normalized force is as low as 0.62 for the square array and 0.72 for the hexagonal array. Electromagnets in array configurations demonstrate interference effects causing a significant loss in system efficiency. Recalling

Figure 5.30, flux images of the clamping system with a large air gap, it is seen that a significant amount of flux exists outside the outer radius of the electromagnet when the air gap is large. In contrast, Figure 5.29 shows that relatively little flux exists in the outer region when the air gap is small. It is reasonable, therefore, to conclude that the observed interference effect is due to the interference of the outer flux of the individual electromagnets with each other. The curves in Figure 5.38 also show a decrease in interference with increased spacing, which supports this conclusion.

The interference phenomenon reiterates the importance of the *k* ratio in the design of a clamping device. Proportionally large air gaps, such as those used in the experiment, cause the device to route magnetic flux inefficiently. It was previously seen that this occurs due to flux leakage across the pole and core of the electromagnet. The array data show the problem would be exacerbated by an array configuration. The already low clamping pressures would be further reduced by as much as 40%. However, inspection of the flux paths typical in a low-air-gap system, such as Figure 5.29, indicates that this interference is likely not a problem with array clamping systems of appropriate *k* values. The outer flux is not a dominant feature so interference will not occur to the same degree. It is therefore concluded that the clamping system may be implemented in an array configuration without significant interference between the individual electromagnets provided an acceptable *k* value is used. As such, no further design step needs to be taken when implementing a chosen electromagnet into an array configuration, provided the electromagnets are rectangular and are positioned closely. A discussion of rectangular electromagnets is given in the next section.

5.6.2 Remarks Regarding Arrays of Non-Round Electromagnets

Up to this point only round, flat-faced electromagnets have been discussed for use in the magnetic clamping system. For research purposes, round electromagnets are advantageous as they may be modeled from a 2D, axisymmetric perspective. They are also very common and commercially available. They may not, however, be the ideal candidates for a system utilizing a large array of electromagnets. The primary reason is that an array of round electromagnets necessarily includes spaces between them. Square and rectangular flat-faced electromagnets are very similar to round electromagnets and may be used instead. Arrays of square electromagnets may be assembled with no spaces between them, thereby removing the gaps present with round electromagnets. Rectangular electromagnets may also be used – it is possible to fabricate long electromagnets that are the width of the part being manufactured. It is also possible to fabricate a ferromagnetic mold made of low-carbon steel with coil passages machined at the appropriate locations and depths and coil packs placed in them.

It is helpful here to mention that design of a clamping system with square or rectangular electromagnets is not significantly different than one utilizing round electromagnets. As with round electromagnets, square electromagnets generate tractive forces through the flux coupling of highly permeable back-iron and a magnetic armature. Flux leakage and saturation dictate that air gap and armature geometric ratios are still critical design parameters. The physics behind the system are the same and similar values of k and z will be required to design an efficient system. Likewise, it is also expected that the scaling relationship between clamping pressure and current intensity is preserved and the same design procedure is applicable.

5.7 Steel Armature Experiments and Discussion

Force experiments were performed with mild steel in place of the magnetic rubber samples with the 6" round electromagnet. Five steel samples of the same mass of iron as the five rubber samples were used to compare the effect of the same amount of iron dispersed through the rubber versus a solid iron piece. Two additional iron samples were used of the same thicknesses of the rubber samples to provide an idea of the upper limit of the attractive forces possible with the device. The same four air gaps, 7mm, 9mm, 16mm, and 25mm were used with applied currents up to 19.2A or until the force reached 500 N.

It was postulated that the total mass of iron may be used as a means to simplify the characterization of armatures of various thicknesses and loading percentages. In other words, the purpose of the experiments was to determine if a rubber armature of thickness t_{rubber} and volumetric loading ϕ yields the same attractive force as a same-mass steel armature with thickness $t_{steel} = \phi\, t_{rubber}$. The experimental results show, however, that this approximation is not valid. In the case of the thinnest steel armature, 0.94mm, used to approximate the iron in the thin 15% loaded rubber sample, the steel yielded slightly more force up to a current of 10A but substantially less above 10A. The final trend was divergent, indicating that the rubber armature outperformed the steel. In the case of the thickest same-mass armature, 3.05mm, the steel armature yielded at least 3 times the force over the entire current range. It is concluded that the same-mass approximation is not a valid or useful simplification in the design of a magnetic clamping device.

The two 6.5mm and 10.2mm thick steel samples were used to determine if the forces developed by rubber armatures of the same thickness were directly proportional to

those made of steel. This hypothesis seems logical in light of the findings, discussed in section 5.5, that the pressure of a clamping device is directly proportional to the loading percentage of the armature. In the case of the 10.2mm steel sample, the steel yielded approximately twice the force of the 10.7mm thick, 30% loaded rubber armature at the highest air gap of 25mm. At the lowest air gap of 7mm, however, the steel yielded 3 times the force at low applied currents (1.8A) and 4 times the force at higher applied currents (5.4A). Higher currents were not experimentally possible because the force exceeded 500N. These findings demonstrate that the hypothesis shows some merit but is not accurate enough to be adopted as a design guideline. The 500N capacity of the load cell also limited the utility of the experiment because higher current intensities could not be applied.

Previous analysis of flux patterns in an electromagnet and armature device has demonstrated that the effects of the two armature parameters, t and ϕ, are not independent. It is therefore not surprising that the attempt to directly scale the force of the device with the same-mass iron assumption was not successful. Nonlinearities in the magnetization models of both steel and magnetic rubber and in the flux paths inherent in the clamping system cause the two parameters to be necessarily confounded. However, the data are helpful in determining the possibility of replacing the rubber armature with a thin layer of steel. The beauty of a rubber armature in a consolidation device is its flexibility and ability to conform to the curvature of a composite part. Stacked layers of very thin steel, such as shim stock, were considered as a possible alternative to magnetic rubber. Thin layers of steel are also flexible and may be able to conform to some levels of curvature. The results show that a steel armature at least 3mm thick can yield marginally

greater attractive forces than those observed with the rubber. This thickness corresponds to an armature ratio value of $z = 0.08$. Further experimentation and modeling are necessary, however, in order to determine if layered shim stock may be used to achieve acceptable clamping pressure levels and conformability.

5.8 Clamping Pressure Distribution

Finite-element modeling of the magnetic field behavior in the magnetic clamping device is used in this section to reveal the distribution of the magnetic forces that occur on the armature. Experiments utilizing a Gaussmeter showed that the model predictions of the field at the face of the electromagnet are accurate. The model may therefore be used to predict the axial B-field profile on the bottom face of the armature. The axial B-field in this location is directly related to the tractive stress exerted by the field on the armature and thusly the compressive stress exerted on the part beneath it. The FEA model is used to determine the effect of the critical process parameters k, z, and ϕ on the axial B-field along the face of the armature. It must be noted, however, that the actual compression experienced by the part is related to the structural behavior of both the part and the armature. However, analysis of the axial B-field provides a first-order approximation of the pressure profile generated by the device. A discussion the magnetic and structural issues that must be addressed to thoroughly simulate the consolidation of a composite part with the device is also included in this section.

5.8.1 Pressure Profile Modeling

Figure 5.26 shows that the axial B-field along the radius of the face of the electromagnet displays both significant maximum and minimum on either side of the coil space. The B-field over the middle of the electromagnet core is relatively flat. The same

trend is observed in the axial B-field profile along the radius of the bottom of the armature. Ideally, a clamping device will have a proportionally small maximum and minimum in order to create an even clamping pressure distribution on the part. The model was solved at a range of parameters and the axial B-field was normalized with respect to the B-field at the center of the electromagnet to observe the effect of the parameters on the relative magnitudes of the maxima and minima.

The process parameters shown in Table 5.5, excluding the highest and lowest z values ($t = 0.1t_0$ and $t = 10t_0$), were chosen for the analysis of the B-field profile. The normalized B-field was recorded against the normalized radius, r, where a value of $r = 1$ refers to the outer radius, R_3, of the electromagnet. In all cases the maximum B-field was observed at $r = 0.46$ and the minimum was observed at $r = 0.88$. The maxima and minima locations are slightly offset from the inner and outer edges of the coil space, respectively. Table 5.8 shows the results of the modeling procedure.

Table 5.8 Normalized axial B-field maxima and minima for a range of parameters

	k = 0.05					
	phi = 30%			phi = 15%		
z =	0.46	0.92	1.83	0.46	0.92	1.83
Maxima	1.979	1.674	1.606	2.184	1.944	1.875
Minima	-1.172	-0.992	-0.938	-1.177	-1.042	-0.992
	k = 0.075					
	phi = 30%			phi = 15%		
z =	0.30	0.60	1.20	0.30	0.60	1.20
Maxima	1.885	1.597	1.472	1.960	1.748	1.637
Minima	-1.002	-0.852	-0.771	-0.974	-0.876	-0.807
	k = 0.01					
	phi = 30%			phi = 15%		
z =	0.23	0.45	0.91	0.23	0.45	0.91
Maxima	1.719	1.503	1.359	1.753	1.620	1.503
Minima	-0.844	-0.751	-0.672	-0.815	-0.759	-0.695

Three values of k were used, each with three values of z and two values of ϕ. Recall that the current intensities for k = 0.05, 0.075, and 0.1 are 350, 450, and 625 A-turns/mm, respectively. These current intensities cause the system pressure to be between 110 kPa and 120 kPa when z is approximately unity. Inspection of the values in the table shows that at all combinations of k and z the system with a higher value of ϕ has lower normalized maxima and minima values. Also, it is seen that for fixed values of ϕ and approximately fixed values of z, increasing k tends also to lower the normalized B-field values. For instance, the maximum value for the parameters k = 0.05, z = 0.46, and ϕ = 30% is 1.979 while for k = 0.1, z = 0.45, and ϕ = 30% it is 1.503. This trend is consistent for all values of z and ϕ. Finally, z is shown to be inversely proportional to the magnitude of the maxima and minima at all values of k and ϕ. Inspection of the data in the table shows that the parameters z and ϕ are inversely proportional to the magnitude of the B-field peaks while k is proportional to them.

Figure 5.40 shows the normalized axial B-field profile of the two cases with the highest and lowest magnitude peaks. The parameters corresponding to the two cases are shown in the figure legend. It is interesting to note that the case with the highest magnitude peak generated only 42 kPa while the system with the lowest magnitude peak generated 122 kPa. This demonstrates that reasonably flat pressure profiles are possible with certain combinations of optimum system parameters.

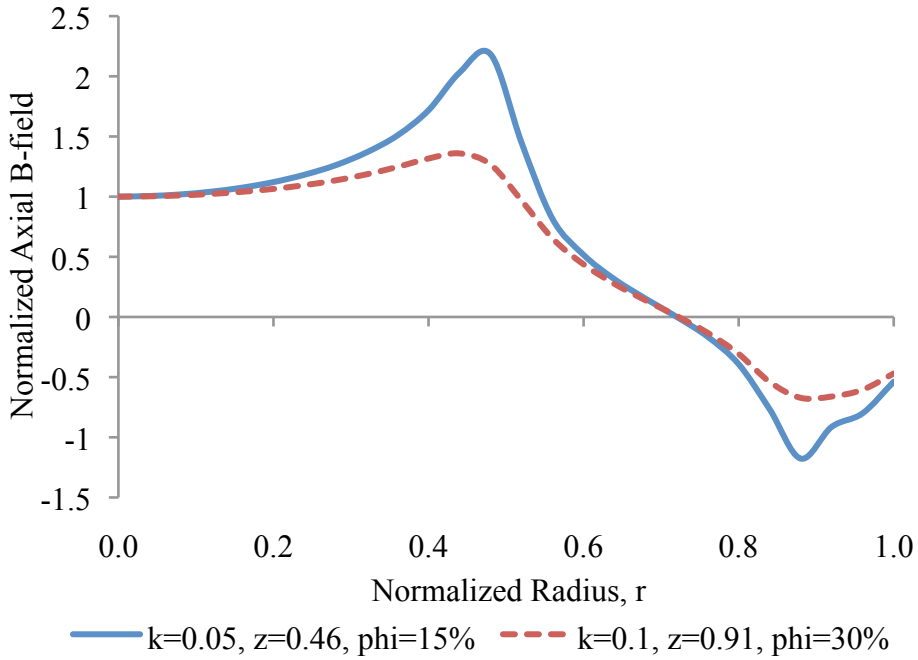

Figure 5.40 Highest and lowest normalized B-field peak cases from Table 5.9

The results of the B-field profile modeling give valuable insight into the pressure profiles expected from the clamping system. Increases in the system parameters z and ϕ are shown to result in more even B-field profiles. The system pressure also scales positively with these parameters. This is an encouraging result because it shows that a well-designed system in terms of clamping pressure is also well-designed in terms of pressure distribution. However, smaller k values, which increase the clamping pressure, tend to cause greater peaks in the pressure profile. As such, it is expected that the final design procedure for a magnetic clamping device must include an optimization between the high pressures achievable with low k values and the flatter pressure profiles from higher k values.

5.8.2 Structural Modeling Discussion

The previous discussion demonstrated that the B-field profile, and thus the pressure profile, is directly related to the system process parameters. A qualitative understanding of these relationships was developed, which may be used as a guideline to minimize the disruption of the B-field in the clamping device but cannot be used to accurately predict the actual deformation of the part to be consolidated. As previously mentioned, there are more factors contributing to this structural problem that must be fully understood before the part deformation can be accurately modeled. Structural modeling of the clamping device and of its interactions with a composite part is not within the scope of this thesis. However, this section provides a discussion of the important factors that must be considered in order to develop a structural model that may be used to completely simulate the deformation of the composite part and therefore the volume fraction of the final consolidated laminate part.

Forces caused by static magnetic fields are generally dealt with in electromagnetic texts using the formulation given in Equation 3.9, which relates the tractive stress in the direction of interest to the B-field component in that direction. Flux lines, as visualized with the FEA field model, may be thought of as tension lines, which generate force where they bend at the interface of a two materials of unlike permeability. This method is useful in systems with rigid steel armatures such as common electromagnetic devices like solenoids or holding devices. Equation 5.4 shows, however, that magnetic fields induced in a magnetically permeable medium create volumetric forces distributed throughout the medium. The standard Equation 3.9 formulation is basically a reduction of the volumetric forces into surface tractions. In the case of a highly elastic armature, knowledge of the

distributed volumetric force is much more critical. This is evident especially when considering the problem presented by the coil space of the electromagnet in the clamping device. Figure 5.39 shows that the axial B-field is always zero near the center of the coil space, which is equivalent to zero pressure via the surface traction equation. However, precise modeling of the distributed volumetric forces throughout the bulk of the armature coupled with the elastic model of the armature will show what degree of clamping pressure is lost in the coil location.

In addition to the distributed volumetric force, knowledge of the elastic model of the rubber armature is critical to proper structural modeling of the device. The modulus of the filled rubber is dependent upon the amount of filler. The samples fabricated with 30% iron particles by volume were substantially stiffer than the two with 15%. Silicone oil was also added to the rubber when it was mixed in order to reduce the viscosity and aid mixing of the filler. Greater amounts of silicone oil caused the rubber to become softer. Structural modeling could be used to determine the optimum stiffness of the armature for an even clamping pressure profile and silicone oil could be added to the degree necessary to reach this optimum level. Furthermore, the iron-filled rubber is a magnetorheological material and, as such, its elastic modulus is a function of the magnetic field that exists within it. A magnetic field applied to a magnetorheological material causes attractive forces between the individual magnetic particles, which translate into increases stiffness in the direction of the magnetic field. This field-stiffening effect also needs to be characterized in order for precise structural modeling to be performed.

An appropriate structural model for the composite part must also be used in order to completely model the performance of the device. The magnetic forces applied to the armature coupled with its elastic characteristics can be used to determine the compressive stress applied to the part, but the actual deformation of the part determines the volume fraction of the finished composite part. A fiber bed compaction model of the cloth and resin system to be consolidated should be included in the complete structural model to solve for the final deformation. Finally, it is desirable that the magnetic and structural effects be directly coupled in a complete model of the system. Magneto-structural coupling is ideal because deformation of the part changes the flux paths through the system and therefore the magnetic forces. Additional coupling of the magnetic field with the field-stiffening effect should also be included for completeness.

5.9 Design Example of Clamping Device

The purpose of this section is to provide an example of the design process for the magnetic clamping device. A device utilizing rectangular electromagnets is designed based upon the necessary part thickness and is shown to be scalable depending on the square area of the part. Power consumption and input voltage and current also is considered.

In this example, a 10mm thick part of approximately a square meter area is chosen for consolidation. The desired clamping pressure is 100 kPa. For the sake of discussion, it is also assumed that the rubber armature is of 30% loading and may be as thick as necessary. Rectangular electromagnets with an aspect ratio of 2 are chosen for the device. Figure 5.41 displays the geometric features of such an electromagnet.

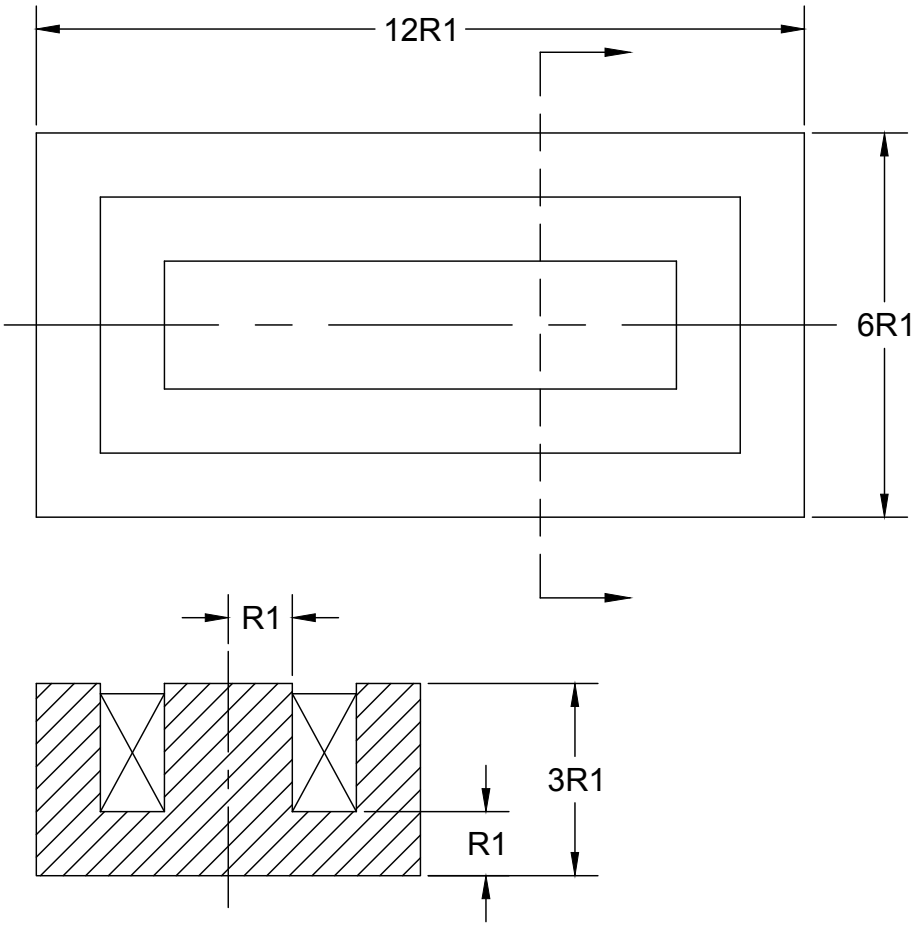

Figure 5.41 Rectangular electromagnet dimensions

The cross section of the rectangular electromagnet is very similar to that of a round electromagnet. Note, however, that the pole, yoke, and half-length of the core are all the same dimension. This relationship is necessary to keep the reluctance of the flux path elements of the back-iron equal. It is also assumed that the dimensions of the coil space are equal to R_1 by $2R_1$, which is typical for rectangular electromagnets. Next, the value k is chosen to be 0.075 to provide a good balance between input power and electromagnet size. The choice of k requires that $R_1 = 133$mm. The ideal armature thickness, maintaining $z = 1$, is also 133mm. Because z = 1 and $\phi = 30\%$, no pressure reduction factors need to be determined. A pressure of 100 kPa is chosen on the $k = 0.075$ performance curve,

requiring a current intensity of 375 A-turns/mm. The necessary electromagnet dimensions can be found using Figure 5.41. The overall length of the electromagnet is 0.8m and its width is 1.6m. Two electromagnets will therefore be used side-by-side in order to consolidate a part that is at least 1m by 1m.

The next design step is to choose the coil arrangement of the electromagnet and determine the necessary electrical power requirements. The current intensity and core radius are multiplied to give the necessary magnetomotive force of the electromagnet, NI = 50000 A-turns. Applied currents of I = 10A and I = 100A are used as the upper and lower currents that may be reasonably used with the system. Table 5.9 shows the details of the electromagnet coil and power requirements for a system driving currents of 10, 50, and 100A.

Table 5.9 Electromagnet power requirements

I [A]=	10	50	100
N =	5000	1000	500
wire d [mm]	2.67	5.96	8.43
wire length [m]	16000	3200	1600
wire C/S [mm^2]	5.59	27.93	55.85
Resistance [Ohm]	48.87	1.95	0.49
Voltage [VDC]	489	98	49
Power each [kW]	4.89		
Power [kW/m^2]	**3.82**		

Electromagnets driven with lower current require more coil turns to preserve NI. The cross sectional area of the coil is used to determine the required wire diameter to pack in N coils, assuming a square packing arrangement. The mean perimeter of the coil is 3.2m, which is used to calculate the total wire length. The wire length and cross sectional area is used to determine the total resistance of the coil, which determines the necessary driving DC voltage. The I = 10A case requires about 500 VDC, which may be

impractical and pose safety concerns. The I = 100A case requires 49 VDC. These requirements may be met with a device such as an industrial welder power supply. It is seen also that, regardless of the size of the coil wire, 5 kW are required to drive each electromagnet. Given that the total square area is 2.56 m^2, the system is able to apply a 100 kPa consolidation force with a power requirement of approximately 4 kW/m^2. If the device was employed, for instance, to consolidate a part the size of a commercial aircraft wing (approximately 150 m^2) at an energy cost of $0.005 per kWh, the device would cost $3 per hour of operation.

5.10 Device Performance with Alternative Materials

The purpose of this thesis is to study the feasibility of an electromagnet and armature clamping system for consolidating large-scale composite parts. The investigations focused primarily on the iron-filled rubber that was developed for use as an armature material. Iron was chosen as the filler based on the results of initial experiments and on the high saturation B-field of iron, which is 2.15T. Modeling and experiments demonstrated that iron-filled rubber may be used to achieve 100 kPa clamping pressures with reasonable power requirements, provided the device is designed with suitable characteristic ratios, z and k. In-depth study of different armature materials is outside the scope of this thesis. However, approximate knowledge of the performance of the device with alternative armature materials is helpful for the sake of future studies. As such, the purpose of this section is to predict the device performance with armatures of alternative materials. First, solid low-carbon 1018 steel is considered. Secondly, an idealized magnetic composite of permalloy and rubber material also is considered. Iron has low initial relative permeability, approximately 8000, and high saturation flux density.

Permalloy, however, has very high initial permeability, about 300,000, and a lower saturation of about 1.33T. Because the system air gaps and flux leakage are unaffected by the choice of armature material, performance curves are calculated at air gap ratios of k = 0.075. In addition, z = 1 is still assumed to be the ideal armature ratio with higher-permeability materials.

The BH curve of the ideal magnetic composite material with high initial permeability was developed based upon the BH curve of 65 permalloy (65% nickel, 45% iron). The permeability of a composite material is dependent upon the intrinsic nature of the filler and the filler fraction. As previously shown in Figure 4.8, the initial relative permeability of ϕ = 30% iron-filled rubber is limited to about 3. The permeability decreases with increasing applied field up to the saturation limit. Because permalloy has much higher initial permeability than iron, the idealized magnetic composite is assumed, for simplicity, to have an initial relative permeability of 100. In addition, the ideal composite is assumed to be loaded with 30% permalloy and therefore has a B-field saturation of 0.4T, based upon Equation 3.16. The material is further idealized by assuming that it acts as a linearly permeable material up to saturation. High initial and low-field permeability such as this may be possible with advanced filler materials or specialized filler particle shapes and alignment. Figure 5.42 displays the BH curves of 1018 steel, the ideal permalloy composite, and 65 permalloy for comparison.

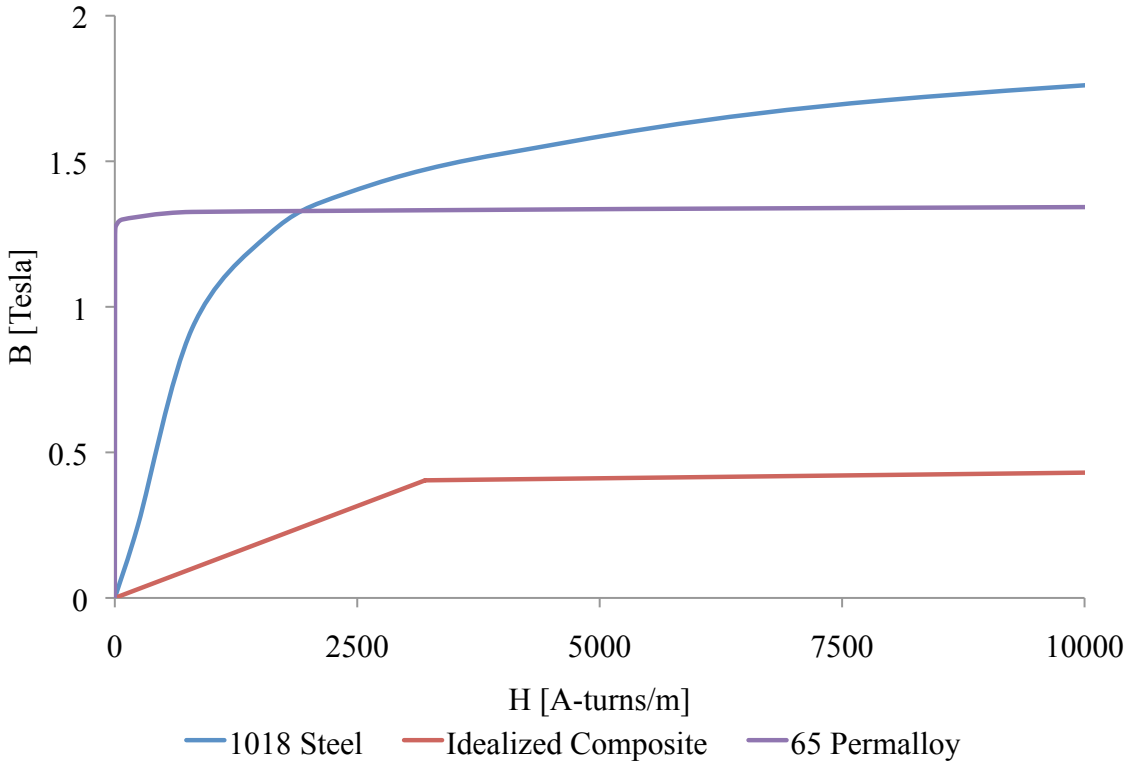

Figure 5.42 BH curves of 1018 steel, idealized composite, and 65 permalloy

The difference in initial permeability and saturation levels of 1018 steel and 65 permalloy are evident in the figure. The BH curve of the idealized composite of high-permeability filler is shown to be linear up to $H = 3200$ A-turns/m where it fully saturates. After this point the material has the same response as vacuum.

The BH curves of 1018 steel and the idealized composite material in Figure 5.42 were used in the model to generate performance curves relating clamping pressure to applied current intensity. An air gap ratio of $k = 0.075$ was used for all cases. The model with the idealized composite material was solved for $z = 1$. The model with the steel material was solved for $z = 1$ and $z = 0.25$ to demonstrate the possibility of using a thinner piece of solid steel as the armature. Figure 5.43 shows the results of these calculations along with the $\phi = 30\%$ iron-filled rubber curve for reference.

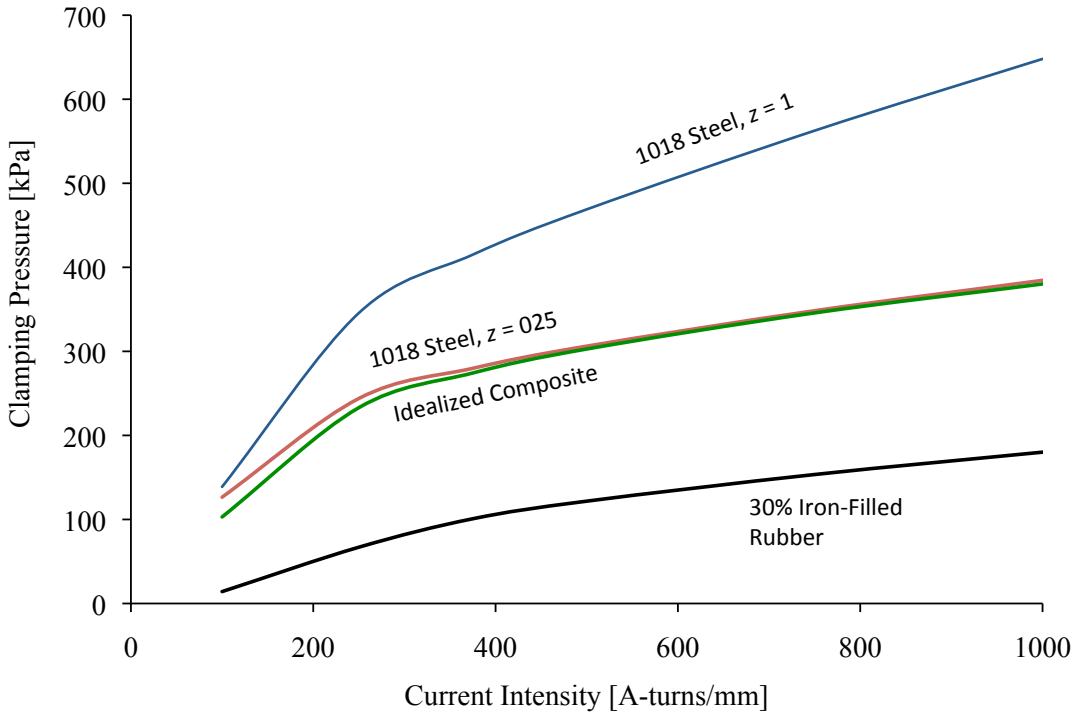

Figure 5.43 Performance curves with 1018 steel, idealized composite, and 30% rubber

Figure 5.43 shows that the two alternative materials are expected to significantly outperform the iron-filled rubber. Using a current intensity of 375 A-turns/mm as a reference, the iron-filled rubber achieves 100 kPa while solid steel at $z = 1$ reaches 415 kPa. The thinner $z = 0.25$ steel and the idealized composite both yield approximately 275 kPa. Note that the idealized composite and iron-filled rubber are both solved with $z = 1$. These results indicate that clamping pressures 3 to 4 times greater than those realized with the iron-filled rubber may be achievable with alternative armature materials. The curves also show that both alternative materials are able to reach the 100 kPa goal at much lower current intensities, which may not require forced cooling of the electromagnets.

The result of the modeling shown in Figure 5.43 show that a magnetic composite rubber material with high permeability but relatively low saturation flux density outperforms the iron-filled rubber material. If a material can be fabricated with a BH curve similar to that in Figure 5.42, it may provide approximately 3 times the clamping force of the iron-filled rubber. However, it is interesting to note that the low-carbon steel armature of $z = 0.25$ has a performance curve almost identical to that of the idealized composite material at $z = 1$. For the previously discussed example device designed to consolidate a 10mm thick part, an armature ratio of $z = 0.25$ refers to a thickness of about 33mm. As such, the clamping pressure achievable with an armature of advanced magnetic material is equivalent to that of a steel plate that is a quarter of the thickness.

The attractive features of a rubber armature are that it is flexible and able to be cast in place. The downsides are that the clamping pressure is limited in magnitude and unevenly distributed throughout the material. A solid steel armature offers a potential solution to these problems through increased clamping force and high mechanical stiffness. A steel armature would provide even clamping pressure over a broad part by virtue of its rigidity. However, forming or casting such an armature would be difficult and disadvantageous. One possibility is to employ smaller, discrete plates of steel in place of a continuous armature. A thin sheet of rubber may be placed between the steel and the workpiece in order to better distribute the pressure, especially over the discontinuities in the steel.

Modeling of two alternative armature materials, 1018 steel and an idealized high-permeability magnetic composite, suggest that advanced magnetic composite materials can outperform the iron-filled rubber, which is the focus of this thesis. If optimal device

proportions are preserved, the clamping pressure may be increased from 100 kPa to 275 kPa and 415 kPa for the idealized composite and steel, respectively. However, solid steel has the same performance as the advanced magnetic composite at a quarter of the thickness. This indicates that a simple low-carbon steel armature may be preferable to advanced magnetic materials. In addition, the original 100 kPa goal may be reached at current intensities below 100 A-turns/mm. As such, power requirements would be decreased by approximately 10 times and cooling may not be necessary for continuous operation. Further research is necessary to validate these model predictions and to determine if magnetic composites of advanced filler materials or fabrication techniques are able to reach higher clamping pressures.

5.11 Chapter Summary

The results of the force experiments with the high-purity iron filled rubber samples were presented in this section. The agreement of the FEA model calculations to the experimental results was analyzed and it was found that the model force predictions have approximately 10% error when air gaps are proportionally small and applied currents are large. The axial B-field simulated by the model was also compared with the experimental values obtained with a Gaussmeter. The simulation displayed good fitment with the experimental values and predicted B-field magnitudes with less than 15% error. It was concluded that the model is accurate enough to provide useful predictions of the performance of the magnetic clamping device.

The clamping device was analyzed from a flux-level magnetic circuit perspective in order to determine the characteristic ratios critical to system performance. The gap ratio k, the ratio of the air gap to the electromagnet core radius, was identified from flux

leakage considerations as an important system ratio. It was determined through simulation that k values above 0.1 are unacceptable for the clamping system and that k = 0.075 is the optimum gap ratio. Lower ratios are acceptable in terms of clamping pressure but necessitate the use of very large electromagnets. The optimum thickness of the armature was also shown to be equal to the electromagnet core radius. As such, the armature ratio z was defined as the ratio of the armature thickness to the core radius, with unity being the optimum value. The model was used to show that the system pressure decreases with decreasing z in a manner that is independent of k or and applied current. It was also shown that the clamping pressure of the system scales linearly with the volumetric magnetic filler loading of the armature.

The clamping pressure exerted by the electromagnet and armature system was shown from a theoretical approach to scale directly with the current intensity, defined here as the magnetomotive force of the electromagnet (NI) divided by the electromagnet core radius. It was therefore concluded that the clamping pressure of a device may be approximated by the two characteristic ratios, k and z, the armature loading fraction, and the current intensity without dependence upon the actual geometric scale of the system, assuming the electromagnets used in the system are well-designed. As such, the same design procedure may be followed whether the part to be consolidated is 3mm or 25mm thick. Additionally, it was shown that clamping pressures of 100 kPa are achievable with current intensity around 400 A-turns/mm, provided the device is thermally regulated. Higher pressures are possible but the system performance curves demonstrate lower marginal increases in pressure as the current intensity is increased beyond 500 A-turns/mm.

The design procedure for the magnetic clamping device was presented in a flowchart configuration. The procedure uses the part thickness as a starting point and provides an iterative method for choosing the proper electromagnet and armature configurations to achieve a required clamping pressure. In addition, an example system was designed using two rectangular electromagnets to consolidate a 10mm thick part of approximately a square meter area. The example design of the electromagnet coil was discussed as well as the necessary power supply requirements. The example was designed with characteristic ratios that are less than optimal in order to provide an upper bound on the power requirements. The system was shown to require approximately 4 kW of electrical power per square meter of part. Also, the coil was shown to require 100A and 50 VDC power input, which are reasonable values for an industrial power supply. As such, it is concluded that the clamping system may be expected to produce 100 kPa of clamping pressure at less than 4 kW per square meter, provided the system is designed correctly.

Experiments were also performed to observe the effect of an electromagnet array configuration on the performance of the device. Proportionally large air gaps caused reductions in the system pressure by up to 40% due to interference of the neighboring electromagnets. However, this interference is not expected to be a significant issue in systems with small air gaps. In addition, force experiments were performed with a set of low-carbon steel samples in place of the rubber armature. It was determined that the performance of a rubber armature compared with that of a steel armature does not scale with the total mass of iron. At some armature thickness, however, steel does outperform

the rubber. The possibility of utilizing layered steel shim stock may be considered as an alternative method to achieve conformable clamping on a composite part.

Simulations were performed to characterize the effect of the critical system ratios and parameters on the axial B-field profile present on the bottom face of the armature. It was shown that higher values of k, z, and ϕ yield flatter axial B-field profiles, which translates to more even pressure profiles. The need for magneto-structural coupled modeling was discussed in terms of its ability to predict the actual consolidation of a composite part.

Finally, device performance was predicted for two armature materials as alternatives to the iron-filled rubber. First, low-carbon steel was used and shown to create clamping pressures of over 400 kPa for $k = 0.075$ and $z = 1$. Second, an idealized magnetic composite material, meant to be an upper limit on the magnetization response of a rubber filled with advanced magnetic materials, was used in the model and shown to create up to 275 kPa at realistic power inputs. However, solid steel was also shown to match the performance of the idealized material at a quarter of the armature thickness, indicating that the advantages of steel are likely to outweigh those of an advanced magnetic material. Further investigations are necessary to determine if these higher clamping pressures are possible and to determine practical ways to utilize a solid steel armature in the clamping device.

CHAPTER 6

CONCLUSION

The consolidation pressure developed by the magnetic clamping device was characterized through experimentation and FEA modeling. Theoretical consideration of magnetic flux demonstrated that two geometric system ratios, k and z, the air gap and armature ratio, respectively, are critical to the performance of the device. The FEA model was used to optimize these ratios at values of $k = 0.075$ and $z = 1$. These ratios may be used with a design process developed in this thesis to yield consolidation pressures of approximately 100 kPa with realistic electrical power requirements. The device was shown to generate these pressures with less than 4 kW of input power per square meter of part area. However, there are some practical limitations to the device that must be considered. First, optimal design of the device required electromagnets with widths of over 50 times the thickness of the part. Parts over 10mm thick require electromagnets on the order of one meter wide. Second, the applied currents recommended for use are higher than those generally used in commercial electromagnets, therefore the electromagnets must be cooled. For large electromagnets especially, this may entail designing internal coolant channels, which adds to the complexity and expense of the system. Third, the thickness of the magnetic rubber sheet is required to be, at minimum, approximately a tenth of the width of the individual electromagnets used in the device. Again, for large electromagnets this requirement may prove to be cumbersome and expensive.

Discussion of the controlled atmospheric pressure resin infusion (CAPRI) process, developed by Boeing as an enhancement to traditional vacuum infusion

processes for composite laminates, shows that clamping pressure of 100 kPa is sufficient for the device to be of practical utility in the manufacturing process. Gains are expected in the fiber volume fraction, and therefore mechanical properties, of parts consolidated by vacuum infusion aided by the magnetic clamping device. However, typical autoclave manufacturing processes involving thermoset prepreg require consolidation pressures of about 600 kPa. The magnetic clamping device is unable to develop such pressures reasonably. Furthermore, thermoplastic prepreg requires even higher compaction pressures, often greater than 1 MPa, and processing temperatures as high as 400°C. Given the limitations of the device and the fact that silicone rubber degrades at temperatures over 300°C, the device is not recommended for use with thermoplastic prepreg materials.

Further research is required to accurately predict the pressure profiles produced by the device on the face of a composite part. The modeling performed in this thesis is limited to magnetic field simulation and effective surface tractions at the bottom of the rubber sheet. However, the actual magnetic forces are volumetric and exist throughout the rubber and must be modeled as such. A complete structural analysis should also include an elastic model of the rubber, the magnetorheological effects, and a fiber compression model of the part. This analysis will also determine how the pressure profile acts over the coil space of the electromagnets. Furthermore, an accurate model should include direct magneto-structural coupling of the magnetic field and elastic effects. In addition, further research may consider the use of magnetic rubbers with advanced magnetic materials or solid steel armatures, as initial modeling indicates that clamping pressures of approximately 300-400 kPa are possible.

REFERENCES

Abraham, D., 1998, "A comparison of physical properties of glass fibre epoxy composites produced by wet lay-up with autoclave consolidation and resin transfer moulding," *Composites Part A*, Vol. 29A, pp. 795-801.

Acheson, J., Simacek, P., Advani, S., 2004, "The implications of fiber compaction and saturation on fully coupled VARTM simulation," *Composites Part A*, Vol. 35, pp. 159-169.

American Society for Metals, *Metals Handbook, vol.1, Properties and Selection: Irons and Steels*, 9th ed., 1978.

Anhalt, M., 2008, "Systematic investigation of particle size dependence of magnetic properties in soft magnetic composites," *Journal of Magnetism and Magnetic Materials*, Vol. 320, pp. 366-369.

Anhalt, M., Weidenfeller, B., 2007, "Magnetic properties of polymer bonded soft magnetic particles for various filler fractions," *Journal of Applied Physics*, Vol. 101, No. 2.

ANSI/NEMA MW 1000-2008, *Magnet Wire*, National Electrical Manufacturers Association, Virginia, 2008, Table 1-1.

Åström, Thomas, *Manufacturing of Polymer Composites*, CRC Press, 1st edition, 1997.

Bansal, Rajeev, *Handbook of Engineering Electromagnetics*, Marcel Dekker, New York, 2004.

Davies, L.W., et al., 2007, "Effect of cure cycle heat transfer rates on the physical and mechanical properties of an epoxy matrix composite," *Composites Science and Technology*, Vol. 67, pp. 1892-1899.

Davis, L.C., 1999, "Model of magnetorheological elastomers," *Journal of Applied Physics*, Vol. 85, No. 6.

Gutowski, T.G., Cai Z., Kingery J., Wineman S.J., 1986, "Resin flow/fiber deformation experiments," *SAMPE Quarterly*, Vol. 17, No. 4, pp. 54-58.

Gutowski, T.G., *Advanced Composites Manufacturing*, John Wiley and Sons, New York, 1997.

Hou, T. H. and Jensen, B. J., 2008, "Double-vacuum-bag technology for volatile management in composite fabrication," *Polymer Composites*, Vol. 29, No. 8, pp. 906-914.

Jolly, M.R., et al., 1996, "A model of the behavior of magnetorheological materials," *Smart Material Structures*, Vol. 5, pp. 607-614.

Long, A.C., 2001, "Experimental characterisation of the consolidation of a commingled glass/polypropylene composite," *Composites Science and Technology*, Vol. 61, pp. 1591-1603.

Moon, F.C., *Magneto-solid Mechanics*, John Wiley and Sons, New York, 1984.

Niggeman, et al., 2008, "(CAPRI) Process Experimental Investigation of the Controlled Atmospheric Pressure Resin Infusion," *Journal of Composite Materials*, Vol. 42, No. 11, pp. 1049-1061.

Potter, K., *Resin Transfer Moulding*, Chapman and Hall, London, 1997.

Ramasamy, A., Wang, Y., Muzzy, J., 1996, "Braided Thermoplastic Composites From Powder-Coated Towpregs. Part III: Consolidation and Mechanical Properties," *Polymer Composites*, Vol. 17, No. 3, pp. 515-522.

Roters, Herbert C., *Electromagnetic Devices*, John Wiley and Sons, New York, 1941.

Vicente, J., et al., 2002, "Permeability measurements in cobalt ferrite and carbonyl iron powders and suspensions," *Journal of Magnetism and Magnetic Materials*, Vol. 251, pp. 100-108.

Young, Wen-Bin, 1995, "Compacting pressure and cure cycle for processing of thick composite laminates," *Composites Science and Technology*, Vol. 54, pp. 299-306.